*Università degli Studi di Salerno*

Dipartimento di Ingegneria dell'Informazione, Ingegneria Elettrica e Matematica Applicata


Dottorato di Ricerca in Ingegneria dell'Informazione
XII Ciclo – Nuova Serie

TESI DI DOTTORATO

# A Study on Defects in Organic Semiconductors for Field Effect Transistors


CANDIDATO: **ROSALBA LIGUORI**

TUTOR: **PROF. ALFREDO RUBINO**

COORDINATORE: **PROF. ANGELO MARCELLI**


Anno Accademico 2012 – 2013

*To my family*

*Those who have reached a stage where they are unable of wonder for anything, simply demonstrate that they have lost the art of thought and reflection.*

**Max Planck**

## Acknowledgements

I owe my sincere gratitude to my supervisor, Prof. Alfredo Rubino, for his teaching and his special help in making this thesis possible.

I would like to thank Prof. Angelo Marcelli, for his guidance for Doctoral School in Information Engineering and his support throughout these years.

I remain grateful to Prof. Antonio Facchetti, who accommodated me at Northwestern University in Chicago, allowing me the use of their equipment, and all the people at Polyera Corporation who offered their time, assisting me and sharing useful information.

Special thanks to my family, my friends, all colleagues and students met during my experience.

My immensurable gratitude goes to people who are always there for me.

*Rosalba*

# Contents

**Introduction ........................................................................... 1**

**Chapter 1**
**Organic thin film transistors ............................................................ 5**
1.1 Organic semiconductors ........................................................... 6
1.2 OTFT operating principles ........................................................ 8
1.3 Electrical characteristics and non-idealities ........................... 12
1.4 Fabrication................................................................................ 16
1.5 Materials.................................................................................... 17
1.5.1 Gate dielectrics ............................................................17
1.5.2 Pentacene ......................................................................19
References .........................................................................................21

**Chapter 2**
**Defects in organic semiconductors.................................................. 23**
2.1 Basic mechanisms in organic semiconductors ....................... 24
2.1.1 Optical properties.........................................................25
2.1.2 Charge carrier transport ...............................................26
2.1.3 Charge carrier injection ...............................................29
2.2 Bias stress.................................................................................. 31
2.3 Origin of defects....................................................................... 33
2.4 Effects of defects on OTFT electrical properties ................... 37
2.4.1 Effects on threshold voltage ........................................37
2.4.2 Effects on mobility.......................................................38
2.4.3 Type of conduction ......................................................39
References .........................................................................................41

**Chapter 3**
**Metastable light induced effects in pentacene................................ 43**
3.1 Photocurrent in a pentacene thin film.................................... 44
3.2 Light effects from infrared to near-ultraviolet........................ 51
3.3 Deep UV light induced metastable defects ............................ 57
3.4 Conclusion............................................................................ 63
References..................................................................................... 65

**Chapter 4**
**Interface trap states in organic thin film transistors .................... 67**
4.1 Photocurrent in organic field effect transistors ...................... 68
4.1.1 Pentacene based thin film transistors with ActivInk D0150 dielectric........................................... 68
4.1.2 Light induced effects in pentacene thin film transistors ................................................................... 72
4.1.3 Photovoltaic and photoconductive effects ................... 76
4.2 Defect evaluation through photocapacitance studies ............. 83
4.2.1 Pentacene based thin film transistors with PVP-co-PMMA dielectric................................... 84
4.2.2 Capacitance measurements in dark ............................. 86
4.2.3 Photo-capacitance measurements................................ 88
4.2.4 Interface trapping ....................................................... 94
4.2.5 Light-induced hysteresis ............................................. 99
4.2.6 Admittance spectroscopy .......................................... 102
4.3 Conclusion.......................................................................... 104
References................................................................................... 105

**Chapter 5**
**Admittance spectroscopy in an organic based MIS capacitor ... 107**
5.1 Admittance measurements in pentacene–based MIS capacitors......................................................................... 108
5.2 Equivalent electrical model ................................................ 113
5.2.1 Insulator layer .......................................................... 114
5.2.2 Depletion layer and interface states .......................... 115
5.2.3 Organic semiconductor bulk ..................................... 117

5.2.4 Contact resistance ....................................................121
5.3 Model simulations ............................................................ 122
5.4 Experimental data fitting and model parameters.................. 125
5.5 Temperature dependence of capacitance measurements...... 132
5.6 Validation of the electrical model ....................................... 136
5.7 Conclusion.......................................................................... 138
References ..................................................................................139

**Conclusions ...................................................................... 141**

# Introduction

As technological research is progressively evolving, product costs in competitive markets dictate even more pressing specifications. At the same time, more relevance should be given to the energy waste and environmental impact of the modern society consumerism, increasing the effort in researching novel approaches and unconventional materials that could help to overcome these challenges. In this scenario, the development of organic electronics has been encouraged, thanks to new attractive properties and promising applications.

For these materials, the chief technology is that of thin films. It perfectly befits the issue of preservation of manufacturing energy usage and provides a valid solution to toxic element minimizing. It also enables the spread of light-weight, unbreakable, transparent and flexible devices.

Many advances have been made in the electronic applications of organic materials. However, important drawbacks remain, such as low charge carrier mobilities and extreme sensitivities to ambient conditions, temperature, light, oxygen and moisture, which could degrade their pristine features. Moreover, the theoretical interpretation of their electronic and optical properties is still incomplete.

The aim of the present research is the understanding and the modeling of mechanisms involved in these unconventional materials, along with a study of their electrical stability, essential to allow the adoption of organic devices in practical applications. For this purpose, besides being a key device of technological interest, thin film transistor can be exploited as a tool for studying the charge transport in organic solids.

The present work has been developed in this context, focusing the attention on the role played by organic semiconductor defects on the electrical performance of organic transistors. Critical issues are indeed the localized states related to the presence of structural defects and chemical impurities. They dominate the charge carrier transport in organic semiconductors and define the quality of interfaces occurring in the transistors. The study has been initially centered on the characterization of a small conjugated organic molecule, the pentacene.

It has been investigated both in the form of a polycrystalline thin film and in combination of various gate insulators for the realization of the active layer in p-type transistors.

In both cases, the characterization methods have been employed in a more effective way, that is, by the use of photo-irradiation to generate a high concentration of both charge carriers. The motivation was that in a p-type semiconductor the presence of a large enough density of electrons could introduce electronic behaviors which otherwise would not be visible. This method has been revealed a useful means to identify trap states affecting charge transport and, simultaneously, to evaluate the stability of the electrical performances of the organic transistors under persistent bias and illumination.

Afterwards, the investigations have been focused on the properties of the interface between the gate insulator and the organic semiconductor, where the conduction in the organic transistor occurs. For this purpose, organic based metal-insulator-semiconductor capacitors have been studied by the use of admittance techniques.

In the organization of the thesis work, after a brief illustration of the working principles of organic thin film transistors in Chapter 1, an overview of the main features of organic semiconductors is presented in Chapter 2. In particular, specific attention has been paid on the most relevant models which describe the charge transport mechanism in disorder solids, showing how it is affected by localized states. Thus, a list of the possible origins of traps and their most significant effects on electrical characteristics has been proposed.

Organic devices have been fabricated and a series of experiments have been carried out to investigate their performance. All devices have been fully processed in the cleanroom (class 100) located in the Microelectronics Laboratory of the University of Salerno. Moreover, some of the organic materials used in the device fabrication have been specifically synthetized at the Department of Chemistry and the Materials Research Center of the Northwestern University in Chicago. The electrical characteristics of the organic transistors have been analyzed with respect to fabrication process parameters, film morphology and used geometries, focusing on the nonideal behaviors and with the aim of optimizing their characteristics.

Thus, a fundamental part of the thesis work has concerned the study of light effects on a pentacene thin film, from infrared to ultraviolet, and the development of a mathematical model describing the generation and annealing dynamics of photoinduced defects under deep ultraviolet

light, with particular attention on their metastable nature. The proposed model is described in Chapter 3.

As regards the performance stability of thin film transistors, they have been characterized through current and capacitance measurements, in dark and under light conditions, in ambient air or in vacuum. Light induced effects have been investigated and the equations modelling the photocurrent phenomena have been deduced. The proposed model, illustrated in Chapter 4, has been proved to be effective in evaluating the light effects on material structure and distinguishing the photovoltaic and photoconductive effects occurring in the organic device. In addition, instability phenomena of transistor threshold voltage have been estimated through photocapacitance studies and a characterization of interface electron traps has been addressed.

Finally, the potentialities of admittance spectroscopy in an organic base metal-insulator-semiconductor structure have been exploited, allowing a complete analysis of the most significant aspects of an organic field effect transistor. An electrical model useful for the description of the physical processes involved in organic devices has been developed during the research activities and is presented in Chapter 5. This model has succeeded in describing the experimental data and in justifying the differences observed among devices based on various materials and structures. It has been proved to be useful to characterize the dynamics of trapping mechanisms at the insulator-semiconductor interface and in the organic semiconductor bulk. Moreover, it can be employed in circuit simulations.

# Chapter 1

# Organic thin film transistors

Mechanical flexibility, transparency, synthesis versatility, innovative applications, combined with cost-effective, reduced power consumption and large area production processes, are just a few of the key features that encourage the development of organic electronics.

There are three broad classes of organic electronic devices, classified according to their functions. They include organic light-emitting diodes (OLEDs), organic solar cells (OPV) and organic thin-film transistors (OTFTs). Irrespective of the functions of these devices, they generally have a sandwich structure of anode-organic material-cathode, assuming the form of a thin film stack. The total thickness ranges from 50 to 200 nm.

In particular, the organic thin film transistor is now a mature device, which has made an impressive progress over the past three decades. The spectrum of its applications (Fig. 1.1) ranges from pixel driver transistors for flat panel display backplanes, which required very high uniformity of the various electrical performance characteristics and large drive currents, to transistors in integrated circuits for radio-frequency transponders with limited budget in supply voltage.

In this chapter, an introduction on organic semiconductors and a description of OTFT operating principles are addressed, along with an overview on the employed fabrication methods and materials.

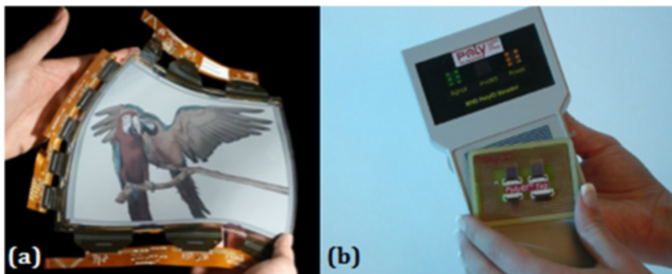


**Figure 1.1.** Applications of OTFTs in OLED displays (a), RFID systems (b).

## 1.1 Organic semiconductors

Organic materials are aggregates of carbon-based small molecules or polymers. Since their typical energy gap ranges between 1.5 and 3.5 eV, they have few carriers at room temperature and can be considered as insulators.

The electronic states of organic molecules are generated from the p-orbitals of carbon atoms through $sp^2$ hybridization. In a $sp^2$ hybridized orbital (Fig. 1.2), three planar σ-bonds are present with large binding energies and localized electrons. The remaining unhybridized p-orbitals form π-bonds with lower binding energies, giving rise to a double bond. In the latter case, the electrons are loosely bound and can be delocalized inside a molecule, becoming responsible for electrical conduction.

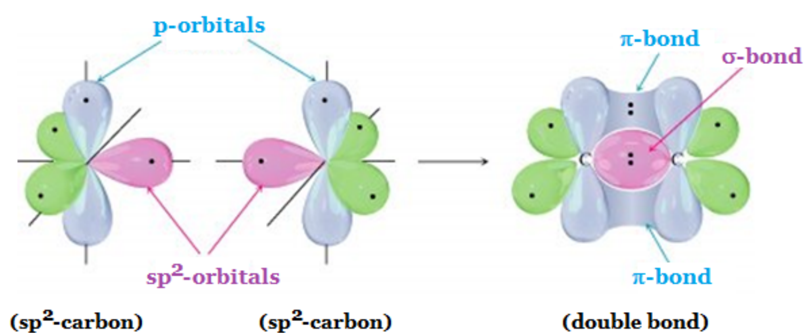


**Figure 1.2.** $Sp^2$-hybridization of carbon orbitals and formation of a double bound between two adjacent carbon atoms.

The π-orbitals define the analogous to the valence band and conduction band of an inorganic semiconductor. In detail, the highest π-bonding orbital that is occupied by electrons is called HOMO (highest occupied molecular orbital) and the lowest π-antibonding orbital that is unoccupied is called LUMO (lowest unoccupied molecular orbital). The σ- and π-bonds are the intramolecular bonds which bind atoms to form a single organic molecule. On the contrary, the intermolecular interactions, such as the van der Waals forces, are very weak and the overlap of wavefunctions centered on neighboring molecules is very small [1]. As a result, the solid has a disordered structure, with variable

local environments of molecules, and the electronic properties of the organic material retain much of the character of their molecular constituents. At the same time, these features confer unconventional and desirable mechanical properties on organic semiconductors, making them better suited for niche applications requiring large area coverage, structural flexibility, low temperature and low cost processing.

The charge states of the organic molecules are structurally relaxed charged states, defined as electron polaron and hole polaron, even if, for simplicity, they are referred to as electron and hole. The reason is that adding or removing an electron from a molecule leads to significant structural relaxations of the surrounding atomic and electronic environment. The fundamental mechanisms of electron and hole transport in disordered organic solids are not fully understood. From a microscopic point of view, the charge carriers move in an organic semiconductor through an intermolecular process, by hopping between adjacent molecules (Fig. 1.3). Moreover, they can be localized by defects, disorder or potential wells caused by the polarization. If the lattice is irregular or the carrier becomes localized on a defect site, the lattice vibrations are essential to let the carrier move from one site to another. This is an activated process and the mobility increases with increasing temperature.

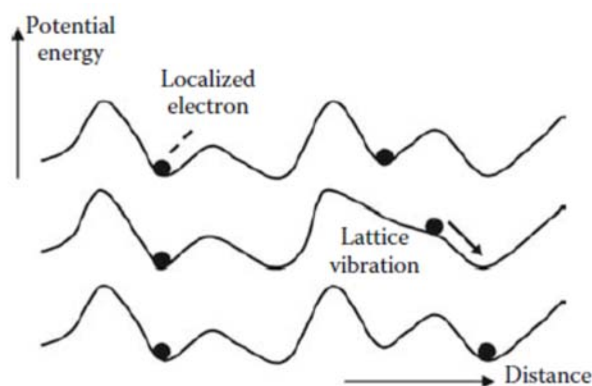


**Figure 1.3.** Hopping transport mechanism.

Materials used as semiconductors in electronic devices can be sorted in conjugated polymers and small conjugated molecules. Conjugation is fundamental for a good electrical conduction. It originates from an alternation of single and double bonds, which

confers rigidity to the molecules, so that in the solid state, as rigid rods, they tend to pack in a compact way with their long axis parallel to each other. The width of each single layer, arranged one over another, almost equals the length of the molecule, with typical values ranging between 1.5 and 3 nm. This structure in conjugated organic solid favors the charge transport in the direction parallel to the layers.

## 1.2 OTFT operating principle

Field-effect transistors (FET) fabricated with organic materials assume predominantly the geometry of a thin film transistor, since for this type of structure low requirements on purity are needed. The first TFTs were made of cadmium sulfite and cadmium selenide, but were rapidly substituted by amorphous silicon, first fabricated in 1979. TFTs have been often used as structures to study transport in solid materials with low mobilities and analyze interface quality. Moreover, in last decades the TFT technology has been revealed to have wide potentialities and it has been exploited mainly in the active matrix of liquid crystal displays (AM-LCD). Most of current TFTs, made of amorphous or polycrystalline silicon, find application in display control, X-ray digital sensors, such as those in medical area, and RFID (radio-frequency identification) tags. Research activities in TFT technology have been continuously encouraged by new needs and interesting applications, among which are OLED displays, flexible and lightweight electronics for mobile phones, palmtops and electronic players, low-cost and rapid fabrication processes, such as inkjet printing. Organic materials, studied since the late 1940s, were introduced in this context, thanks to their attractive features. A transistor based on a polymeric semiconductor was experimented in 1983 for the first time, with a device made on an electrochemically grown polythiophene film, while the possibility of fabricating organic TFT with small molecules was shown in 1989 with the use of sexithiophene [2].

The electrical behavior of TFTs is remarkably similar to that of the MOSFET (metal-oxide-semiconductor FET). A thin film transistor is a three terminal device: two of the electrodes, the source and the drain, are in contact with the semiconductor film at a short distance from one another; the third electrode, the gate, is separated from the semiconductor film by the insulating layer (Fig. 1.4).

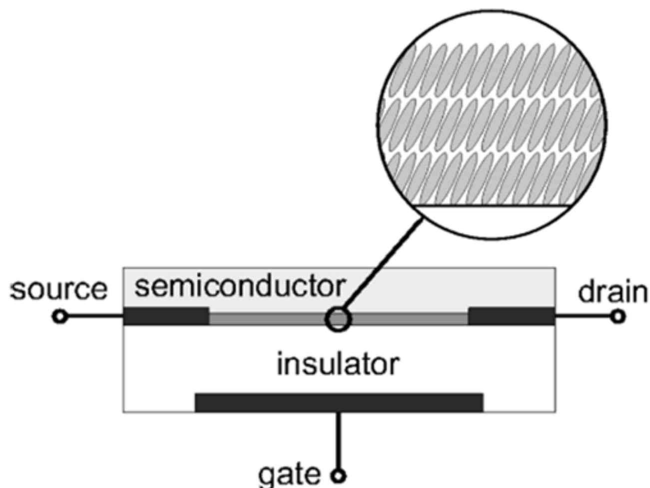


**Figure 1.4.** Schematic view of an organic thin-film transistor and illustration of the layer structure of the conducting channel.

A voltage gate, $V_G$, is applied on the substrate or gate electrode. Charges, which are injected from the source electrode into the active material, are accumulated at the layer adjacent to the gate dielectric under the influence of $V_G$ to form a conducting channel. Under this condition, another voltage is applied at the drain electrode, $V_D$, which carries the charges from source to drain through the channel.

Different configurations of OTFTs exist, depending on the sequence of film deposition (Fig. 1.5). As for the position of gate electrode, two architectures are distinguished: bottom gate and top gate configurations. For bottom gate configuration, a few hundred nanometers insulator (gate dielectric) is grown on a substrate with a conducting layer (gate electrode). A highly doped silicon substrate could serve directly as the gate electrode, otherwise, if the substrate is glass or plastic, a conducting electrode is deposited on it. The active material and the two electrodes of source and drain are deposited above. Conversely, in a top gate configuration, the active material and electrodes are deposited on the substrate, followed by the deposition of gate insulator and gate contact.

These two configurations, in turn, are separated in other two classes: bottom contact and top contact configurations, depending on the deposition sequence for electrodes and active layer. In the bottom contact configuration, the organic layer is incorporated into the device after the source and drain electrodes are deposited. For the top contact

devices, the organic layer is the first to be deposited, followed by the source and drain electrode deposition.

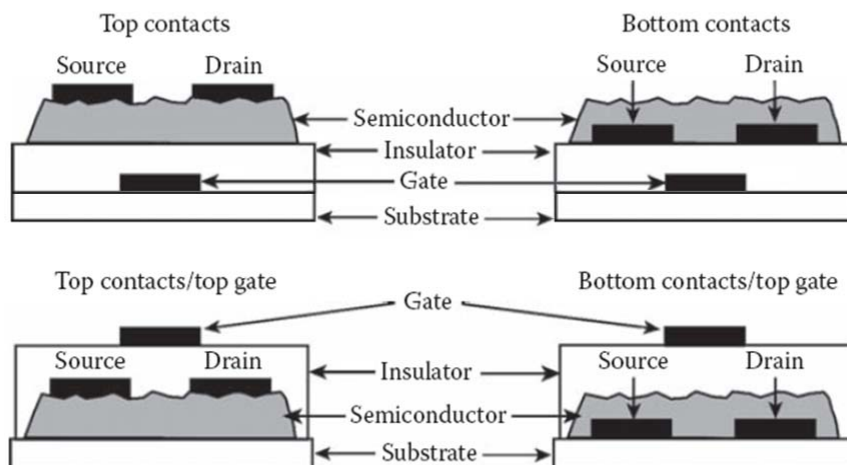


**Figure 1.5.** Four possible configurations for an OTFT.

As regards the charge transport, two types of OTFTs exist: p-type, where the majority charge carriers are holes, and n-type, where electrons are the majority charge carriers. However, this concept differs from that of doping in conventional semiconductors.

Let consider, as an example of p-type transistor, a device made of pentacene, that is, a small conjugated molecule, as semiconductor and gold as electrodes. The Fermi level of gold is close to the HOMO level of pentacene. When a positive voltage is applied to the gate, negative charges are induced at the source electrode. Since the Fermi level is far from the LUMO level, electron injection is very unlikely and no current should pass through the pentacene layer, except for the leakage through the insulating film. When the gate voltage is reversed, holes can be injected from the source to the semiconductor, thanks to the close alignment between gold Fermi level and pentacene HOMO. Consequently, charges accumulate at the insulator-semiconductor interface, forming a conducting channel, which allows the charges to be driven from source to drain by applying a bias to the drain. Because holes are more easily injected than electrons, pentacene is said to be p-type. Symmetrically, an organic semiconductor is said to be n-type, when the LUMO is closer to the Fermi level than the HOMO and thus electron injection is easier than hole injection.

In more detail, three states of the device are distinguished, depending on the value of the gate bias: depletion, intrinsic and accumulation mode (Fig. 1.6). In the depletion regime, the bias applied to the gate is positive and the semiconductor is depleted of majority charges. The current flowing through the device consists only of the semiconductor bulk current, which due to the low intrinsic charge carrier density is very small. When the gate bias reaches the so called switch-on voltage, the flat-band condition is fulfilled and the semiconductor is in the intrinsic state. The switch-on voltage is influenced by any fixed charges in the insulator layer and at the insulator-semiconductor interface. Above this voltage the current increases with the gate voltage and the device works in the accumulation regime.

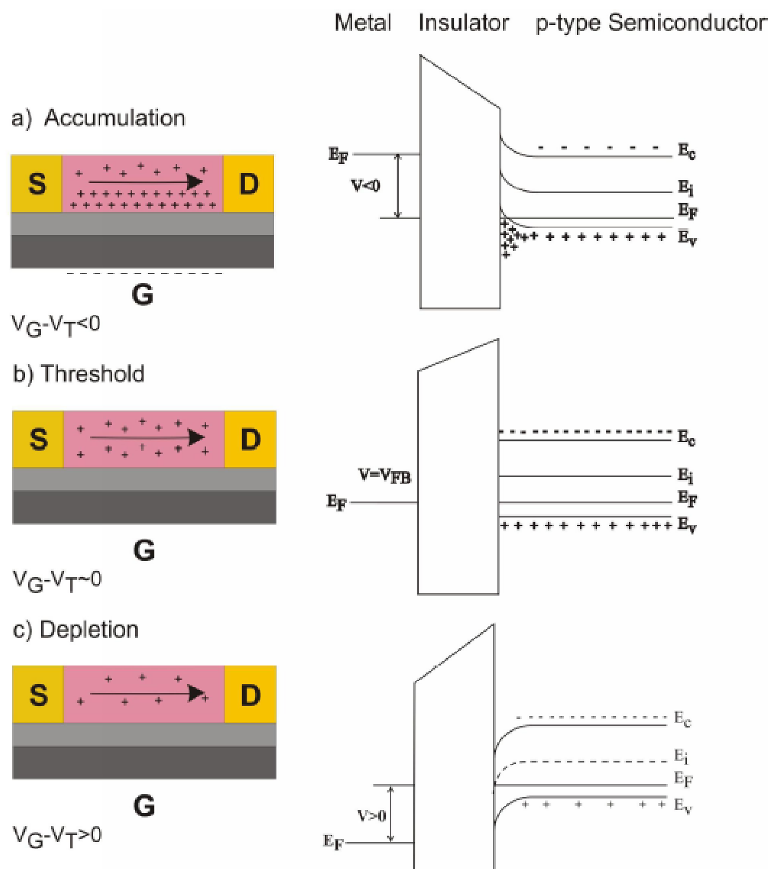


**Figure 1.6.** The three different regimes of operation of an OTFT: accumulation (a), threshold (b), depletion (c). $V_T$ and $V_{FB}$ are, respectively, the threshold and flatband voltages.

## 1.3 Electrical characteristics and non-idealities

Observing the typical output characteristics ($I_D$ vs $V_D$), shown in Figure 1.7a, two operating regions are distinguished: linear and saturation regions. The conductance of the channel formed in the semiconductor at the interface with the insulator is proportional to the gate voltage. At low drain biases, the current increases linearly with drain voltage (linear region), but when the drain bias is comparable to gate voltage, the potential drop at drain contact falls to zero, the conducting channel is pinched off and the current becomes independent from the drain voltage (saturation region).

The drain current $I_{DS}$ assumes the following expressions:

$$I_{DS}^{lin} = \frac{W}{L}\mu_{FE}^{lin}C_i\left[V_{DS}\left(V_{GS}-V_T\right)-\frac{V_{DS}^2}{2}\right] \quad \text{(linear region)}, \qquad (1.1a)$$

$$I_{DS}^{sat} = \frac{W}{2L}\mu_{FE}^{sat}C_i\left(V_{GS}-V_T\right)^2 \quad \text{(saturation region)}, \quad (1.1b)$$

where $W$ and $L$ are the channel width and length, respectively, $C_i$ is the capacitance of gate dielectric per unit area, $V_T$ is the threshold voltage, $V_{GS}$ and $V_{DS}$ are the voltages at gate and drain electrodes, respectively, related to the source potential, $\mu_{FE}$ is the field effect mobility, which is the carrier mobility obtained from TFTs and can assume different values depending on the operation in linear or saturation region.

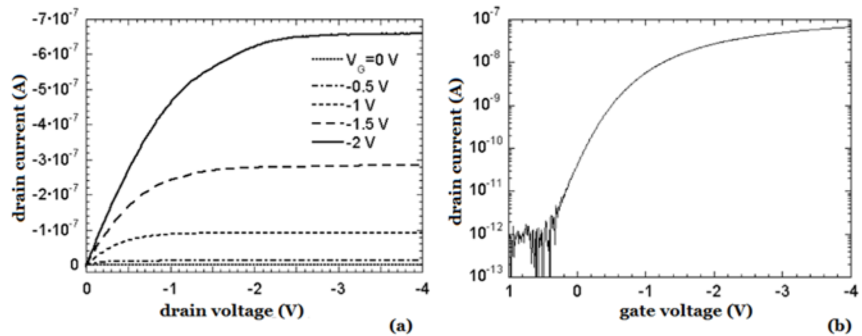


**Figure 1.7.** Typical output (a) and transfer (b) characteristics of OTFTs.

In the transfer characteristics ($I_D$ vs $V_G$), shown in Figure 1.7b, a threshold is evident: below this threshold, most of induced charge carriers are trapped in localized states and the current, due to diffusion process, increases exponentially; while, in the above threshold regime, the current becomes proportional to the gate bias, according to the operating modes described above.

The organic thin film transistor is considered a two-dimensional device, because nearly all the charge of the conducting channel resides in the first monolayer next to the insulator-semiconductor interface. It can be viewed by the estimation of the charge distribution *n(x)* across the semiconductor film:

$$n(x) = \frac{(C_i V_{GS})^2}{2k_B T \varepsilon_S} \left(1 + \frac{x}{\sqrt{2} L_D}\right)^{-2} , \tag{1.2}$$

where $x$ is the axis normal to the interface, $k_B$ the Boltzmann constant, $T$ the absolute temperature, $\varepsilon_S$ the permittivity of the semiconductor and $L_D$ is the Debye length:

$$L_D = \frac{\sqrt{2} k_B T \varepsilon_S}{q C_i V_{GS}} . \tag{1.3}$$

By defining the channel as the layer of uniform charge density that would contain the same amount of charge than that obtained by integrating the charge distribution, its thickness results equal to $\sqrt{2} L_D$. Typical values for the Debye length range between 0.1 and 1 nm, which are noticeably lower than the thickness of a monolayer.

The field effect mobility can be obtained in linear region from the slope of the plot of $I_D$ vs $V_G$, and in saturation region from the slope of the plot $\sqrt{I_D}$ vs $V_G$, according to the following equations:

$$\mu_{FE}^{lin} \equiv \frac{L}{W C_i V_D} \frac{\partial I_D}{\partial V_G} , \tag{1.4a}$$

$$\mu_{FE}^{sat} \equiv \frac{2L}{W C_i} \left(\frac{\partial \sqrt{I_D}}{\partial V_G}\right)^2 . \tag{1.4b}$$

However, in organic transistors the actual curves often deviate from pure straight lines and an increase of the mobility with the gate bias, due to charge trapping, is often revealed [3]. This dependence could be expressed by the formula:

$$\mu = \mu_0 \left(V_{GS} - V_T\right)^{\gamma} \ , \tag{1.5}$$

where $\mu_0$ and $\gamma$ are semi-empirical parameters.

Besides non-homogeneities and low purity in organic semiconductors, other non-linearities should be encountered in the electrical characteristics of an OTFT. They include contact resistance, parallel conductance and leakage currents.

The presence of a significant contact resistance is known to induce a superlinear growth of the current with the bias in linear region. Its entity can be evaluated by the use of the transfer length method (TLM), where the channel resistance of a set of transistors with different channel lengths is measured and the contact resistance is taken from the value corresponding to a channel with zero length (Fig. 1.8).

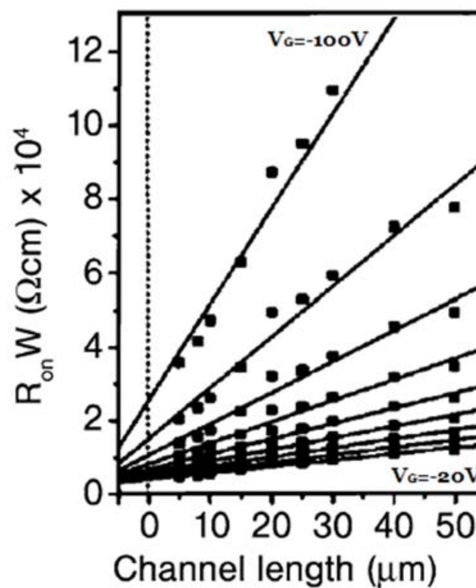


**Figure 1.8.** Width-normalized resistance measured between source and drain electrodes as a function of channel length at different gate voltages (transfer length method). The magnitude of the contact resistance depends on the bias condition.

In a bottom contact architecture, the contact resistance is caused by an enhanced disorder of the deposited semiconductor in proximity of the electrodes (Fig. 1.9). In a top contact configuration, it is due to the distance covered by the injected carriers, through the low-conductivity material towards the accumulation channel. However, the latter configuration, i.e. putting source and drain contacts on top of the semiconductor, often results in increased mobility, thanks to an improved crystalline order at device interfaces.

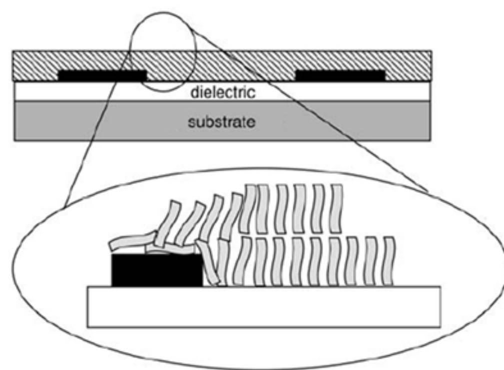


**Figure 1.9.** Effect of bottom contacts on molecular ordering in organic semiconductors.

An additional contribution to performance degeneration is induced by the parallel conductance through the organic semiconductor film. Even if the semiconductor in an OTFT can be as thin as one monolayer, mechanical and chemical stability should be assured and the active layer is grown thicker. This phenomenon results in a reduction of the on/off ratio of the device.

A further shortcoming could be the leakage current through the insulator layer. In high-mobility materials, such as silicon in the MOSFET geometry, gate currents can be considered negligible compared with channel currents. On the contrary, for most organic materials, which have low mobilities, the channel currents are small and requirements on the insulator are stronger. Undesirable currents come from the electrodes, from the gate over the entire plate and in the channel area. As solution to minimize leakage, a guard ring could be placed around the device which is then grounded. Alternatively, the active layer could be patterned, avoiding to deposit semiconductor material outside the channel region.

## 1.4 Fabrication

Organic materials can be deposited by vapor deposition or by solution processing. A vapor deposited organic semiconductor generally yields higher thin-film transistor performances, whereas solution processing is preferred for high-volume and low-cost production.

Small molecular organic semiconductors are deposited using vacuum thermal evaporation. This traditional method preserves the purity of source material, provides the possibility to deposit films with monolayer precision and, in some cases, up to 50% material utilization efficiency. The chamber pressure during thermal evaporation is maintained lower than $10^{-6}$ mbar, thanks to mechanical and turbomolecular pumps. The film thickness is monitored with a quartz-crystal microbalance.

Many organic thin film-based devices require the active layers to be patterned in the substrate plane. Examples are the semiconductor film of a transistor, in order to reduce the leakage currents, and the subpixels of an OLED, in order to obtain a full color display. This aim is typically accomplished by depositing the materials through a shadow mask, which is a metal foil punched with holes reproducing the device pattern.

However, the fabrication by thermal evaporation is not suitable for commercial-scale deposition of organic devices, because of some limiting characteristics, such as strong dependence of evaporation rate on temperature and nonuniform heating of the source material.

Conjugated polymers can only be processed from solution. Spin-coating is one of the simplest methods. The procedure starts with the dispersion of an amount of solution on the substrate. Then, the substrate, which can be either flexible or rigid, is rotated to a preset speed, which lets the solution to spread outwards with the resultant thin film formation. The process completes with film baking or photo-curing, to favor the residual solvent evaporation and increase the film stability.

# 1.5 Materials

The materials used in the fabrication of organic TFTs and the device design play a crucial role in achieving the required performance. The selection of the transistor architecture has a significant effect on electrical characteristics, because of differences in charge injection. However, this choice is often limited by the restrictions in processing methods or the incompatibility of the materials used in the fabrication. Thus, important factors in tuning device performance are choice and optimization of the materials.

If an ordered organic semiconductor promises performance comparable or better than amorphous silicon and a proper metal can assure an effective charge injection from electrodes, the insulator is the material which maybe plays the greatest role on device performance. The capacitance of gate dielectric layer determines the operating voltage of the transistor. In an OTFT with bottom gate configuration, the dielectric layer provides the surface on which the organic semiconductor is deposited, determining its molecular growth and orientation and, above all, the characteristics and quality of the insulator-semiconductor interface, where the conducting channel is formed.

A review of the insulating materials and organic semiconductor used in the fabricated devices is now reported.

## 1.5.1 Gate dielectrics

Various dielectric materials were employed. As inorganic insulator, silicon dioxide was used. It is thermally grown on single-crystalline silicon. Thanks to the availability of silicon wafers and the combination with oxide, this system remains an attractive expedient for the realization of gate and dielectric layer also in organic transistors. Despite a number of excellent properties, $SiO_2$ suffers from a relatively low dielectric constant which causes high operating voltages.

As an alternative to the silicon oxide, organic dielectrics were tested, in particular, both commercial and innovative polymers. They showed higher dielectric constants, provided smooth films on glass

substrates and, thanks to their transparency to a wide range of wavelengths, were also suitable for optoelectronic measurements. They were deposited by solution through the simple process of spin-coating. Some of them, after the deposition, required an additional temperature or irradiation step to produce the final film.

The first polymer evaluated was the Poly(methyl methacrylate) (Fig. 1.10a), known as PMMA and already used as electronic photoresist. It is appreciated in electronic applications when transparency is needed. Thanks to its surface energy, PMMA promotes the growth of organic semiconductor with a large grain size.

The disadvantage met with the use of PMMA was the gate leakage through the insulator film. This problem was overcome by the use of the copolymer Poly(4-vinyl phenol-co-methyl methacrylate) (Fig. 1.10b), or PVP-co-PMMA. In this insulator the insertion of methyl-methacryl groups into the PVP polymer backbone prevents water adsorption at the polymer surface and diffusion into it, as well as interactions with other polar molecules and mobile ions.

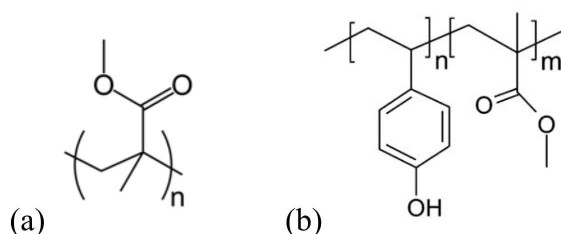


**Figure 1.10.** Monomer units of PMMA (a) and PVP-co-PMMA (b).

Finally, an innovative polymer, D0150, was exploited for the fabrication of OTFTs with an improved stability. This material is a photocurable ActivInk, specifically synthesized in the laboratories of Polyera Corporation. The polymer layer, after deposition by spin-coating, was crosslinked with UV radiation at $\lambda$=300 nm (Fig. 1.11), using varied curing times (0-12 min). The resulting film was very smooth (RMS roughness < 0.3 nm) and exhibited very low gate leakage current densities (<$10^{-8}$ $Acm^{-2}$ at 3.3 $MVcm^{-1}$). The degree of bulk crosslinking was monitored by the optical absorption spectroscopy (Fig. 1.12) of the corresponding film irradiated on quartz substrates. In particular, the progressive absorbance decrease of the peak at $\lambda$~270 nm, assigned to the cynnamoyl fragment, with curing time

proved the progress of the photoinduced cycloaddition process. The film was fully crosslinked only after about 12 min of irradiation.

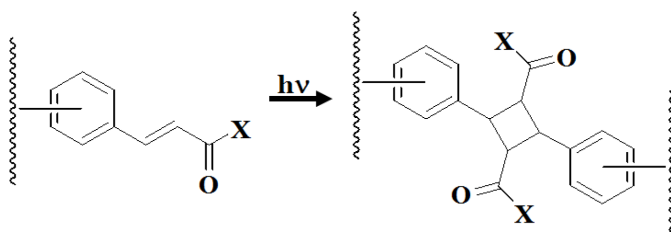


**Figure 1.11.** Schematic of the cycloaddition reaction occurring in ActivInk D0150 film via photocrosslinking.

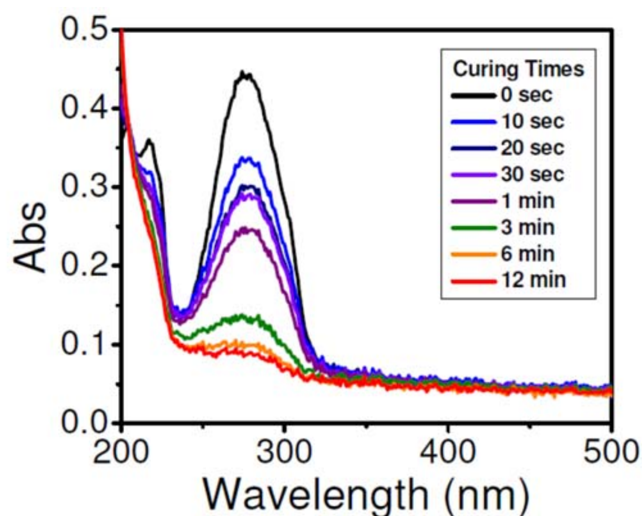


**Figure 1.12.** Optical spectra of a 40 nm thick D0150 film on a quartz substrate irradiated for the indicated curing times.

## 1.5.2 Pentacene

Pentacene is the organic small molecule used for the realization of the active layer of the OTFTs. Pentacene films were grown by vacuum vapor deposition, in order to control important parameters such as the chamber pressure, the substrate temperature and the deposition rate, and at the same time to allow an improved purification of the starting material.

Pentacene is one of the most important organic semiconductors. It is exploited in many applications thanks to its native solid-state order and emerges as the most widely used p-type active layer in OTFTs. It is a planar aromatic molecule, consisting of five benzene rings fused in series (Fig. 1.13).

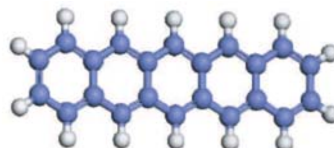

**Figure 1.13.** Molecular structure of pentacene.

Thermally evaporated pentacene mainly deposits in polycrystalline films, with the long axis roughly perpendicular to the substrate. The structure is dominated by strong two-dimensional edge-to-face interactions leading to a packing of molecules in a herringbone arrangement [4]. However, the morphology depends on the substrate temperature during deposition (Fig. 1.14) [5]. It has been reported that, by keeping the substrate close to -196 °C, an amorphous film, practically insulating, is produced. When the substrate temperature is kept at RT, a very highly ordered film is deposited, assuming the so-called thin-film phase. At higher temperatures, a mixture of the thin film phase and the single crystal phase is grown, causing the mobility to decrease, probably due to the high defect concentration resulting from the coexistence of the two phases.

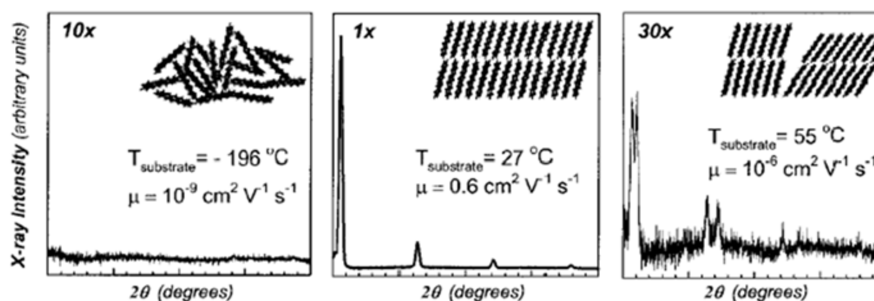


**Figure 1.14.** X-ray diffraction spectra of pentacene films deposited at different temperatures of the substrate. From Ref. [5]

OTFTs fabricated with pentacene as active layer exhibit on the average a reliable hole mobility of about 1 cm$^2$V$^{-1}$s$^{-1}$, but also higher

mobility are reported, up to 60 $cm^2V^{-1}s^{-1}$ measured in single crystals. Disadvantages include its insolubility and its susceptibility to degradation. A better organization of the molecules can be achieved by modifying the surface of the insulator, through particular chemical treatments or with the interposition of an organic film or a self-assembled monolayer (SAM) prior to the pentacene deposition.

In the fabricated devices, an efficient hole-injection in pentacene was achieved through the deposition of gold as source and drain electrodes, because it has a high work function (about 5.1 eV) close to the HOMO level of pentacene.

# References

1. M. Schwoerer, and H. C. Wolf, *Organic Molecular Solids* (Wiley, 2007)
2. G. Horowitz, J. Mater. Res. **19**, 1946 (2004)
3. P.V. Necliudov, M.S. Shur, D.J. Gundlach, and T.N. Jackson, J. Appl. Phys. **88**, 6594 (2000)
4. H. Klauk (Ed.), *Organic Electronics – Materials, Manufacturing, and Applications* (Wiley, 2006)
5. C. D. Dimitrakopoulos, and P. R. L. Malenfant, Adv. Mat. **14**, 99 (2002)

# Chapter 2

# Defects in organic semiconductors

Organic materials have a large density of localized states and electronic transport is always characterized by the capture of the involved charge carriers in these states. Such trapped carriers may be released after a specific retention period or may recombine with carriers of opposite charge sign. In case the release rate is higher than the recombination rate, the localized state is defined as a trap, while for a dominant recombination rate, the localized state forms a recombination center.

Since trapped charge carriers do not contribute to current, traps strongly affect the charge transport properties and lead to complex behaviors in electronic devices.

A trapped charge, similarly to a dopant, can be seen as a charge with zero mobility and not contributing to current. Both a trap and a dopant level communicate to a band; as ionized dopants are compensated by free charge to maintain charge neutrality, a charge on a trap will be compensated by a charge of opposite sign in the band. However, the interaction with bands are different. For instance, a positive charge on a trap empties to the valence band, while a positively ionized donor receives an electron from the conduction band:

$$\begin{aligned} T^0 + h &\leftrightarrow T^+ \\ D^0 &\leftrightarrow D^+ + e \end{aligned} \tag{2.1}$$

that is, a dopant becomes neutral when capturing the charge from the band, whereas a trap becomes charged when a charge is captured [1].

The presence of traps can manifest in many ways in the electrical characteristics of OTFTs. It reduces the effective charge carrier mobility, introduces nonlinear effects in the current characteristics, makes the mobility dependent on temperature and bias, causes instabilities in the transient operation, induces hysteresis phenomena

and leads to performance degradation, along with threshold voltage shift in bias stress condition.

## 2.1 Basic mechanisms in organic semiconductors

In organic semiconductors the width of the transport bands can be very narrow. Especially in amorphous films, extended states are rarely observed and the density of states is well represented by a Gaussian-like distribution of localized molecular orbitals of individual molecules.

Traps are favorite energy sites situated in the energy gap of the semiconductor. Besides the traps formed by the tails of the HOMO and LUMO distributions, there may exist additional trap states at a discrete energy level or with any arbitrary energy distribution in the gap (Fig. 2.1).

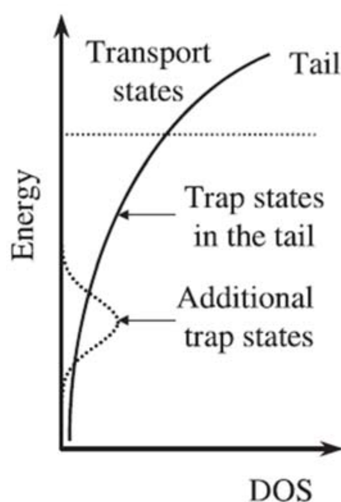


**Figure 2.1.** Transport states, trap states in the tail and additional trap states.

As will be described below, the physical mechanisms responsible for charge carrier transport and excitation in organic semiconductors, as well as charge injection at a metal-organic interface, are dominated by the presence of localized states.

### 2.1.1 Optical properties

The optical properties, absorption and luminescence spectra, of organic molecular solids, in first approximation, can be considered very similar to those in gas phase or in solution. This follows from the fact that the intermolecular forces in crystals are relatively weak in comparison to the binding forces within the molecules. In particular, an important role is played by intramolecular vibrations. However, solid state spectra can differ in detail with respect to selection rules, oscillator strength and energetic position. In addition, the packing of molecules in the crystal structure may produce a pronounced anisotropy, while the disorder usually yields a considerable spectral broadening.

In contrast to inorganic counterparts, organic semiconductors are characterized by the existence of well-defined spin states (singlet and triplet) like in isolated molecules. Furthermore, the optical excitations (excitons), generated via the absorption of a photon, are usually localized on one molecule. The energetic difference between an excited state sitting on one molecule, also called a Frenkel exciton, and a pair of uncorrelated negative and positive carriers sitting on different far apart molecules defines the exciton binding energy (Fig. 2.2). Typical values are from 0.5 to 1 eV [2].

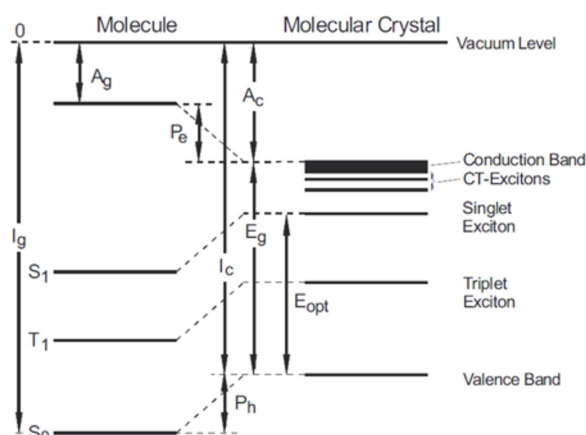


**Figure 2.2.** Energy levels of an isolated molecule and a molecular crystal. $I_g$ and $A_g$ denote the ionization potential and electron affinity in the gas phase, $I_c$ and $A_c$ the respective quantities in the crystal. Due to the polarization energies, $P_h$ and $P_e$, charged states are stabilized in the crystal. $E_g$ is the single particle gap being relevant for charge carrier generation, whereas $E_{opt}$ denotes the optical gap measured in absorption and luminescence. Their difference is the exciton binding energy. From Ref. [2].

### 2.1.2 Charge carrier transport

The charge carrier transport mechanism in organic semiconductors can fall between two extreme cases: band transport, although with a weak electronic delocalization, typically observed in highly purified molecular crystals, and hopping transport, prevalent in amorphous organic solids. In the first case, the temperature dependence of mobility follows a power law behavior as $\mu \sim T^{-n}$; in the other case, an activated behavior is exhibited, along with a dependence on electric field.

The hopping motion (Fig. 2.3) can be described by the Marcus theory [3], which defines the electron transfer rate between neighboring molecules, *k*, in term of the reorganization energy $\lambda$ and the electronic charge-transfer integral $V_{ab}$, related to the electronic coupling factor, between the hopping sites *a* and *b*. In the case of temperature sufficiently high to let the vibrational modes be treated classically, the transfer rate is:

$$k = \frac{4\pi^2}{h} V_{ab}^2 \frac{exp\left(-\lambda / 4k_B T\right)}{\sqrt{4\pi\lambda k_B T}}, \tag{2.2}$$

where $k_B$ is the Boltzmann constant, *T* is the absolute temperature and *h* is the Planck constant. From the knowledge of the transfer rate, the diffusion coefficient, *D*, for charge carriers can be determined through the relationship:

$$D = a^2 k, \tag{2.3}$$

where *a* is the average hopping distance, and consequently the carrier mobility, $\mu$, can be estimated from the Einstein relation:

$$\mu = \frac{qD}{k_B T}, \tag{2.4}$$

where *q* is the charge of an electron.

Another theory, the Poole-Frenkel model [4], focuses on the influence of an external applied field (Fig. 2.3) and was found to well

describe the charge transport in many organic systems. The field dependence of charge carrier drift mobility has the form:

$$\mu = \mu_0 exp\left(\beta_{PF}\sqrt{F}\right), \tag{2.5}$$

where $\mu_0$ is the zero-field mobility, $F$ the electric field, $\varepsilon$ the dielectric constant, $\beta_{PF}$ the Poole-Frenkel slope.

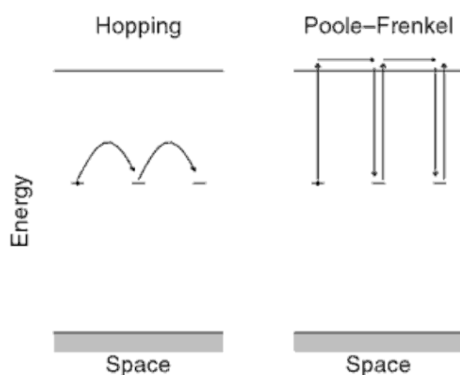


**Figure 2.3.** Schemes of charge transport according the hopping model and the Poole-Frenkel model.

A more precise theory for hopping charge transport is the Gaussian disorder model (GDM), proposed by Bässler [5], and it is widely used for amorphous organic solids. It makes reference to the Gaussian distributions characterizing the transport site energies and separations (Fig. 2.4). The model equation takes into account the dependence on both electric field and temperature:

$$\mu(F,T) = \mu_\infty exp\left[-\left(\frac{2\sigma}{3k_B T}\right)^2\right] exp\left(\beta\sqrt{F}\right), \tag{2.6}$$

where $\mu_\infty$ is the high temperature limit of the mobility, $\sigma$ is the energetic disorder, related to the width of the Gaussian distribution of the density of energy states for the transport sites, and $\beta$ is a factor depending on the geometric randomness arising from structural or chemical defects.

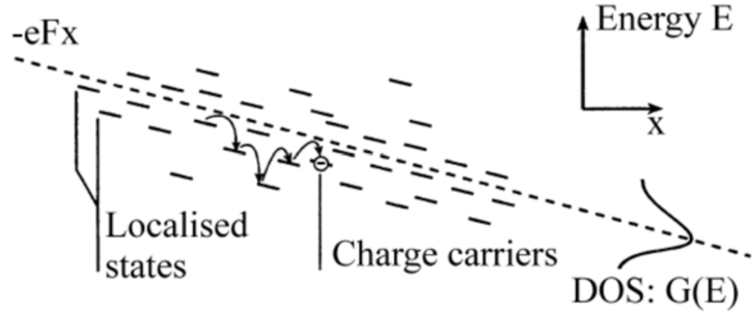


**Figure 2.4.** Representation of the charge transport model in amorphous organic solid, according to the Bässler model.

The concept of variable-range hopping (VHR) was developed in 1998 by Vissenberg and Matters [6]. According to this theory, a carrier may either hop over a small distance with a high activation energy or hop over a long distance with a low activation energy. Thus, the temperature dependence of the carrier transport is strongly dependent on the density of localized states.

A balanced situation between the two extreme mechanisms of band and hopping transport is defined by the multiple trapping and release (MTR) model. The localized states are distinguished in deep traps, which are located near the center of the band gap, and shallow traps, located close to the conduction or valence band, separated by no more than a few *kT*. In particular, the charge captured in a deep trap cannot be released by thermal excitation, while if trapped in a shallow level the charge could be release through a thermally activated process. Thus, when the charge carriers are multiply trapped by and thermally released from trap states associated with the defects, an effective, or apparent, mobility [7] can be introduced:

$$\mu_{eff} = \mu_0 \frac{n_f}{n_f + n_t} \approx \frac{\mu_0}{1 + \frac{N_t}{N_C} \exp\left( \frac{E_C - E_T}{k_B T} \right)}, \tag{2.7}$$

where $n_f$ and $n_t$ are the density of the free and trapped charge carriers, respectively, $\mu_0$ is the intrinsic mobility, $N_C$ is the effective density of extended states at an energy $E_C$, $N_t$ is the concentration of localized states at a specific energy $E_t$.

### 2.1.3 Charge carrier injection

The charge injection process is dominated by the charge injection barrier at the interfaces between the active layer and the metal electrodes. The barrier height is defined by the separation between the Fermi level of the electrode and the HOMO/LUMO of the organic layer. Three mechanisms can be considered to describe the injection process: the field-assisted thermoionic injection where the carriers from the electrode are thermally excited to overcome the barrier, deriving from the superimposition of the image charge potential and external field; the Fowler-Nordheim tunneling injection in which the carriers tunnel through the potential injection barrier under a high electric field; the thermoactivated hopping injection, when the carriers hop from the metal Fermi level into the localized states of the organic semiconductor.

For an effective injection it become fundamental to assure the alignment of the energy level at the metal-organic interfaces. The molecular-level alignment at interfaces in early days was believed to obey the classical Mott-Schottky model, which assumes that no interaction occurs at the interface. In this case, the molecular energy level positioning follows the alignment of vacuum level and the barrier heights for electrons, $\phi_e$, and holes, $\phi_h$, are:

$$\phi_e = \Phi_m - A_e, \tag{2.8a}$$

$$\phi_h = I_p - \Phi_m, \tag{2.8b}$$

where $\Phi_m$ is the metal work function, i.e. the difference between the Fermi level and vacuum level, $A_e$ is the electron affinity, i.e. the minimum energy required to form a negative ion, and $I_p$ is the ionization potential, that is the minimum energy required to bring an electron from the HOMO to the vacuum to form a positive ion.

It should be noted that for the estimation of the carrier injection barrier height, it is more appropriate to consider the charge-transport gap ($E_g$), that is, the energy separation of the HOMO and the LUMO levels involved in the electron injection process, obtained by the combination of UPS (ultraviolet photoelectron spectroscopy) and IPES (inverse photoemission spectroscopy) techniques, rather than the optical bang gap ($E_{opt}$), determined by the absorption spectroscopy.

However, a common vacuum level is not achieved in most metal-organic interfaces, but it is discontinuous at the interface due to the formation of a dipole layer (Fig. 2.5). In particular, an abrupt change Δ was observed experimentally right across the interface, through various UPS and Kelvin probe works. This dipole modifies the interface barriers as follows:

$$\phi_e = \Phi_m - A_e - \Delta \, , \tag{2.9a}$$

$$\phi_h = I_p - \Phi_m + \Delta \, . \tag{2.9b}$$

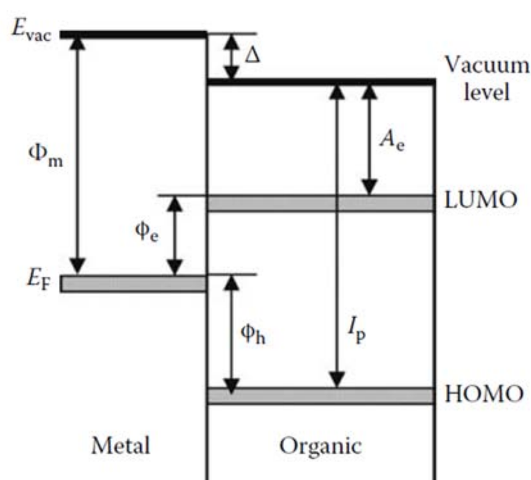


**Figure 2.5.** Schematic energy diagram of a metal-organic interface, including the presence of an interface dipole. $\Phi_m$ is the metal work function, $I_p$ is the ionization potential, $A_e$ is the electron affinity, and $\Delta$ is the vacuum level shift due to the interface dipole. Band bending effects are not considered.

The origin of this phenomenon is not fully clear but some interpretations were proposed, including: electron transfer between the metal and the organic layer, image force effect, chemical interactions that could lead to the rearrangement of new bonds, existence of interfacial states and permanent dipole moment (Fig. 2.6). If the barrier height is reduced, carriers can freely inject into the organic solid and the interface behaves as an ohmic contact, i.e. a reservoir of free carriers large enough to supply the maximum charge capacity at a given applied

voltage. In this case, the current-voltage characteristics exhibited a bulk-controlled behavior.

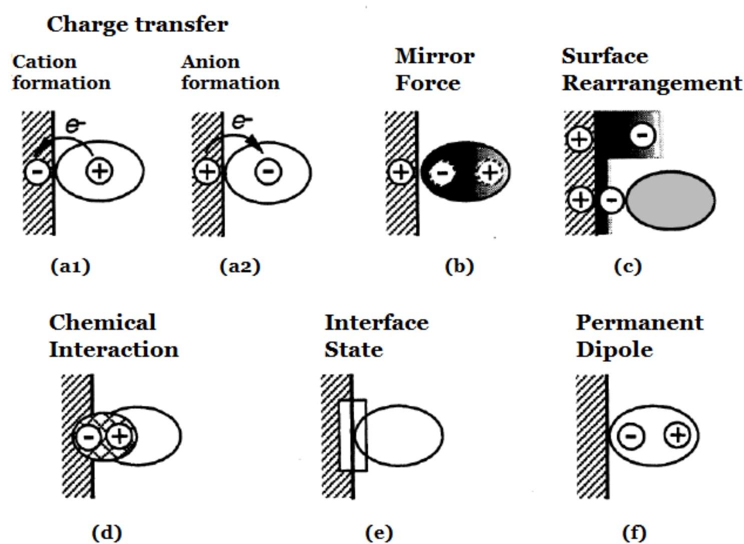


**Figure 2.6.** Possible factors forming and affecting the interfacial dipole layer: (a) charge transfer across the interface, (b) concentration of electrons in the adsorbate leading to positive charging of the vacuum side, (c) rearrangement of electron cloud at the metal surface, with the reduction of tailing into vacuum, (d) strong chemical interaction between the surface and the adsorbate leading to the rearrangement of the electronic cloud and the molecular geometries, (e) existence of interface state serving as a buffer of charge carriers, (f) orientation of polar molecules or functional groups. From Ref. [8]

## 2.2 Bias stress

The success of organic semiconductors in the marketplace depends critically on the ability of these materials to sustain their electrical performance under operation. However, various challenges should be overcome for the future development of organic electronics. They deal especially with the electrical instability, also called bias stress, which comes up with a decay of the output current over the protracted operation of the transistor.

Bias stress can be associated with either a structural degradation of the semiconductor material or a trapping of mobile charge in nonconducting states. Sustained application of bias can eventually cause the charges to be removed from conductive states and to be captured on the trap states.

These mechanisms are usually observed through the time dependence of effective carrier mobility and threshold voltage. In detail, the structural degradation leads to a decrease of mobility, while the charge trapping induces a threshold voltage shift with no change in mobility. Trapping can occur in the semiconductor, in the gate dielectric or at the insulator-semiconductor interface. Since all the induced charge is located within the ~1 nm from the dielectric interface, the major effects occur near this interface. However, most mechanisms of bias stress in organic semiconductor remain unknown.

In pentacene transistors, bias stress has been studied in terms of hysteresis and translation of I-V characteristics. Positive and negative $V_T$ shifts have been observed depending on the sign of the persistent applied gate voltage [9], while little dependence on the gate dielectric has been revealed, suggesting that trapping, responsible for degradation, occurs in the pentacene semiconductor. The process proposed as the origin of bias stress in pentacene is the formation of hydrogen-induced traps has been proposed [10].

Particular behaviors are observed under photo-excitation. Optical interactions can have major effects on the structural properties of deep-level defects, in contrast to shallow ones. When light causes an electronic excitation of a localized defect, the alteration of the electron wavefunction induces changes, in the surrounding distribution of electronic charge, which cause movement of the neighboring atoms. The new configuration induced by an electronic excitation may not be stable. If the excited electronic state with the new configuration can promptly (relative to the observation time) relax back to the ground state, it is not stable. If some properties inhibiting relaxation to the ground state exist, the new configuration is metastable (Fig. 2.7), so that it will endure long enough to be observable. This means that between ground and excited electronic states there are energy barriers to be overcome.

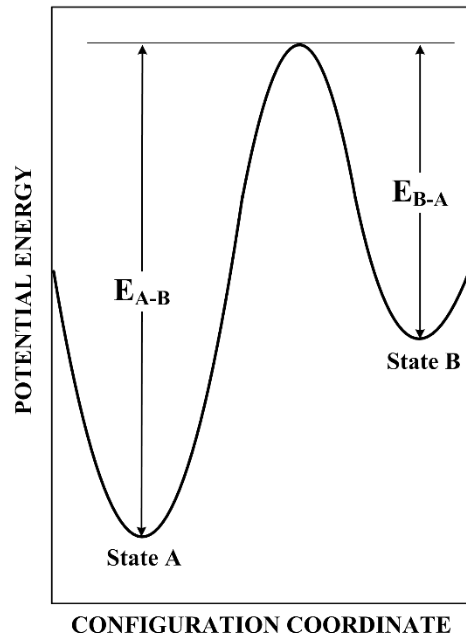


**Figure 2.7.** Double-well scheme of a metastable defect in a configuration coordinate diagram. In equilibrium, most of the defects are in ground state A and can be excited to the metastable state B. The transitions proceed over the barrier heights.

## 2.3 Origin of defects

The stability of organic semiconductors can be compromise by the presence of both structural defects and impurities. Unfortunately, an accurate estimate of defect origins and reaction mechanisms is difficult, with the consequence that device performance is usually uncontrollable and unpredictable.

The defects may assume a variety of forms: native point defects, such as vacancies or interstitials; point defects for the presence of isolated impurities; defect complexes formed by the special correlations between different point defects, such as impurity-vacancy pairs; line defects, such as dislocations; defects associated with grain boundaries or with the existence of an interface.

Structural imperfections can arise as a result of chemical synthesis. They are present in the structure of the main chain of molecules, due to asymmetric and coupling reactions. Furthermore, since it is nearly impossible to obtain a fully pure sample, an organic small molecule or polymer consists of a distribution of molecular species with different molecular weights. Such a distribution leads to an inherent microstructural disorder, limiting the crystallization of organic thin films. The HOMO and LUMO levels are not only determined by the chemical structure of the molecule itself but also by the electronic polarization of its surrounding. Since structural imperfections lead to fluctuating surroundings, a distribution of levels has to be expected. In a polycrystalline layer, where a specific kind of structural defect occurs with enhanced probability on grain boundaries, structural defects may result in more or less discrete trap states deep in the gap.

Chemical defects are also induced by the reactions promoted under ambient conditions, because of the presence of light and molecular oxygen (Fig. 2.8).

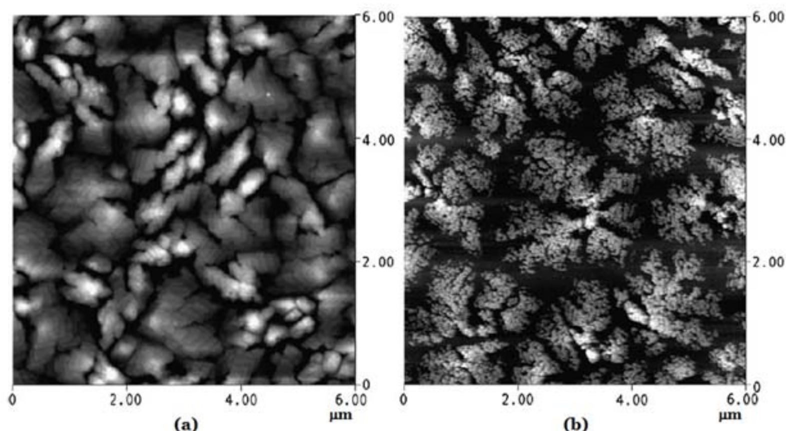


**Figure 2.8.** AFM images of a 12 nm thick pentacene film on $SiO_2$ in its pristine state (a) and after 26 h UV exposure in air. From Ref. [11]

Organic molecules generally exhibit stable performance under vacuum conditions, but many molecules are also kinetically unreactive with $O_2$, when it is in its ground state, even though oxidation is a thermodynamically favorable process. The reason is that the ground state of $O_2$ has a triplet spin multiplicity while most organic materials have singlet multiplicity. On the contrary, the singlet states of $O_2$ are particularly reactive [11]. Singlet oxygen can be generated by the

photo-excitation to the triplet state and the subsequent intersystem crossing to the singlet electronic states or by the energy transfer from electronically excited organic species. The chemical species that can be created during photo-oxidation are numerous, but the general result of these reactions is a loss in conjugation in the molecule structure. A smaller number of conjugated rings in the chains means a wider HOMO-LUMO gap and a reduction in the number of electrically active states in the material, leading to the decrease of the OTFT mobility.

As regards impurities and dopants, at the present moment, the prediction of charge-transfer process with them is essentially qualitative. In addition, the results of analyses and investigations vary widely and are difficult to compare.

Several experimental studies have suggested oxygen as a dopant for a variety of organic semiconductors [12,13]. Oxygen is at a relatively high concentration under ambient conditions and could interact with conducting organic molecules. Since states appear within the band gap of the material, they will influence the shape of the bandtail, changing the turn-on characteristics of the device. Thus, the effects of doping are most easily appraised in OTFTs in the sub-threshold region (Fig. 2.9).

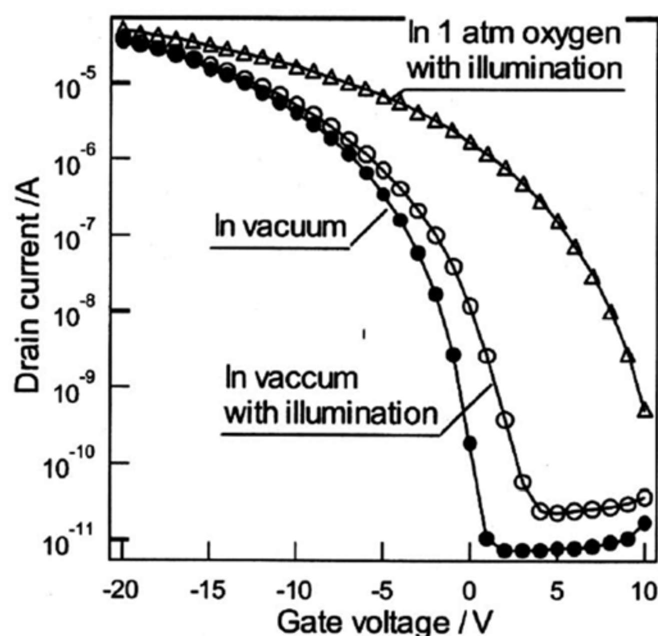


**Figure 2.9.** A comparison of the transfer characteristics of a pentacene transistor under three conditions: in vacuum, in vacuum with illumination and in oxygen atmosphere with illumination. From Ref. [12]

Also water is known to cause electrical instability in organic electronic devices (Fig. 2.10). It can be absorbed by the bulk of the film and interact directly with the accumulated carrier states. In particular, the absorption of humidity worsens the effects induced by gate-bias stress [14].

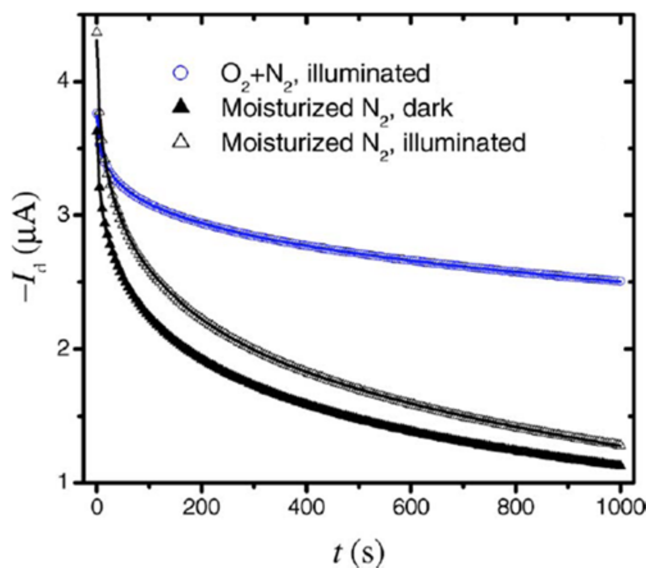


**Figure 2.10.** Time domain data of three pentacene-based OTFTs measured under various ambient and illumination conditions. From Ref. [14]

Water increases off-state conduction and causes a lack of saturation in the output characteristics. Usually, over the absorption of water, the measured carrier mobility remains relatively unaffected, but deeper trap states are formed.

Further elements able to affect the current in an OTFT are organic solvents, in case spin-coating is adopted for the deposition process of organic films. The effects of solvent adsorption are attributed to charge trapping at grain boundaries in the films.

Molecular deformations are also induced by geminate pairs and self-trapping mechanisms [2]. A geminate pair is formed by a hole and an electron, which underlie a Coulomb interaction even if several molecules separate them. If the recombination probability between the hole and the electron is limited, a geminate pair creates a Coulomb trap. Self-trapping is the trapping mechanism which occurs in polymers when the charge carrier forms its own trap state on the polymer chain.

The origin is the molecular deformation, and the subsequent lowering in energy, for the presence of an excess charge on an organic molecule. A carrier together with its produced molecular deformation has already been referred to as a polaron; if two charge carriers share the same molecular deformation a bipolaron is formed. These quasi-particles may have such a low mobility to be considered not mobile.

## 2.4 Effects of defects on OTFT electrical properties

Structural defects, such as dangling bonds, and chemical impurities, such as atomic substitution of heteroatoms, have been demonstrated to have a significant role in the electrical behavior of amorphous inorganic semiconductors. Semiconducting polymers and small molecules also contain defects and impurities, but there are important differences between their origin and how they can be controlled compared with inorganic materials. A discussion on the effects of chemical defects and impurities on the electrical performance of OTFTs is reported.

### 2.4.1 Effects on threshold voltage

Mobile charges induced in the conductive bands to compensate immobile charge species can affect the threshold voltage. For instance, let consider a p-type OTFT, i.e. hole mobility is higher than electron mobility, characterized by the presence of a trap that can capture and immobilize the holes. In this case, a certain trapped positive charge density, $N_T^+$, is present and it is compensated by free electrons. It results in a change of threshold voltage, because an extra bias has to be applied to the gate in order to remove this charge (Fig. 2.11) [15]. In this particular case, an additional negative bias is needed so that holes, attracted to the valence band, could form a conductive channel. Thus, the shift in threshold voltage in an OTFT is proportional to the trapped charge density:

$$\Delta V_T = -\frac{qN_T^+}{C_i}, \tag{2.10}$$

where $q$ is the electron charge and $C_i$ is the insulator capacitance.

The description is more complicated if the occupancy of the traps depends on the bias. Indeed, the gate bias can sweep the Fermi level through the energy diagram and therefore change the occupancy of any states passing under it. The result is not simply the introduction of an extra voltage to the gate, but also a bias dependence of effective mobility and an alteration of the characteristic curves.

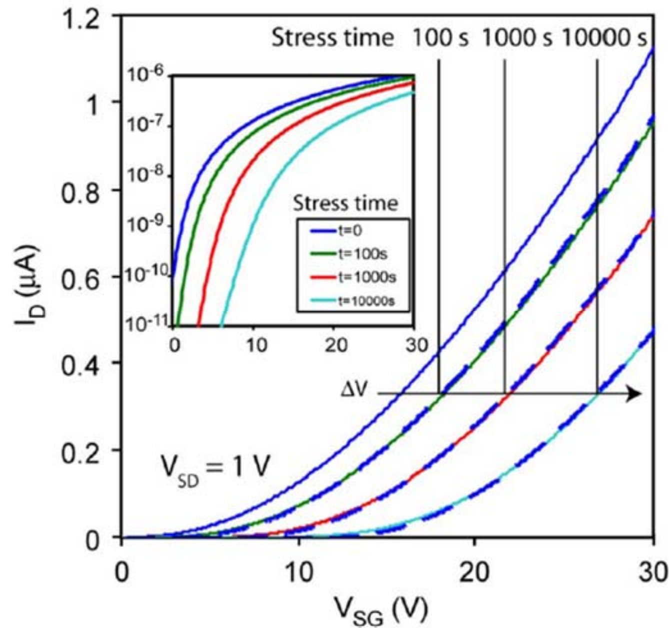


**Figure 2.11.** Transfer characteristics after bias stress at $V_{GS}$=30 V and $V_{DS}$=1 V at varying stress times. Inset: semilogarithmic plot. From Ref. [15]

## 2.4.2 Effects on mobility

When a gate voltage is applied, charges accumulate in the semiconducting layer region that is close to the insulator. As these accumulated charge carriers fill the lower-lying states, any additional charges induced in the accumulation layer will occupy states at a relatively high energy, and a lower activation energy will be required to hop away to a neighbor site. This mechanism results in a higher

mobility with increasing gate voltage and a subsequent deviation of electrical characteristics from the ideal curves. According to the VRH model, given an exponential distribution of localized state:

$$g(\mathrm{E}) = \frac{N_t}{kT_0} \exp\left(\frac{E}{kT_0}\right), \tag{2.11}$$

with a number of states per unit volume $N_t$ and a width $T_0$, the field-effect mobility shows a bias and temperature dependence following this relationship:

$$\mu_{FE} \sim \left[\frac{\left(C_i V_{GS}\right)^2}{2kT_0 \varepsilon_S}\right]^{T_0/T-1}. \tag{2.12}$$

## 2.4.3 Type of conduction

Defects seems to be responsible also for the difference between the mobility of negative charges and that of positive charges. In semiconducting polymers and small molecules, electron mobility is typically much smaller than hole mobility. Transport in organic π-conjugated compounds occurs thanks to the transfer of single positive and negative charges, i.e. holes and electrons, between the π orbitals of adjacent molecular units. Thus, it is expected that the mobilities of electrons and holes differ slightly, as it happens in traditional inorganic semiconductors where the difference is less than a factor of five. In contrast, without any fundamental reason, organic semiconductors typically show highly asymmetric electron and hole mobilities. Indeed, most organic semiconductor materials are intrinsically p-type, that is, the hole mobility exceeds the electron mobility by orders of magnitude. Plenty of materials suit to make p-type transistors, whereas n-type devices, needed to compensate the electronic architectures, such as in CMOS technology, are less common.

When molecular crystals from naphthalene, anthracene or pentacene were investigated, a temperature activated transport was observed but it was not immediately clear whether charge transport would take place in delocalized bands or hopping transport would prevail. Later, it turned out that band transport prevailed in ultrapure

and well-ordered crystals, while charge mobility was limited by trapping in less pure samples. Recently, a paper published on Nature Materials [16] clarified the possible origin of the discrepancy in mobility values between holes and electrons. Here Nicolai and co-workers investigated the trapping mechanisms in a wide range of semiconducting polymers. They showed that transport of electrons was limited by trapping and that the trap states were similar in all these materials. They managed to identify a common energy level of about -3.6 eV versus vacuum, as the most likely trap due to an oxygen-water complex universally present in organic materials.

For most organic semiconductors, the highest occupied molecular orbital is located around -5 to -6 eV versus vacuum, while the lowest unoccupied molecular orbital ranges from about -2 to -3 eV. Holes move by transfer between the HOMOs of adjacent molecules and can follow an incoherent motion for the presence of higher-lying filled defect levels. However, defects and impurities frequently have empty orbital below -3 eV suitable for localizing the electrons which are hopping between the LUMOs of adjacent molecules (Fig. 2.12).

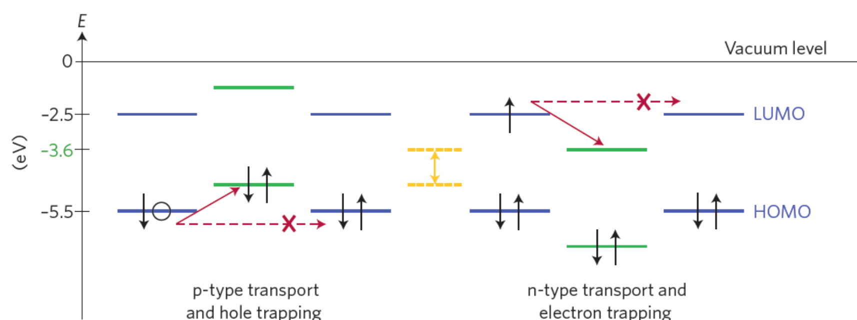


**Figure 2.12.** Energy level diagram illustrating hole and electron trapping in organic semiconductor films. Holes (black circle) and electrons (black arrow) transfer between HOMOs and LUMOs, respectively, of adjacent molecules (blue lines). A filled higher-lying or an empty lower-lying defect level (green lines) can trap holes and electrons, respectively, until they are released by thermal activation. Trap-free ambipolar transport may be observable in small HOMO-LUMO gap materials (yellow lines). From Ref. [17]

Trapping and subsequent thermally activated release reduce the mean mobility of charge carriers. As a consequent, the different susceptibility of electrons and holes to trapping results from the dissimilar energies of the HOMO and LUMO. In order to obtain ambipolar materials with similar high mobilities for electrons and holes,

a small bandgap is needed; otherwise, either electrons or holes will be susceptible to trapping [17].

For the same reason, eliminating electron traps could be an effective solution to design n-type materials. Examples are the electronegative hydroxyl groups at the interfaces between organic semiconductors and gate dielectrics. They were found to be responsible for electron trapping; indeed, when dielectric materials free of hydroxyl groups were used, electron was not inhibited [18]. In this way, n-type transistors could be realized, even with materials that are originally thought to be p-type semiconductors.

# References

1. P. Stallinga, *Electrical Characterization of Organic Electronic Materials and Devices* (Wiley, UK, 2009)
2. W. Brütting (Ed.), *Physics of Organic Semiconductors* (Wiley, Weinheim, 2005)
3. R. A. Marcus, Rev. Mod. Phys. **65**, 3 (1993)
4. J. Frenkel, Phys. Rev. **54**, 647 (1938)
5. H. Bässler, Phys. Stat. Sol. B **175**, 15 (1993)
6. M. C. J. Vissenberg, and M. Matters, Phys. Rev. B **57**, 12964 (1998)
7. K. Ryu, I. Kymissis, V. Bulović, and C.G. Sodini, IEEE Electron Dev. Lett. **26**, 716 (2005)
8. H. Ishii, K. Suguyama, E. Ito, and K. Seki, Adv. Mater. **11**, 605 (1999)
9. D. Knipp, R. A. Street, A. Völkel, and J. Ho, J. Appl. Phys. **93**, 347 (2003)
10. J. E. Northrup, and M. L. Chabinyc, Phys. Rev. B **68**, 041202 (2003)
11. A. Vollmer, H. Weiss, S. Rentenberger, I. Salzmann, J. P. Rabe, N. Koch, Surface Science **600**, 4004 (2006)
12. S. Ogawa, T. Naijo, Y. Kimura, H. Ishii, and M. Niwano, Appl. Phys. Lett. **86**, 252104 (2005)
13. P. K. Naayak, R. Rosenberg, L. Barnea-Nehoshtan, D. Cahen, Organic Electronics **14**, 966 (2013)
14. G. Gu, and M. G. Kane, Appl. Phys. Lett. **92**, 053305 (2008)
15. K. K. Ryu, I. Nausieda, D. D. He, A. I. Akinwande, V. Bulović, and C. G. Sodini, IEEE Trans. Electron Dev. **57**, 1003 (2010)
16. H. T. Nicolai, M. Kuik, G. A. H. Wetzelaer, B. de Boer, C. Campbell, C. Risko, J. L. Brédas, and P. W. M. Blom, Nature Mater. **11**, 882 (2012)

17. A. Köhler, Nature Mater. **11**, 836 (2012)
18. L.-L. Chua, J. Zaumseil, J.-F., E. C.-W. Ou, P. K.-H. Ho, H. Sirringhaus, and R. H. Friend, Nature **434**, 194 (2005)

# Chapter 3

# Metastable light induced effects in pentacene

One of the environmental factor which could affect organic materials was analyzed. Pentacene thin film samples were fabricated and the stability of their electrical properties was monitored when the devices were exposed to different energy light sources.

In recent years pentacene has become one of the most widely studied molecules [1] and has attracted growing attention as an electronic device material, especially in the field of high mobility thin-film transistors (TFTs) and photodetectors. The most appealing properties of the pentacene molecules are the ease to grow thin films on various substrates and the polycrystalline nature leading to high hole mobilities, with values comparable or higher than that of amorphous silicon [2]. However, in organic devices several degradation effects have been observed under continuous bias or temperature stress conditions [3], as well as in the presence of oxygen, water or light [4]. This chapter focused on the effects induced by light irradiation in a pentacene thin film [5]. Steady-state photocurrent spectrum and transient behavior were investigated in order to explore the transport mechanism, the carrier trapping and recombination effects. The disordered structure of a polycrystalline material was demonstrated to lead to a broad distribution of event times characterizing the evolution of its physical properties. Photoconductivity dynamics were revealed to depend on duration of the optical excitation as well as on wavelength. In particular, the modifications induced by ultraviolet irradiation were inspected.

A number of papers have investigated the enhancement of the performances of pentacene-based TFTs as a result of UV light treatments [6, 7]. It was reported that a low energy UV irradiation with a wavelength of 364 nm could enhance the pentacene-based thin-film

transistor conductivity and control the threshold voltage of the device, whereas, after an illumination by high energy UV light at 254 nm, the transistor could show a degraded mobility and lowered saturation current [8]. The mobility degradation of a pentacene TFT induced by a continuous UV light irradiation [9] was directly correlated to the deterioration of the semiconductor crystallinity; to prevent this phenomenon an ultraviolet-protecting $SnO_2$ thin-film encapsulation prepared by ion-beam-assisted deposition was proposed [10].

In this study, anomalous phenomena were revealed for effect of a persistent ultraviolet (UV) irradiation, in particular a photoconductivity degradation under light conditions and a dark recovery were observed at a wavelength of 285 nm. The decrease in the conductivity of pentacene was attributed to the creation of defects, whose evolutions were studied focusing on their metastable nature. The results were reported in terms of a trap density model, which provides a description of the dynamics of light induced electrically active defects in an organic semiconductor.

## 3.1 Photocurrent in a pentacene thin film

A pentacene thin film layer with a thickness of 50 nm was deposited on a glass substrate by thermal evaporation with base vacuum level of $2 \cdot 10^{-7}$ mbar and deposition rate of 0.5 Å/s. The electrodes, consisting of 50 nm thick gold contact pads, were evaporated on the top through a shadow mask leading to resistive samples with length $L$ = 50 µm and width $W$ = 500 µm. Current measurements were performed at a constant 30 V bias voltage, at room temperature and in ambient air, by using a HP/Agilent 4155B semiconductor parameter analyzer. The Ohmic nature of the contacts was confirmed by the I-V characteristics.

In order to study the light induced effects, the devices were illuminated with non-coherent light sources at various wavelengths, placed on the top of the organic semiconductor (Fig. 3.1). The conductivity was recorded for various photon energies of incident light covering the spectrum between 285 nm and 870 nm. Since the LEDs had different intensities, with photon dose varying from $10^{15}$ to $10^{16}$ photons/cm$^2$ per second, a normalization of the measured photo-induced current was then performed.

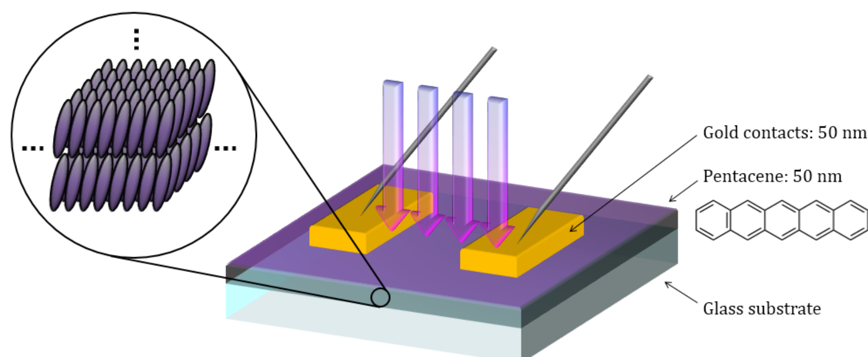


**Figure 3.1**. Structure of a pentacene thin film deposited by thermal evaporation.

To appraise the degree of degradation induced by persistent irradiation, the samples were also exposed to continuous excitation, during which photoinduced current was monitored until steady-state conditions were met. Between consecutive illumination periods with different energies, the samples were kept in the dark for at least 24 hours in order to accurately determine the dark current. During dark periods after irradiation, persistent photocurrent was observed and characterized.

Since the behavior for effect of ultraviolet light appeared to differ significantly from those obtained under other wavelengths, time evolution of the photocurrent under 285 nm irradiation was studied separately, by the use of two different optical power densities, while alternating light and dark periods of equal duration.

LEDs covering a wide range of photon energy levels were used as illumination sources, in order to identify the main excitation mechanisms. Under an excitation with the photon energy condition of $h\nu < E_g$, where $h$ is the Planck constant, $\nu$ denotes the irradiation frequency and $E_g$ the bandgap energy of the material, the photon energy was insufficient to generate a large number of electron-hole pairs in the semiconductor layer, whereas it contributed to the photo-excitation of deep-level impurities. For the case of $h\nu > E_g$, the carrier concentration enhancement was promoted by band-to-band excitation.

The current flowing through the samples immediately after LED switching was measured and a normalization of the photocurrent spectrum by the incident photon density was developed. However, the small transient photo-induced current, measured a short time after

excitation starting, was not taken as an indicative parameter to compare the results of light excitation, since it could be attributed to two mechanisms, either the carrier generation efficiency or the hopping limited drift mobility. The relative contributions of these two factors to the photoresponse could be judged through the analysis of the steady-state photoconductivity results. Therefore, the current was monitored over a long enough period of time to reach a stable value.

The photocurrent, defined as the current increase under light conditions, was given by the photo-induced free carriers, $n_{ph}$, present under stationary conditions in the volume exposed to light and collected at the electrodes with a transit time $t_t$, as follows:

$$I_{ph} = I_{illum} - I_{dark} = \frac{qn_{ph}}{t_t} , \tag{3.1}$$

where $n_{ph} = N_{photons}\eta_\lambda \tau$, and $N_{photons} = \lambda P_{opt} / hc$. $N_{photons}$ is the number of photons incident per second when an optical power $P_{opt}$ is delivered to the sample, $\eta_\lambda$ is the generation efficiency at the wavelength $\lambda$ the emission spectrum of LED is centered at, $\tau$ is the lifetime of light-induced charge carriers defined in the presence of deep trapping or recombination [11], $h$ is Planck's constant and $c$ is the speed of light. From the estimation of the steady-state photocurrent and the flux of incident photons, the quantum efficiency was obtained at various wavelengths:

$$\eta_\lambda G = \frac{I_{ph}}{qN_{photons}} , \tag{3.2}$$

where the photoconductive gain $G = \tau / t_t$ is defined as the ratio of the carrier lifetime to the transit time.

The size of quantum efficiency, defined as the increase in the number of collected carriers per incident photon, estimated from the photocurrent revealed after two hours of continuous irradiation, was reported in Fig. 3.2 and compared with the instantaneous quantities.

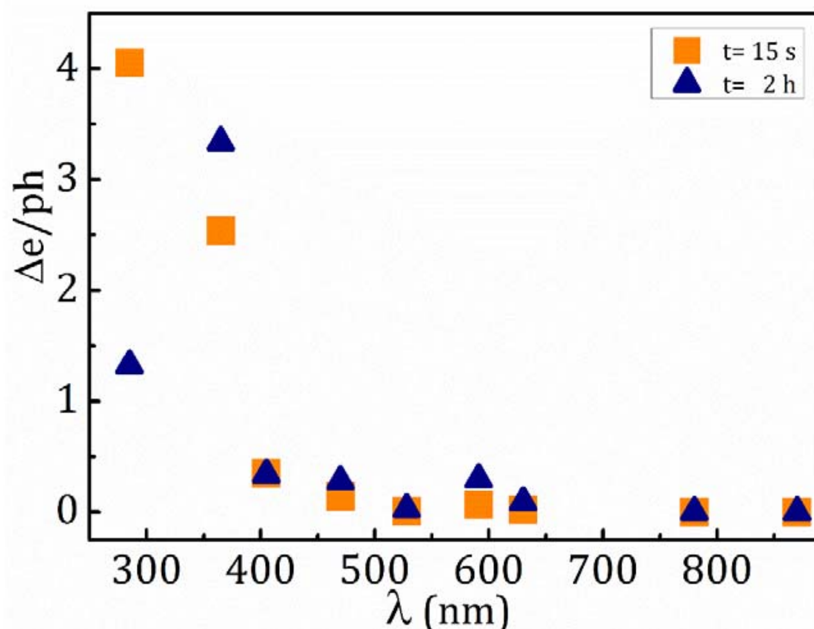


**Figure 3.2.** Increase in the number of collected carriers per incident photon, estimated after 15 s and after 2 hours at different wavelengths in a pentacene thin film.

For all the samples, the spectrum exhibited an intense response in the visible range at 591 nm. Moreover, a high efficiency was observed in the ultraviolet range but the steady-state photocurrent for effect of a UV-light at 285 nm was revealed to be lower than the initial value.

The high sensitivity of pentacene to visible light around 2 eV could be attributed to the fundamental gap between the HOMO and LUMO levels. Indeed, this feature was exploited in the fabrication of organic phototransistors used as efficient red light sensors [12]. The current enhancement in the UV range could be justified by a high energy absorption peak of a pentacene film, located near 300 nm and connected to the molecular-like character [10] of constituent pentacenes. In particular, an optical excitation at a wavelength of 365 nm seemed to increase significantly the carrier density without changing the mobility and, furthermore, with a quantum efficiency greater than unity. Indeed, ultraviolet radiation at medium energy was already used as a treatment in order to improve the performance of pentacene-based thin film transistors, by effectively modulating the threshold voltage thanks to the formation of a more conductive channel [13]. On the contrary, a high energy UV is known to degrade the crystalline quality of a

pentacene film and negatively affect the mobility [10], as it was revealed under prolonged illumination with 285 nm wavelength.

Thus, it was evident that the time evolution till the achievement of the steady-state value depended on the optical energy. Figure 3.3, showing photocurrent behavior during the first 10 minutes of light exposure as a function of the irradiation wavelength, proved that if the light energy was not high, i.e. from infrared to near UV range, an increase in current was induced, due to photogeneration of additional electron-hole pairs. Meanwhile, if light energy was higher, a drop in current was observed after a maximum level had been reached.

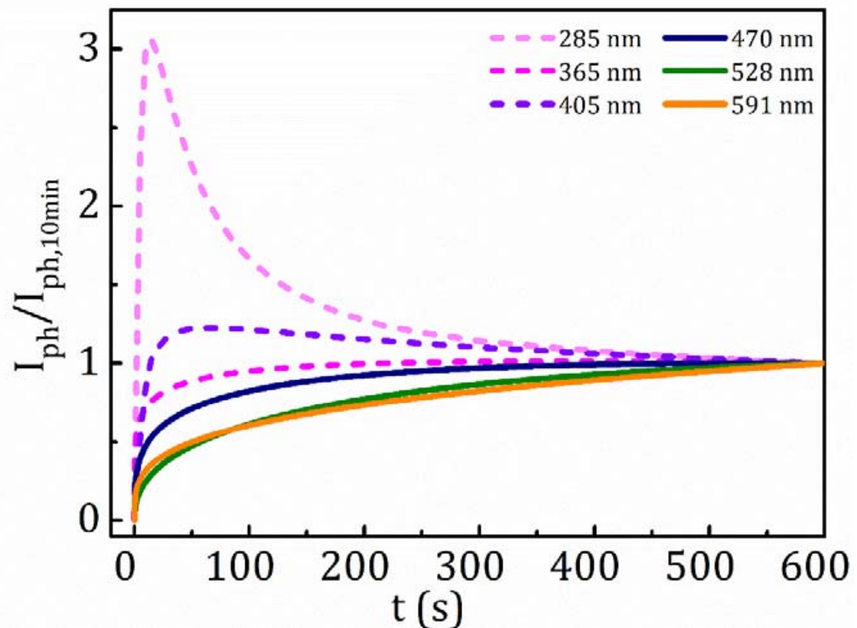


**Figure 3.3.** Persistent photocurrent growth kinetics at room temperature in a pentacene thin film under continuous illumination at various wavelengths. Measured data are normalized to the photocurrent after 10 min.

Original current values were restored only after turning off the light source (inset of Fig. 3.4), even at room temperature, showing a persistent photoconductivity. Measurements of the residual photocurrent developed during post-irradiation dark periods were reported in Fig. 3.4 as a function of excitation energy and normalized to the photocurrent value reached before light termination.

The curves revealed that, for all the wavelengths, the samples exhibited an initial fast decrease followed by a slower and steady decrement, according to a distribution of time constants, characteristic of dispersive rate processes, such as trap-assisted recombination [14] and bimolecular recombination limited by the low charge carrier mobility [15]. However, an ultraviolet light radiation caused the dark conductivity to decrease to a level lower than the original one.

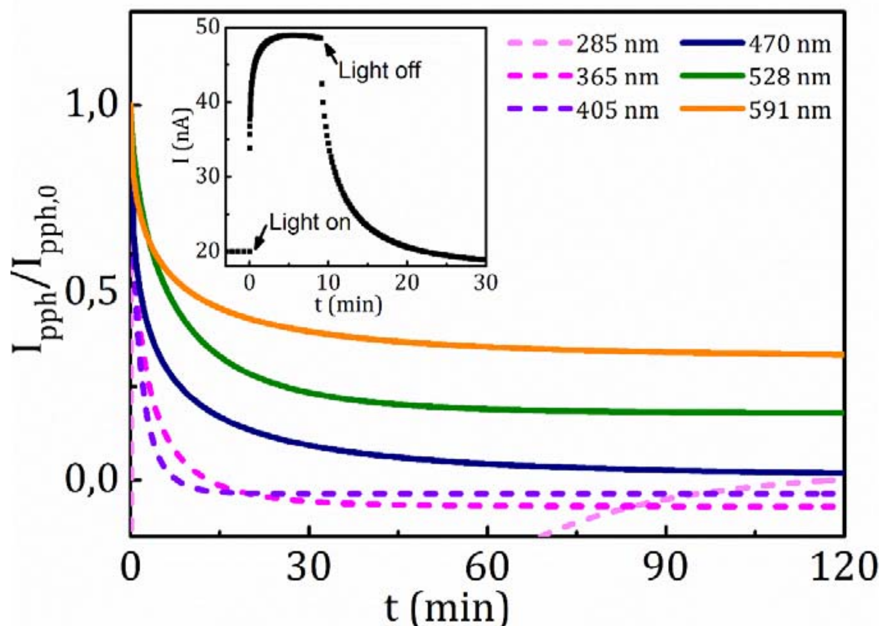


**Figure 3.4.** Persistent photocurrent decay kinetics at room temperature in a pentacene thin film after illumination at various wavelengths. Measured data are normalized to the steady-state photocurrent. Inset: typical evolution of photocurrent growth under continuous irradiation and following dark recovery.

Furthermore, the dynamics of the current revealed during prolonged exposure to a LED emitting UV light with peak centered at 285 nm differed considerably from the behaviors described above, since conductivity dramatically decreased during light periods while recovered during dark ones (Fig. 3.5). In order to assess the dependence on optical power, two different irradiances of the light source were used during experiments: 64 $\mu W/cm^2$ (Fig. 3.5a) and 158 $\mu W/cm^2$ (Fig. 3.5b).

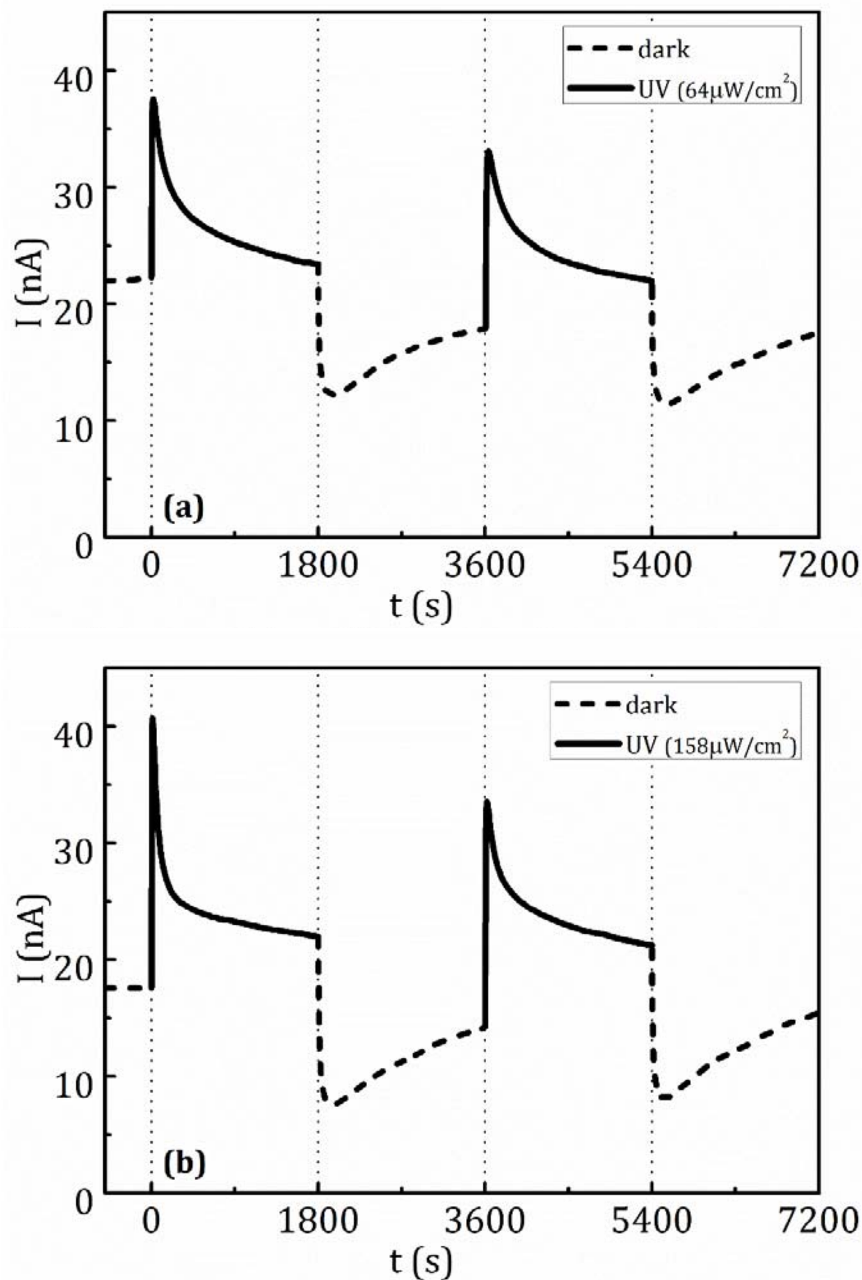


**Figure 3.5.** Current measured in a pentacene thin film at V= 30 V, during and after illumination by UV light (λ= 285 nm) with irradiances of 64 µW/cm$^2$ (a) and 158 µW/cm$^2$ (b). Photoconductivity increased not linearly with optical power.

It was found that the evolution of photoconductivity decreasing under illumination could be fully described by the sum of two exponentials with two different time constants, while just one time constant was measurable during the recovery of dark conductivity after illumination.

## 3.2 Light effects from infrared to near-ultraviolet

In order to investigate the energy level distribution, quantum efficiency spectrum from the steady-state photocurrents was measured for excitation energies ranging from 1.42 eV to 4.35 eV (Fig. 3.6) and was found to reflect the presence of peaks in pentacene absorption spectra illustrated in literature, although a general agreement on their nature and information concerning the exact energy gap of pentacene were not reported [4,16-18]. In the long wavelength region of the spectrum, the photocurrent decreased exponentially with a characteristic Urbach energy of 100 meV. This behavior near the absorption edge could result from the impurities in the organic material, in particular it could be attributed to the microfields induced by the diffused gold particles at the contact interfaces [19]. The fabricated pentacene samples exhibited a forbidden bandgap lying between 2.1 and 2.2 eV, since the peaks at 1.97 eV and 2.09 eV should be interpreted as a singlet exciton band and a dominating charge transfer exciton band, respectively, whereas the high response at 2.6 eV should represent the optical transition to an higher-lying unoccupied molecular orbital level.

By applying a continuous illumination, it was possible to evaluate the device stability. In this case, different behaviors were observed depending on radiation wavelength (Fig. 3.3). Exposure to ultraviolet light for prolonged time, with the exception of an optical energy range around 3.4 eV, turned out to be detrimental to device performances, because, after an initial period of conductivity increase due to the photo-generation of mobile charge carriers, a reduction of the total current was detected. Otherwise, in the case of infrared and visible light, no photo-degradation was observed and a continuous illumination caused a monotonic growth of current toward a constant value, which appeared

to occur either rapidly or through a gradual increment with a long constant time.

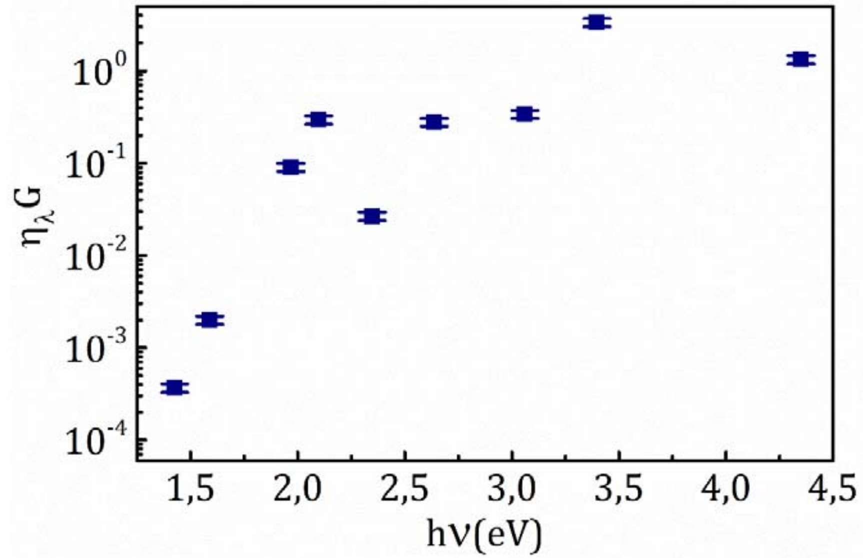


**Figure 3.6.** Quantum efficiency spectra of a pentacene thin film at room temperature.

The observation of photocurrent growth proved that the small instantaneous photoconductivity, displayed also at wavelengths where pentacene has good absorption, could be attributed to the trap limited drift mobility of the organic semiconductor. Moreover, photocurrent response and current decay showed a significant broadening, suggesting that the event time distribution extended into the time range of the experimental observation. Gaussian statistics, whose distribution function has an exponential time dependence, $\psi(t) \sim \exp(-t/\tau)$, associated with a single event time τ, could not be applied. In a disordered material, both trap modulation of the mobility and hopping between trap sites can lead to dispersion [20] in the transient photoconductivity, so that complicated time and temperature dependences should be taken into account to analyze the experimental data. A common origin for the dispersion is an exponential energy distribution of traps, $\exp(-E/kT_0)$, where $kT_0$ is the width of the trap distribution. In the case of multiple trapping transport, it has been shown that the distribution function, which describes the probability for

an event to happen at time $t$ after the previous event, obeys to a power law [20] of the form:

$$\psi(t) \sim t^{-(1+\alpha)}, \tag{3.3}$$

where the dispersion parameter assumes a value between zero and unity and is given by $\alpha = T/T_0$.

The dispersive transport model has been used to derive an expression for the growth of photocurrent during continuous uniform bulk excitation [22]. Thus, the experimental data reported in Fig. 3.3 were analyzed through the following expressions:

$$I(t) \propto t^{\alpha}\left[1-\frac{1}{3}\left(\frac{t}{\tau_g}\right)^{\alpha}\right] \quad t < \tau_g \tag{3.4a}$$

$$I(t) \propto \tau_g^{\alpha}\left[1-\frac{1}{3}\left(\frac{\tau_g}{t}\right)^{\alpha}\right] \quad t > \tau_g \tag{3.4b}$$

where $t$ is the time relative to the starting of radiation source, $\tau_g$ is a characteristic time, closely related to the time required for the carriers to move between the electrodes.

The growth of photocurrent for $t << \tau_g$ and the saturation photocurrent for $t >> \tau_g$ could be approximately rewritten as $I(t) \propto t^{\alpha}$ and $I(t) \propto \tau_g^{\alpha}$, respectively, as it was confirmed by the fitting of experimental data with straight lines in a log-log plot (Fig. 3.7). From the dependence of photocurrent $I_{ph}$ on illumination time, the characteristic parameters, $\tau_g$ and $\alpha$, were extracted for different excitation energies and illustrated in Fig. 3.9.

After illumination removal, the decay of the residual photocurrent appeared not to be exponential, but at least two regions were distinguished: an initial fast process and a following long-term relaxation, and the rate of photocurrent decrease still changed with the photon energy (Fig. 3.4). Also the origin of persistent photocurrent could be explained by the dispersive transport, since the photoexcited carriers were trapped and spatially separated by local potential fluctuations, which therefore suppressed the recombination of carriers.

A sum of exponentials with up to three components and a hyperbolic law were attempted in order to fit the experimental data of Fig. 3.4, but neither was able to provide an accurate fit over the entire range of time.

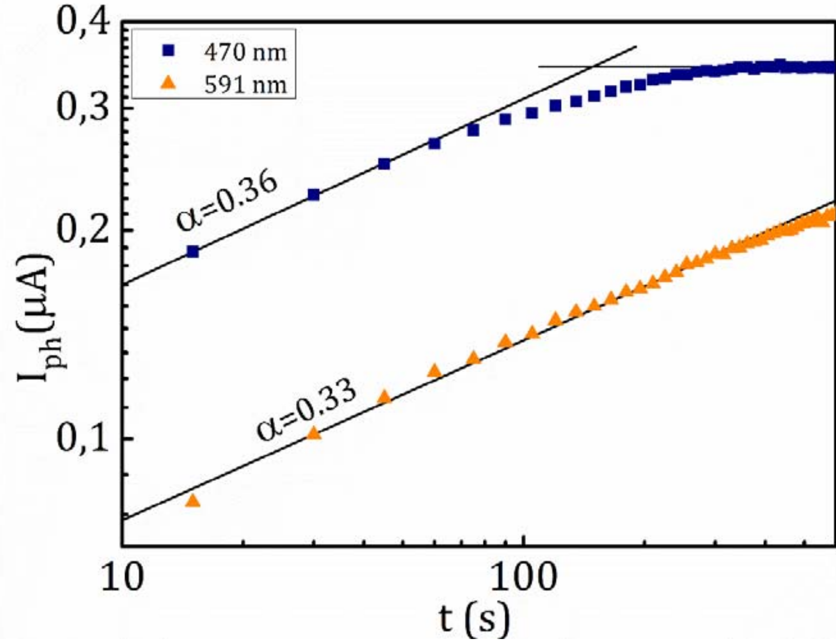


**Figure 3.7**. Log-log plot of $I_{ph}$ vs t. The curves at 470 nm and 591 nm are reported as examples of two different rise time constants ( $\tau_g^{470nm} < \tau_g^{591nm}$ ). The solid lines are the least-squares fits of experimental data proving that the photocurrent growth could be well described by a power function.

The kinetics after the termination of light were instead well described through a stretched-exponential function:

$$I_{pph}(t) = I_S + I_p \exp\left[-\left(\frac{t}{\tau_d}\right)^{\beta}\right], \qquad (3.5)$$

where $t$ is the time relative to the beginning of the relaxation experiment, $\tau_d$ is the characteristic decay time constant, $\beta$ is the decay exponent, $I_S$ is the steady-state dark current after illumination, $I_p$ is the constant which should be added to $I_S$ to equal the steady-state photocurrent. The stretching exponent ($0<\beta<1$) indicates the degree of disorder and should coincide with the dispersion parameter $\alpha = T/T_0$.

By plotting the residual photocurrent $I_{pph}(t)$ in the form $ln\left[I_p/\left(I_{pph}(t)-I_S\right)\right]$ in a log-log graph (Fig. 3.8), where $I_S$ was approximated with the value measured after 2 hours in dark conditions, the least-square fit to the experimental data yielded a linear behavior, demonstrating that the persistent photocurrent of pentacene samples followed a stretched-exponential evolution. The characteristic parameters, $\tau_d$ and $\beta$, extracted at different excitation energies were displayed in Fig. 3.9.

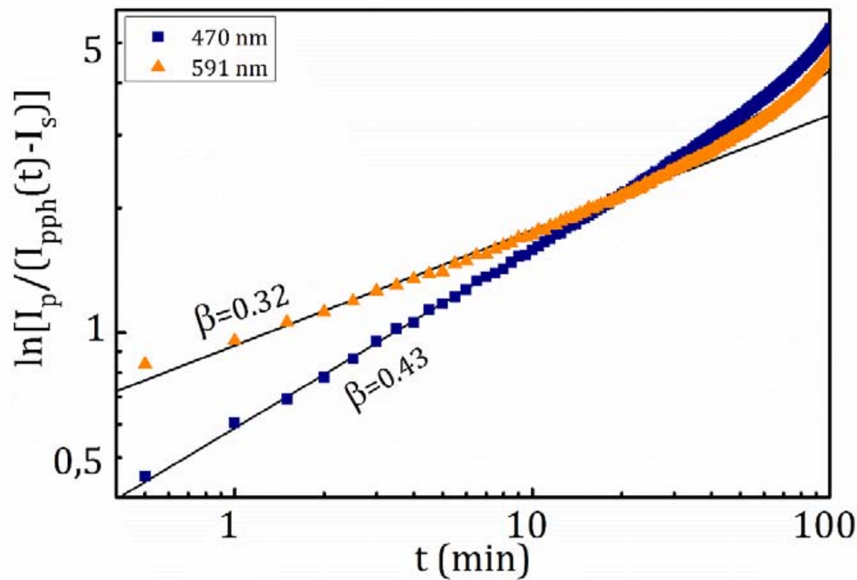


**Figure 3.8.** Log-log plot of $\ln\left[I_p/\left(I_{pph}(t)-I_S\right)\right]$ vs t. The curves at 470 nm and 591 nm are reported as examples of two different decay time constants ($\tau_g^{470nm} < \tau_g^{591nm}$) and dispersion factors ($\beta^{470nm} > \beta^{591nm}$). The solid lines are the least-squares fits of experimental data proving that the persistent photocurrent decay could be well described by a stretched-exponential function.

The time constant, characterizing the photocurrent growth and relaxation, was influenced by trapping and emission dynamics and, thus, gave information about the depth of states responsible for the observed behaviors. Indeed, it is given by $\tau = \nu^{-1}\exp\left(E_a/kT\right)$, where $\nu$ is an experimentally determined attempt-to-escape frequency and $E_a$ is the activation energy. The deeper the trap is, the longer the time

needed for thermal emission of localized carriers becomes. The rise and decay time constants were found not to match, but they followed a similar behavior: they were of the order of $10^3$ s and exhibited resonances around 1.42 and 2.09 eV, meaning that the capture and emission from these levels were very slow.

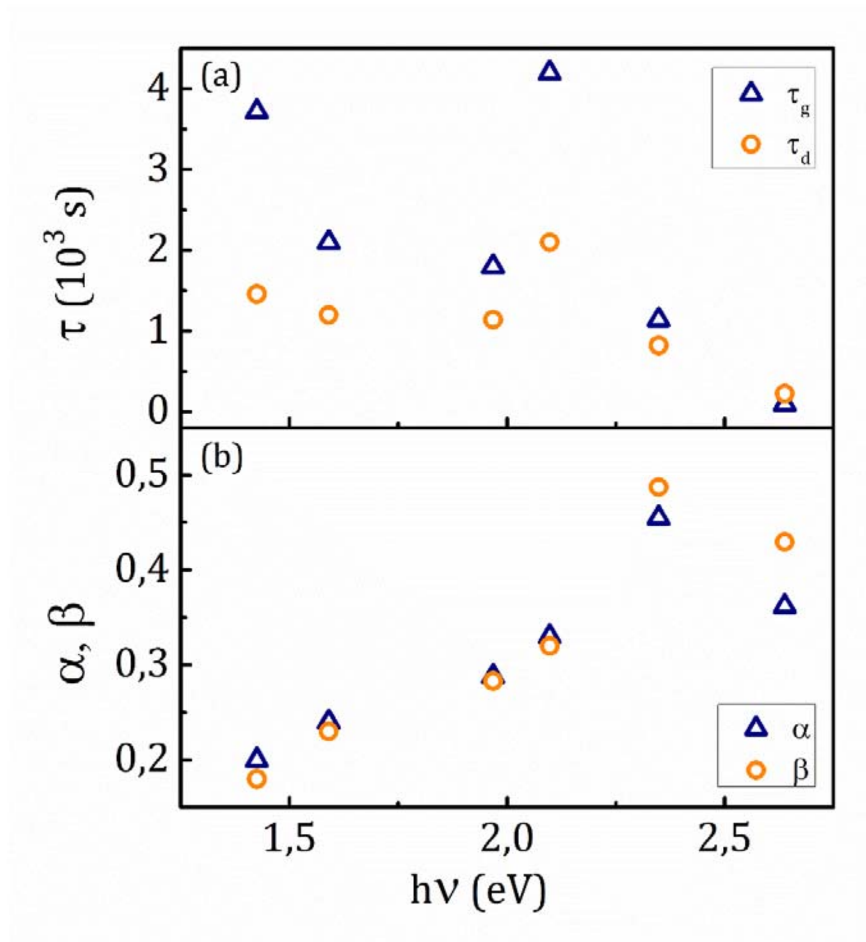


**Figure 3.9.** Characteristic time constants (a) and dispersion parameters (b) describing photocurrent growth and persistent photocurrent decay as a function of incident light energy in the infrared and visible range.

The dispersion parameters $\alpha$ and $\beta$, which were deduced from the time dependence of the photocurrent under continuous illumination with monochromatic light and during relaxation process, respectively, indicated the slope of trap distributions (inversely proportional to the

characteristic temperature $T_0$). The lower the dispersion parameter appears, the larger the distribution is. Broad distribution of deep defect states were detected within the bandgap and the quantum efficiency measured at these excitation energies reflected the energy dispersion in Fig. 3.6. Excitation of carriers from these deep levels represented the main contribution to the persistent photocurrent and, even when the quantum efficiency was not high, they influenced the transport properties since the thermodynamic equilibrium was recovered in a longer time scale.

## 3.3 Deep UV light induced metastable defects

Anomalous transient photoresponse to UV light was detected in the pentacene thin film and was explained by a study on the time evolution of generation and annealing of photoinduced bulk defects. For this aim, the dispersive defect structure of the organic semiconductor was simplified by the proposed model, which used just two components as a first-order approximation [23].

In an organic polycrystalline semiconductor charge transport takes place through the extended electronic states in the periodic structure of the crystals but is limited by the electronic states localized at the crystal grain boundaries. The structural disorder in the organic film leads to trapping of the induced charges, with the charge transport alternating between trapped and free states. By considering the capture and release dynamics of free carriers at trapping sites, mainly concentrated in grain boundaries, the formula of apparent mobility [24] could be used:

$$\mu_{eff} = \mu_0 \frac{Q_{free}}{Q_{free} + Q_{trapped}}, \tag{3.6}$$

where $\mu_0$ is the mobility of the carrier when it is in an extended state of the organic crystals, while $Q_{free}$ and $Q_{trapped}$ are the free and trapped fractions of the charge carriers.

Current measurements were developed while the organic thin film was illuminated by UV light at the optical energy of 4.35 eV. The curves shown in Fig. 3.5 represented the results of the sequence of two one-hour periods during which light and dark conditions were

alternated. The current flowing through the pentacene resistor of length $L$, width $W$ and thickness $t$, when an external bias $V$ was applied, was assumed proportional to the conductance $\sigma$ of the organic film as $I = (Wt/L)\sigma V$, since contacts contribution to the overall resistance turned out to be negligible. The conductance was given by the product of effective mobility and total charge density, which for Eq. (3.6) was equivalent to the product of band mobility and free charge density, obtained by subtracting trapped charge from total charge. Let $n_{tot}$ be the total carrier density in the semiconductor in dark conditions and $N_D$ the defect density. Under light conditions a photo-induced charge $n_{ph}$ had to be added to the carrier concentration:

$$\sigma_L = q\mu_{eff,L}\left(n_{tot} + n_{ph}\right) = q\mu_0\left(n_{tot} + n_{ph} - N_D\right), \tag{3.7}$$

where $\sigma_L$ and $\mu_{eff,L}$ are the conductivity and the effective mobility, respectively, under irradiation.

The behavior of current in the pentacene thin film under UV light exposure was related to the modification of trap state density $N_D$, due either to charge generation itself or to non-radiative recombination of energetic excitons. Photoinduced defects played an electronically active role that affected the electrical properties of the semiconductor and due to their metastable nature they persisted long enough to be observable. Referring to a double-well model [25], it was possible to define a ground state and a metastable defect state. Transitions between the two configurations, occurring over the barrier in both directions, were represented by specific generation and annealing rates. Each transition can in general be caused by thermal energy or recombination energy and, therefore, in both generation and annealing rates, a thermal activation contribution and a recombination-induced transition coefficient might be present. Exciton non radiative recombination was supposed to be the dominant process, which might cause the break of bonds in pentacene molecules thanks to high energy charges induced by ultraviolet irradiation, whereas, due to the large barrier height, thermal transitions were negligible at room temperature.

The creation and annealing kinetics of light induced metastable defects were described by the proposed model, where only two types of defects were taken into account. Each type of defects had different characteristics and followed an individual rate equation. Furthermore, it was assumed that all components arose from a unique common reservoir of ground states available for defect formation and there was

no direct communication between the two types, as proposed in [26] for hydrogenated amorphous silicon.

Thus the defect creation rate was supposed to be proportional to the density of centers that were in their ground state through a generation coefficient. Meanwhile a negative term, proportional to the defect density through an annealing coefficient, took in account the process reversibility. The system of rate equations for both components, $N_{D1}$ and $N_{D2}$, during UV light exposure was written as:

$$\begin{cases} \dfrac{dN_{D1}}{dt} = G_1\left(N - N_{D1}(t) - N_{D2}(t)\right) - A_1 N_{D1}(t) \\ \\ \dfrac{dN_{D2}}{dt} = G_2\left(N - N_{D1}(t) - N_{D2}(t)\right) - A_2 N_{D2}(t) \end{cases} \tag{3.8}$$

where $t$ is the time and $N$ is the total number of states that could be converted into defects. $G_i$ and $A_i$ with $i$=1,2 are the constant defect generation and annealing coefficients for the $i$-th component, respectively, and both include the dependence on defect cross sections and light intensity.

It was assumed that $N_D$ represented the photoinduced trap density rather than the total trap density, so that $n_{tot}$ in Eq. (3.7) included the defect concentration present in the material prior to UV-light exposure. The time evolution of each type of defects predicted by equations was the sum of two exponentials:

$$N_{Di}(t) = \alpha_i e^{-\lambda_1 t} + \beta_i e^{-\lambda_2 t} + N_i^o \quad i = 1,2 \;, \tag{3.9}$$

where the exponential constants $\lambda_1$ and $\lambda_2$ depend on generation and annealing coefficients:

$$\begin{aligned} \lambda_{1,2} = & \frac{1}{2}\left(A_1 + A_2 + G_1 + G_2\right) \pm \frac{1}{2}(A_1 - A_2 + \\ & + G_1 - G_2)\sqrt{1 + \frac{4G_1G_2}{\left(A_1 - A_2 + G_1 - G_2\right)^2}} \end{aligned} . \tag{3.10}$$

Assuming that $N_{D1}$ represented defects which were generated and annealed much faster than $N_{D2}$, i.e. $G_1 \gg G_2$ and $A_1 \gg A_2$, two independent time constants $\tau_1$ and $\tau_2$ could be defined as follows:

$$\lambda_1 \approx A_1 + G_1 = 1/\tau_1, \ \ \lambda_2 \approx A_2 + G_2 = 1/\tau_2 . \tag{3.11}$$

Analytically solving the equation system it was evident that the total defect density was mainly controlled by the fast defects in the short time limit and then by the slow defects:

$$\begin{cases} N_{D1}(t) = \tau_1 \dfrac{NG_1\tau_2 - N_1^o}{\tau_1 - \tau_2} e^{-t/\tau_1} + \tau_2 \dfrac{NG_1\tau_1 - N_1^o}{\tau_2 - \tau_1} e^{-\frac{t}{\tau_2}} + N_1^o \\ N_{D2}(t) = N_2^o \left(1 - e^{-\frac{t}{\tau_2}}\right) \end{cases} , \tag{3.12}$$

where $N_1^o$ and $N_2^o$ defined the steady-state solution and were related to $N$ so that:

$$\frac{A_1 + G_1}{G_1} N_1^o + N_2^o = N . \tag{3.13}$$

Equivalent rate equations were defined for the post-irradiation dark, where generation and annealing coefficients were supposed to be comparable for both sets of defects:

$$\begin{cases} \dfrac{dN_{D1}}{dt} = G_D\left(N - N_{D1}(t) - N_{D2}(t)\right) - A_D N_{D1}(t) \\ \dfrac{dN_{D2}}{dt} = G_D\left(N - N_{D1}(t) - N_{D2}(t)\right) - A_D N_{D2}(t) \end{cases} , \tag{3.14}$$

leading to symmetric solutions depicted in Eq. (3.15), where $N_1^i$ and $N_2^i$ were the densities of fast and slow defects, respectively, in the semiconductor when the light was switched off:

$$\begin{cases} N_{D1}(t) = \left( \dfrac{N_1^i + N_2^i}{2} - \dfrac{G_D N}{A_D + 2G_D} \right) exp\left[ -\left( A_D + 2G_D \right) t \right] \\ \qquad + \left( \dfrac{N_1^i - N_2^i}{2} \right) exp\left( -A_D t \right) + N_1^o \\ N_{D2}(t) = \left( \dfrac{N_1^i + N_2^i}{2} - \dfrac{G_D N}{A_D + 2G_D} \right) exp\left[ -\left( A_D + 2G_D \right) t \right] \\ \qquad - \left( \dfrac{N_1^i - N_2^i}{2} \right) exp\left( -A_D t \right) + N_2^o \end{cases} . \quad (3.15)$$

It was evident that the sum of the two components had a transient behavior fully described by a single time constant as follows:

$$N_D(t) = \left( N_1^i + N_2^i - \frac{2G_D N}{A_D + 2G_D} \right) e^{-\frac{t}{\tau_D}} + \frac{2G_D N}{A_D + 2G_D} . \quad (3.16)$$

This model was applied to the current measures shown in Fig. 3.5 and, by assuming $\mu_0$= 1.2 cm$^2$/Vs [27,28], it yielded the dynamics of the partial densities $N_{D1}$ and $N_{D2}$ and the total density $N_{D1}$+$N_{D2}$. The curves were plotted in Fig. 3.10 for irradiances of 64 μW/cm$^2$ and 158 μW/cm$^2$. Both sets of defects increased at the beginning of the optical degradation but, as the ultraviolet irradiation persisted, the fast defect density reached a maximum and then relaxed back again, meanwhile slow defects always showed an increase in density along exposure time. Evolutions in the post irradiation dark were similar and characterized by the same time constant. From the steady-state condition reached in the presence of light, the total density of possible defect centers was estimated to be $7{\cdot}10^{13}$ cm$^{-3}$. From the dark current the free carrier density $n_{tot}$ in pentacene samples was determined to be around $6{\cdot}10^{13}$ cm$^{-3}$, which was comparable to the estimated total center concentration available for defect creation. Finally, from analysis of photocurrents, the photo-induced charge densities were obtained equal to $5{\cdot}10^{13}$ cm$^{-3}$ and $8{\cdot}10^{13}$ cm$^{-3}$ for the low and the high intensities of the UV light irradiation, respectively.

The extracted generation and recovery coefficients describing the defect dynamics were reported in Table 1.

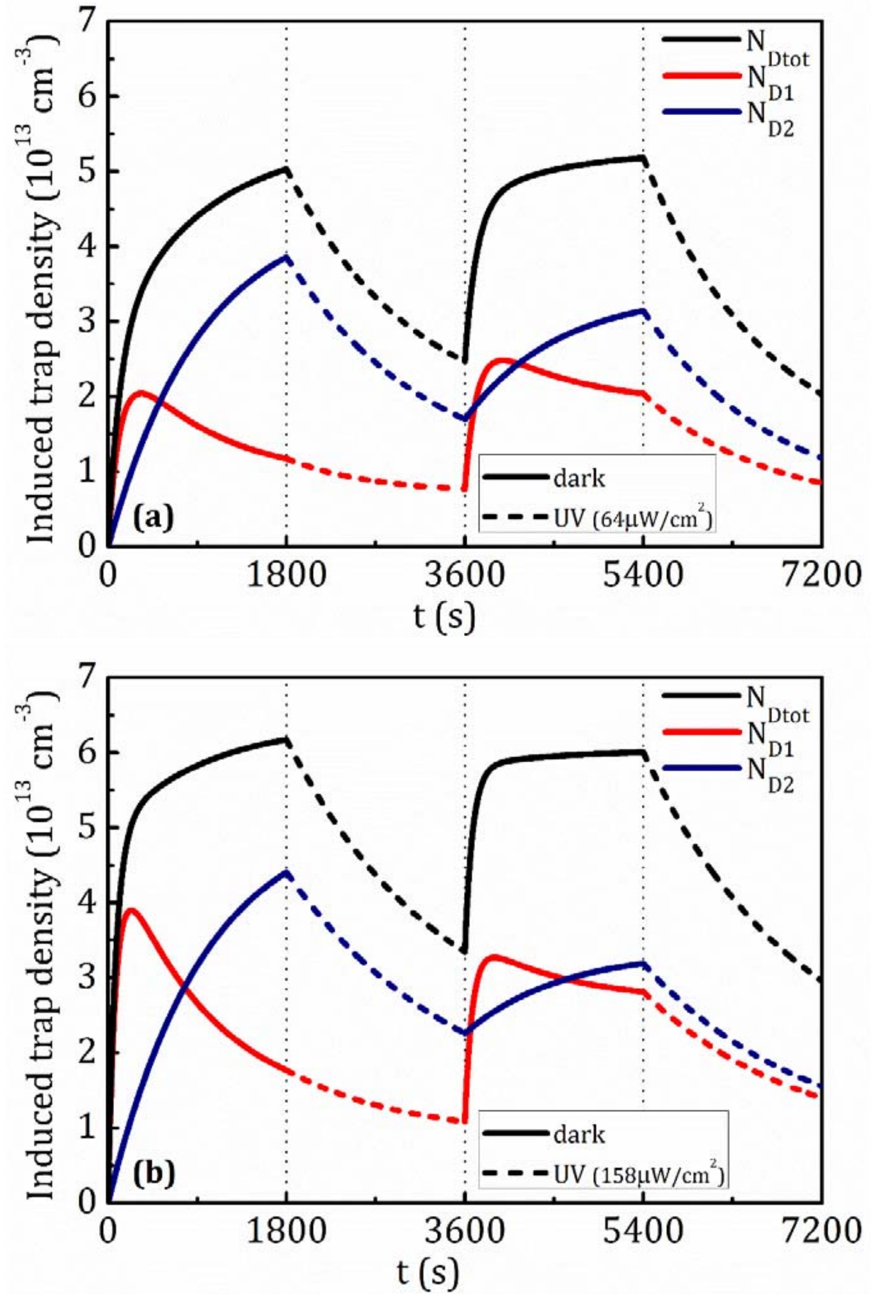


**Figure 3.10.** Plots of the total density of photoinduced defects $N_D$ and of the two components extracted from experimental data in Fig. 4 according to the proposed model, during and after illumination by UV light ($\lambda$= 285 nm) with irradiances of 64 μW/cm$^2$ (a) and 158 μW/cm$^2$ (b).

**TABLE 1.** Extracted parameters under 285 nm – light irradiation (with optical power density of 64 μW/cm$^2$ and 158 μW/cm$^2$) and during post-irradiation dark. The characteristic time constants were $\tau_1$= 119 s, $\tau_2$= 935 s and $\tau_D$= 1310 s for the low irradiance and $\tau_1$= 77 s, $\tau_2$= 962 s and $\tau_D$= 1580 s for the higher intensity.

| **Parameter** | **UV (P=64μW/cm$^2$) / Dark** | | **UV (P=158μW/cm$^2$) / Dark** | |
|---|---|---|---|---|
| | 1st period [$10^{-3}$ $s^{-1}$] (±1%) | 2nd period [$10^{-3}$ $s^{-1}$] (±1%) | 1st period [$10^{-3}$ $s^{-1}$] (±1%) | 2nd period [$10^{-3}$ $s^{-1}$] (±1%) |
| $G_1$ | 3.04 | 4.40 | 8.62 | 9.55 |
| $A_1$ | 5.36 | 4.00 | 4.37 | 3.44 |
| $G_2$ | 0.79 | 0.71 | 0.93 | 0.81 |
| $A_2$ | 0.28 | 0.36 | 0.11 | 0.23 |
| $G_D$ | 0.09 | 0.05 | 0.09 | 0.07 |
| $A_D$ | 0.59 | 0.66 | 0.45 | 0.49 |

Analysis of the parameters at different optical power densities gave consistent results: when UV intensity was higher, trap formation rates increased for both kinds of defects, proving that the generation process was driven by the interaction with light; in contrast, trap annealing rates dropped, showing that light should be able to cause recovery of defects as well as their formation.

In the absence of light, defect generation was negligible and could be ascribed to the current flow or to the energy released upon the excess carrier recombination. The photoinduced defects annealed out even at room temperature, with a long time constant due to their metastable nature.

## 3.4 Conclusion

The instability of the electronic properties of organic materials and device performance under light exposure could be a critical problem limiting their application. An experimental analysis of degradation effects of a polycrystalline pentacene thin film and a study focusing on metastable nature of defects were presented; the aim was the

understanding of the mechanisms lying behind the operation of the organic electronic devices.

The samples were illuminated with different energy photons and the steady-state photocurrents were measured, showing that the spectrum was dominated by a high efficiency under ultraviolet light, related to the molecular-like properties of pentacene, and an intense response at 2.1 eV, due to the formation of charge transfer excitons.

Also the photoconductivity evolution under continuous excitation and the following recovery in dark were investigated in order to judge the mechanisms of transport, carrier storage and relaxation. The large value of persistent photocurrent along with very long decay times suggested delay in the recombination process. Relaxation time constants, as well as dispersion factor, changed with photon energy. The existence of deep states within the bandgap, due to the disorder in the pentacene film, gave the main contribution to the persistent photocurrent.

Conductivity degradation was observed as a result of enduring exposure to a high energy UV light and was ascribed to an increase in the trapping states. Slow and fast defects were demonstrated to control the degradation and recovery kinetics of photocurrent which showed a double exponential behavior. Through the definition of apparent mobility, pentacene conductivity and photocurrent were related to the trapping site concentration. Thus a mathematical model defining the generation and annealing dynamics of photoinduced metastable defects was developed from the simplification of trap states. Two components were taken into account: each of them was related to a type of defect and was described through specific generation and annealing coefficients. Parameters extracted from the experiments under light irradiation were revealed to depend on the optical intensity, while they turned out to be constant under dark conditions.

# References


1. D. Nabok et al., Phys. Rev. B **76**, 235322 (2007)
2. M. Kitamura, and Y. Arakawa, J. Phys.: Condens. Matter **20**, 184011 (2008)
3. K.K. Ryu et al., IEEE Trans. On Electron Dev. **57**, 1003 (2010)
4. B. Fraboni, A. Matteucci, A. Cavallini, E. Orgiu, and A. Bonfiglio, Appl. Phys. Lett. **89**, 222112 (2006)
5. R. Liguori, and A. Rubino, “Metastable light induced effects in pentacene”, Organic Electronics. Submitted
6. Y.J. Lin, F.M. Yang, W.Y. Chou, and J. Chang, Jpn. J. Appl. Phys. **47**, 7851 (2008)
7. J.M. Choi, W. Choi, S. Lee, and S. Im, Synthetic Metals **158**, 1072 (2008)
8. J.M. Choi, D. K. Hwang, J.M. Hwang, J.H. Kim, and S. Im, Appl. Phys. Lett. **90**, 113515 (2007)
9. N. Wrachien et al., IEEE Trans on Nuclear Science **58**, 2911 (2011)
10. W. J. Kim, W. H. Koo, S. J. Jo, C. S. Kim, H. K. Baik, D. K. Hwang, K. Lee, J. H. Kim, and S. Im, Electrochem. Solid-State Lett. **9**, G251 (2006)
11. A. Rose, Proc. IRE **43**, 1850 (1955)
12. Y.-Y. Noh, and D.-Y. Kim, Solid-State Electr. **51**, 1052 (2007)
13. J.-M. Choi, and S. Im, Synthetic Metals **159**, 1689 (2009)
14. M. Kuik, L.J.A. Koster, G.A.H. Wetzelaer, and P.W.M. Blom, Phys. Rev. Lett. **107**, 256805 (2011)
15. J.C. Scott, S. Karg, and S.A. Carter, J. Appl. Phys. **82**, 1454 (1997)
16. J. W. Spalenka, E. M. Mannebach, D. J. Bindi, M. S. Arnold, and P. G. Evans, Appl. Phys. Lett. **99**, 193304 (2011)
17. D. V. Lang, X. Chi, T. Siegrist, A. M. Sergent, and A. P. Ramirez, Phys. Rev. Lett. **93**, 086802 (2004)
18. C. Jundt, G. Klein, B. Sipp, J. Le Moigne, M. Joucla, and A. A. Villaeys, Chem. Phys. Lett. **241**, 84 (1995).
19. M. Ohtomo, T. Shimada, K. Saiki, and T. Hasegawa, J. of Appl. Phys. **102**, 064510 (2007)
20. G. Pfister, and H. Scher, Adv. Phys. **27**, 747 (1978)
21. H. Scher, and E. W. Montroll, Phys. Rev. B **12**, 2455 (1975)
22. S. R. Kurtz, and R. C. Hughes, J. Appl. Phys. **54**, 229 (1983)
23. R. Liguori, S. Aprano, and A. Rubino, AIP Conf. Proc. **1583**, 212 (2014)

24. K. Ryu, I. Kymissis, V. Bulović, and C.G. Sodini, IEEE Electron Dev. Lett. **26**, 716 (2005)
25. R. S. Crandall, Phys. Rev. B **43**, 4057 (1991)
26. L. Yang and L. Chen, Appl. Phys. Lett. **63**, 400 (1993)
27. C. C. Mattheus et al., Synthetic Metals **138**, 475 (2003)
28. J. Y. Lee, S. Rith, and Y. W. Park, Appl. Phys. Lett. **88**, 252106 (2006)

# Chapter 4

# Interface trap states in organic thin film transistors

Organic-based electronic devices have gained immense importance in recent years in the field of cost-effective, reduced power consumption and large area production processes [1]. Electronics has adopted the advantages of organic materials in the fabrication of field effect transistors, by relying especially on conjugated polymers and small molecules. Organic technology, together with science of thin films, can help to overcome the challenges that drive modern societies, by encouraging the development of new promising applications [2-5]. However, for organic materials, the theoretical interpretation of their electronic and optical properties is still incomplete. Besides being a key device of technological interest, thin film transistors can be a tool for studying the charge transport in solid materials [6,7] and are particularly suitable for organic semiconductors, which are materials with low charge carrier mobility.

Organic TFTs were fabricated and a series of experiments were carried out to investigate their performances [8]. In particular, pentacene-based thin film transistors were studied under photoirradiation, which allowed the identification of trap states affecting charge transport. Light was used in order to generate a high density of both charge carriers and study the localized states [9]. The motivation was that in a p-type semiconductor the presence of a large enough concentration of electrons could introduce electronic behaviors which otherwise would not be visible. At the same time, it was possible to evaluate the stability of the electrical performances of the organic transistors under steady-state illumination and to assess the applicability of such devices as photodetectors.

A light environment was exploited as a tool for investigating defects in the organic material also during capacitance-voltage measurements

[10,11]. The admittance techniques could provide plenty of information about the properties of a field-effect device [12-14], particularly with respect to the semiconductor physical nature, the transport mechanism in the active layer [15-17], the insulating properties and the semiconductor-insulator interface quality [18-20].

## 4.1 Photocurrent in organic field effect transistors

This paragraph is devoted to the investigation of photocurrent in organic devices. For this purpose, OTFTs were fabricated, with pentacene as active layer and with an innovative polymer as insulator, and current measurements were performed under light conditions. The equations useful to describe the photocurrent evolution and to separately characterize the effects of photogenerated electrons and holes were proposed.

### 4.1.1 Pentacene based thin film transistors with ActivInk D0150 dielectric

Organic thin film transistors were fabricated in the top-contact bottom-gate configuration (Fig. 4.1) starting from a glass substrate. Prior to deposition processes, the substrate was cleaned in an ultrasonic bath with acetone and isopropanol and, then, blown with dry nitrogen. A transparent gate electrode of ITO (Indium-Tin-Oxide) was deposited with a thickness of 125 nm. An innovative photocurable polymer, D0150, specifically synthesized in the laboratories of Polyera Corporation, was used as gate insulator. The polymeric solution was spin-coated to afford a film thickness of about 600 nm. The film was cured under ultraviolet irradiation at 300 nm wavelength for 30 min and then baked at 120°C for 2 min. Subsequently, the thermal evaporation of a 50 nm thick pentacene active layer was conducted under the base pressure of $2 \cdot 10^{-7}$ mbar. The deposition rate of the organic molecule was maintained at 0.5 Å/s on the substrate kept at room temperature. After semiconductor film deposition, the transistors were completed by evaporating 50 nm thick layer of gold through a shadow mask to realize

source and drain electrodes. Different devices were considered; since they showed similar qualitative features, the results belonging to the most representative samples were reported.

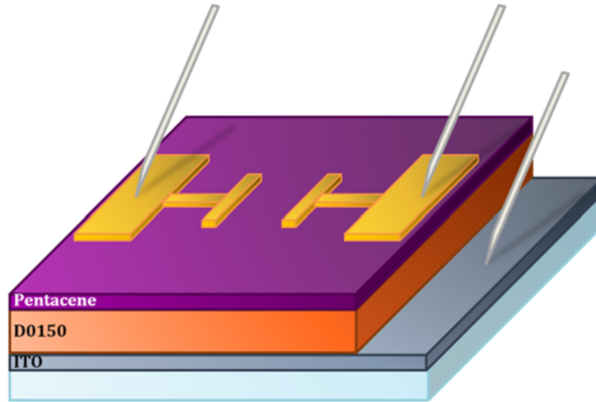


**Figure 4.1.** Structure of the OTFTs fabricated with pentacene and D0150.

Field-effect mobility could be estimated, in both linear and saturation regime, from the fundamental relationships based on the traditional silicon MOSFET model:

$$\mu_{FE}^{lin} \equiv \frac{L}{WC_i V_D} \frac{\partial I_D}{\partial V_G}, \tag{4.1a}$$

$$\mu_{FE}^{sat} \equiv \frac{2L}{WC_i} \left( \frac{\partial \sqrt{I_D}}{\partial V_G} \right)^2, \tag{4.1b}$$

where $W$ and $L$ are the width and the length of the channel, respectively, and $C_i$ is the insulator capacitance. However, for the fabricated devices, the use of such a model was found to be inadequate because of the dispersive conduction mechanism, as previously discussed, typical of polycrystalline organic semiconductor. In particular, it was not possible to obtain a perfectly linear trend from the extrapolation curves described by Eqs. (4.1a) and (4.1b), but more than one value for the mobility, as well as for the threshold voltage, could be defined depending on the selected range of data. While in an amorphous organic semiconductor the field effect mobility dependence on gate bias is related to the hopping charge transport, in polycrystalline films of

small-molecule semiconductors, where most of the defects are concentrated at the grain-boundaries, it is more reasonable to attribute this behavior to a multiple trapping and release mechanism. According to this model, charge transport occurs in a delocalized band but is limited by the intra-gap trap distributions. While majority charges are accumulated in the organic layer upon applying a negative gate bias, localized states are increasingly filled by the shift of Fermi level, thus resulting in an effective mobility dependence on bias. At a gate voltage of 30V, a field-effect mobility through the conducting channel and a threshold voltage were measured of about $3 \cdot 10^{-2}$ $cm^2/Vs$ and 10.7 V, respectively.

Both measuring method and bias application period affected measured parameters. Upon air exposure, a threshold voltage shift, which hastened the device switching, and an increase in gate leakage occurred. It was seen that by keeping the devices in vacuum for at least 12 hours it was possible to partially regain the threshold voltage. This behavior, along with the not full recovery of the original values, could be explained by the release of oxygen, which had been absorbed from atmosphere and had enhanced the conductivity, by acting as doping for pentacene. In addition, over time, the continual bias stress, as well as the inherent degradation process essentially due to moisture absorption, tended to modify permanently the transistor behavior (Fig. 4.2).

Measurements under ultraviolet irradiation altered the characteristics even more incisively, in particular the transconductance decreased and the threshold voltage shifted toward larger positive values (Fig. 4.3), so that saturation regime was no more observed within the bias range considered during the first electrical characterization. However, the exposure to an ultraviolet irradiation centered at 285 nm, a wavelength next to the one used for the dielectric curing, was revealed to reduce the loss currents through the insulator film. According to experimental results found in literature [21], molecular oxygen and water did not react irreversibly with pentacene, on the experiments time scale, as long as they came into contact in dark. Also a visible light excitation might not be sufficient to promote a reaction. Indeed, in both cases, oxygen, diffused into pentacene at atmospheric pressure, seemed to evacuate again rapidly in vacuum conditions.

In contrast, the exposure of pentacene to air in presence of UV light most probably yielded an oxidation by singlet oxygen and/or ozone produced by UV light, even if the reaction product was not yet well defined.

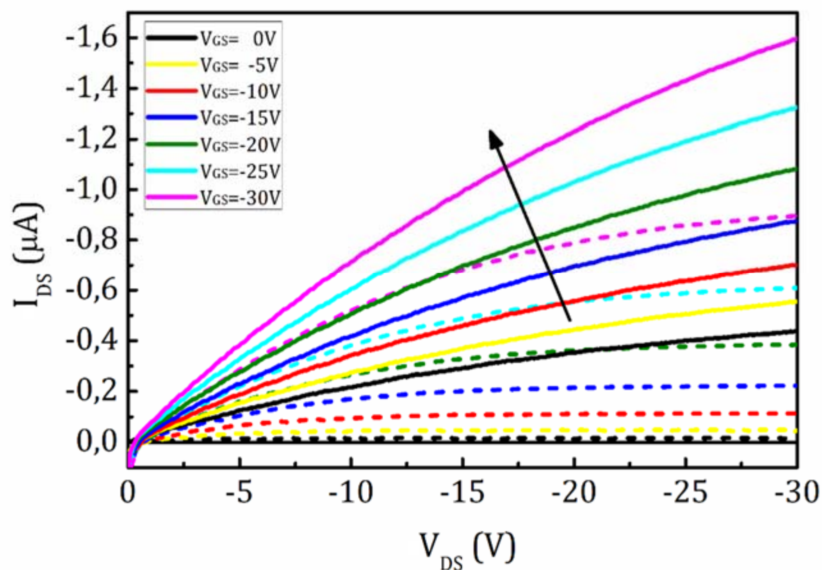


**Figure 4.2.** Output characteristics of pentacene-based OTFTs. Pristine samples (dashed lines) and after bias and optical stress (solid lines).

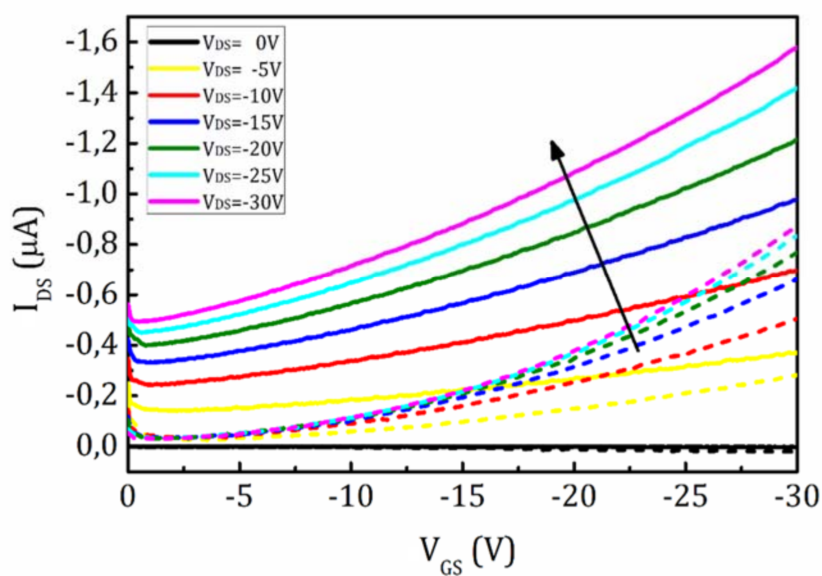


**Figure 4.3.** Transfer characteristics of pentacene-based OTFTs. Pristine samples (dashed lines) and after bias and optical stress (solid lines).

### 4.1.2 Light induced effects in pentacene thin film transistors

An investigation of the effect of the wavelength of the incident light source on the performance of the OTFTs was proposed. For this aim, the devices were illuminated from the top side, by the use of LEDs located at a distance of 5 mm from the substrate, at various irradiances and wavelengths in the visible and ultraviolet range (between 285 nm and 630 nm). All measurement were performed at room temperature and in ambient air. Thanks to the photo-generation of mobile charge carriers, an increase of conduction current was detected (Fig. 4.4). Moreover, the shape of the characteristic plots changed under illumination, as it was seen from the photoresponse, i.e. the ratio between the current under illumination and the current in the dark (inset of Fig. 4.4).

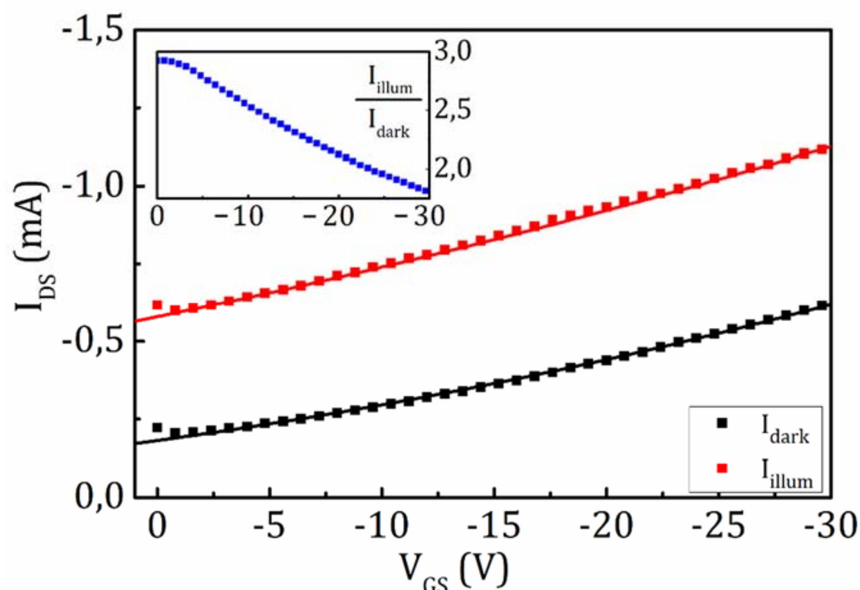


**Figure 4.4**. Drain current in the dark and under illumination ($V_{DS}$= -30 V). Inset: photoresponse of the organic transistor for negative $V_{GS}$.

In particular, a negative gate-to-source voltage should cause the conduction to be dominated by field-induced charges, while, next to the threshold voltage, light induced charges should contribute to the

measured current for the main part and the photoresponse should be greater than in accumulation regime. For this reason, illumination in a field-effect transistor could be seen as an additional element able to control the gate electrode and it could be used as an optical signal in addition to the electrical signal. In other words, the thin film transistor could be switched on through two control elements: a gate voltage or a light radiation, and when one of these sources is off the effect of the other one is maximized.

The transfer curves measured under illumination showed a shift toward more positive gate voltages with respect to the transfer characteristics in the dark. Such a behavior was similar to that induced by dark bias stress [22] and was justified by the presence of deep states in the channel region: when charge carriers are trapped, they can partially screen the gate field. Therefore, from the translation of threshold voltage, surface deep trap density could be estimated. This shift was not accomplished by a change in conductivity. Indeed, channel mobility should be only determined by the shallow traps, thus it was not affected by illumination.

However, the photocurrent, defined as the current increase under light conditions, exhibited different behaviors, depending on the radiation energy, optical power and measuring method. If the devices were irradiated with a visible light source, they showed a shift of the curves along the voltage axis, with the greatest effect at a photon energy near the absorption edge of the organic semiconductor. Moreover, the photocurrent increased with irradiance level without any change in the conductivity. On the other hand, when the transistors were illuminated by an ultraviolet light source, the threshold voltage shift was even larger, but a transconductance drop was observed with increasing power. The dependence of the relative photocurrent on the irradiance was illustrated in Fig. 4.5, at different gate-to-source voltages.

Furthermore, by inspecting the evolution of the current levels at a fixed drain-to-source voltage, during and after irradiation, it was observed that for higher negative gate biases the light source removal oddly yielded an increase in current (Fig. 4.6).

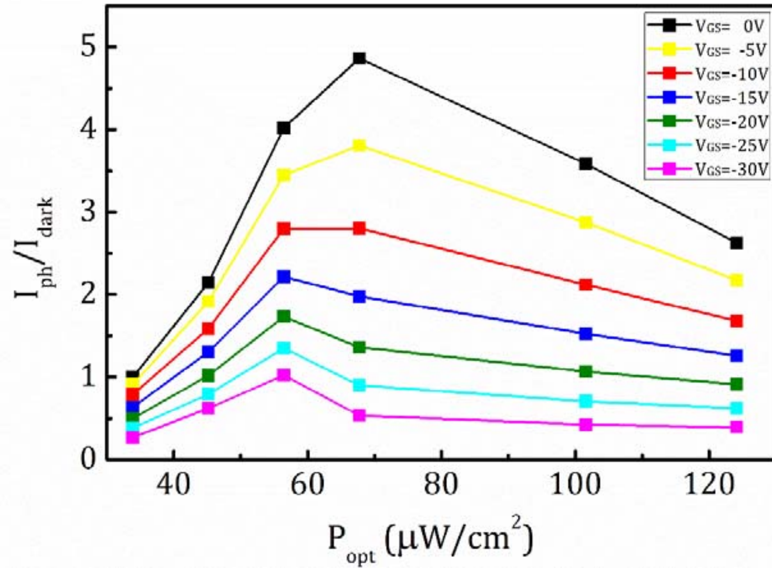


**Figure 4.5.** Dependence of the relative photocurrent ($V_{DS}$= -30 V) on the irradiance of an ultraviolet irradiation, at various $V_{GS}$.

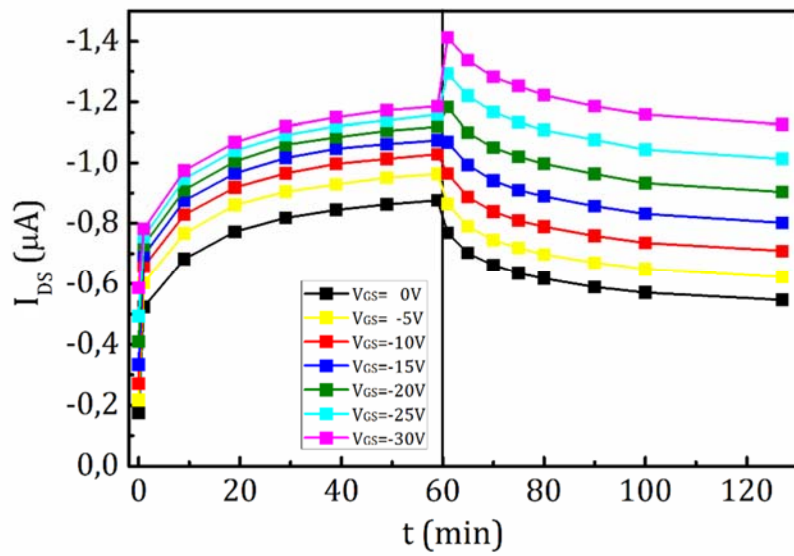


**Figure 4.6**. Evolution of drain current under irradiation and recovery in the dark ($V_{DS}$=-30 V). Light was removed at t=60 min.

The explanation was sought in a measurement self-induced effect. Indeed, if electron interface trapping under illumination was supposed to be responsible for the forward shift of threshold voltage, the holes induced at the interface during I-V measurements could neutralize the trapped charge, leading to a temporary backward shift of the threshold voltage during the measurement itself.

Such a mechanism was proved through the alteration of the ramp speed of the gate voltage: by lowering the sweep rate from 3 V/s to 0.2 V/s, the current curves under illumination tended to stretch out to such an extent that the resulting photocurrent reduced to zero (Fig. 4.7).

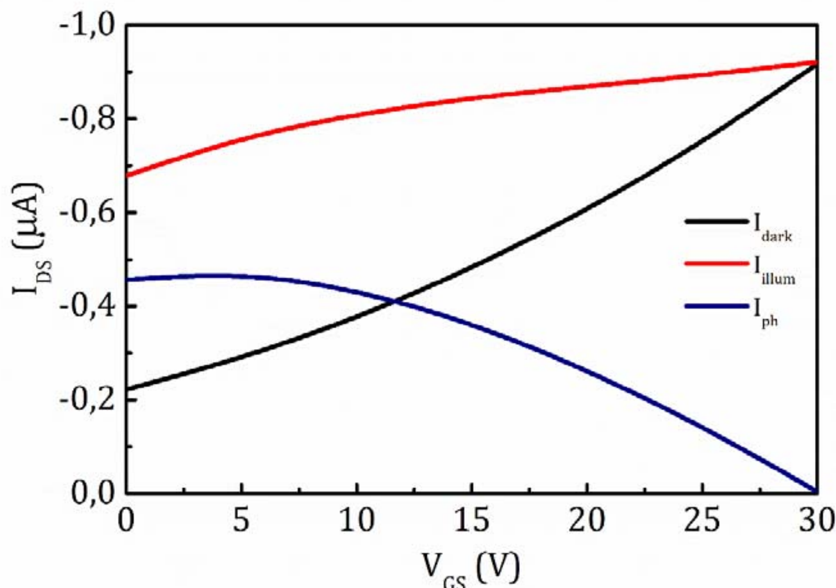


**Figure 4.7**. Transfer curves of drain current ($V_{DS}$= -30 V) in dark and under illumination with a sweep rate of 0.2 V/s. By reducing the sweep rate photocurrent could drop to zero.

The effects obtained as a result of the illumination of the devices and the simultaneous application of an electric field perpendicular to the interface gave a further confirmation to the proposed hypotheses. In particular, when illumination was applied to a device polarized with a positive gate-to-source voltage, the current increased; on the contrary, if the device was operating in accumulation region with a negative gate-to-source voltage, the current was decreased by illumination, oppositely to what was usually observed in photoconductivity

experiments. Thus, depending on the sign of the transverse electric field at the interface under illumination, either positive or negative charges could be deeply trapped at the interface or even transferred into insulator.

### 4.1.3 Photovoltaic and photoconductive effects

The photogeneration caused the increase in the drain current. Large number of excitons were generated when photons of energy equal or higher than the band-gap were absorbed. Subsequently, excitons dissociated into holes and electrons: holes could flow to the drain electrode, whereas electrons due to the lower mobility could be easily trapped in localized states.

In a field effect transistor, two mechanisms have been distinguished in the active layer to explain the photoinduced response. A photovoltaic effect has been observed when the transistor operated in the on-state; it was associated to a photovoltage induced by the accumulation of a large number of carriers under the electrodes, leading to the lowering of the potential barrier between the electrodes and the semiconductor channel. This effect could give rise to a significant increase in current, through a shift of the switch-on voltage, and its dependence on the illumination irradiance has been described by a logarithmic relationship [23]:

$$I_{ph,\mathrm{on}} \sim ln\left(1+\eta_{\lambda}\frac{qP_{opt}}{h\nu I_{d}}\right), \tag{4.2}$$

where $\eta_{\lambda}$ is the external quantum efficiency, $I_d$ is the dark current, $h$ is the Planck constant, $P_{opt}$ is the incident optical power, or by a power law function [24]:

$$I_{ph,\mathrm{on}} \sim P_{opt}^{\gamma}, \tag{4.3}$$

where $\gamma$ is a gate bias and material dependent factor.

On the other hand, a photoconductive effect has been seen when the device operated in the off-state. It arose from the photogeneration of mobile carriers, whose number increased with the photon flux, so that the photocurrent exhibited a direct dependence on the illumination power through the following relation:

$$I_{ph,\mathrm{off}} = \eta_\lambda G \frac{qP_{opt}}{h\nu}, \tag{4.4}$$

where $\eta_\lambda$ is the quantum efficiency, $G$ is the photoconductivity gain, $\nu$ is the irradiation frequency.

Starting from these observations, the total photocurrent $I_{ph}$ measured in the pentacene TFTs was assumed to result from the sum of a contribution caused by the threshold shift, $I_{ph,\Delta VT}$, and a direct photo-induced current, $I_{ph,direct}$, so that the total current measured under illumination, $I_{illum}$, was:

$$I_{illum} = I_d + I_{ph} = I_d + I_{ph,\Delta V_T} + I_{ph,direct}, \tag{4.5}$$

where $I_d$ is the dark current. $I_{ph,\Delta VT}$ and $I_{ph,direct}$ were introduced to take into account the effects of the photogenerated electrons and the photogenerated holes, respectively, on the drain current. In particular, it was assumed that, under illumination, excitons were generated uniformly in the bulk of the organic material of the transistor and then split into free charge carriers. The photogenerated holes gave contribution to a direct photocurrent through the drain, while the photogenerated electrons were trapped in localized states, most likely present at the interface between the pentacene and the insulating layer. When electrons were trapped, they screened the voltage applied at the gate electrode, leading to a translation of the voltage needed to turn on the device. The observed shift occurred toward more positive voltages, promoting the device switching and increasing the overall channel current.

The effect of irradiation was investigated when the transistors were biased in the linear region, in order to obtain a uniform charge carrier density in the channel. However, the transfer curve did not show a linear behavior, because of the increase of the field-effect mobility with the gate voltage value relative to the threshold voltage. Indeed, in the polycrystalline pentacene, a multiple trapping and release mechanism for the majority carriers occurred and the field-effect mobility, $\mu_{FET}$, could be expressed through the following expression [25]:

$$\mu_{FET} = \mu_0 \left(V_{GS} - V_T\right)^{\gamma}, \tag{4.6}$$

where $\mu_0$ is a constant, $V_{GS}$ is the gate-to-source voltage, $V_T$ is the threshold voltage. The exponent $\gamma = 2(T_0/T - 1)$ is a semi-empirical parameter, dependent on the temperature $T$ and associated to the width, $kT_0$, of a band tail distribution. According to this expression, the dark current, $I_d$, had a superlinear dependence on the transverse field and was written as:

$$I_d = K\left(V_{GS} - V_T\right)^{\gamma+1} V_{DS} \ , \tag{4.7}$$

with $K = \mu_0 C_i W/L$. $C_i$ is the insulator capacitance, $W$ and $L$ are the width and the length of the channel, respectively, and $V_{DS}$ is the drain-to-source voltage. The exponent γ, obtained from the fitting of the current plot in the dark, was 1.2, equivalent to a band tail width of about 40 meV.

The drain current in the linear regime under illumination was presented through two components:

$$I_{illum} = K_L\left(V_{GS} - V_{TL}\right)^{\gamma+1} V_{DS} + G_L\left(V_{GS} - V_{TL}\right)^{\gamma} V_{DS} \,. \tag{4.8}$$

The first term, where $K_L$ and $V_{TL}$ are the equivalent prefactor and threshold voltage under light conditions, resembled the form of the dark current and corresponded to the sum of $I_d$ and $I_{ph,\Delta VT}$ in Eq. (4.5). The second term, where $G_L$ is a constant correlated to the pentacene layer conductance under illumination, represented the direct photocurrent $I_{ph,direct}$. Also in the latter contribution the mobility dependence on the transverse electric field was included, by using Eq. (4.6) with the equivalent threshold voltage under illumination.

The threshold voltage shift resulted from the trapping of photogenerated electrons, while the excess mobile holes supplied a direct photocurrent through the drain, proportionally to the incident light intensity. Indeed, the constant $G_L$ could be written as:

$$G_L = \frac{q\mu_0 n_{ph}}{L^2} = \frac{q\mu_0 \tau}{L^2}\eta_\lambda \frac{P_{opt}}{h\nu} \,, \tag{4.9}$$

where $n_{ph}$ are the photogenerated charge carriers in the semiconductor layer, $\eta_\lambda$ is the quantum efficiency, $\tau$ is the excess carrier lifetime.

The experimental data (Fig. 4.8) were fitted to the proposed equations. Parameters $K_L$, $V_{TL}$ and $G_L$ were extracted and their evolution with illumination time were studied, in order to investigate separately the light effects on the pentacene structure, the trapping of excess electrons and the photoconductive efficiency, respectively. The dependences of each component on exposure time and recovery kinetics were recorded for different photon energies. The most representative results were shown in Fig. 4.9 for a visible light radiation and in Fig. 10 for a UV light.

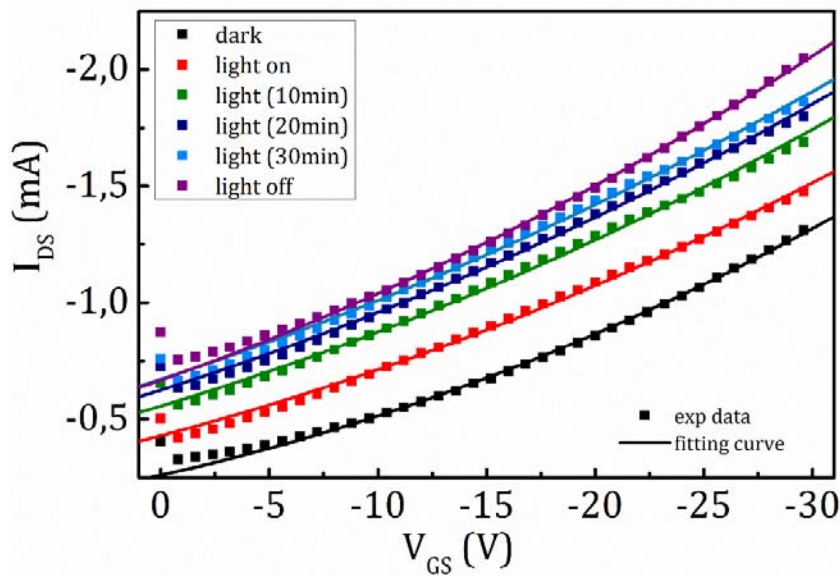


**Figure 4.8.** Typical transfer characteristics of the OTFT ($V_{DS}$= -30 V) in dark, at different illumination times and after irradiation. Experimental data were fitted with the proposed model (Eq. 8).

Regarding the effects of an irradiation in the visible range (Fig. 4.9), during illumination, it was observed a gradual shift of the threshold voltage, suggesting that an even larger number of photogenerated carriers were being trapped at the interfaces, while the mobility factor, $\mu_0$, remained practically constant, indicating that the electronic structure of the organic semiconductor was not affected by the illumination. The response of photogenerated holes, as seen in the evolution of the photoconductance factor $G_L$, was limited by the dispersive transport in the organic material.

The curves of the threshold voltage shift could be well fitted with a power law:

$$\Delta V_T \sim t^{\alpha}, \tag{4.10}$$

where $\alpha$ depended on the gate bias. In particular, the translation in $V_T$ showed to be slower for high negative $V_{GS}$. The reason could be the repulsion of photogenerated electrons from the interface where they were trapped and the enhanced hole recombination. In order to verify this phenomenon, a persistent constant bias was applied to the gate of devices under illumination. It was observed that a negative voltage, applied for a prolonged time, reduced the initial translation induced by illumination to such an extent that the threshold voltage moved to the opposite direction, that is toward more negative values. On the contrary, high positive gate bias, persisting during illumination, seemed to accelerate the shift of the threshold voltage.

The illumination effectively shifted the threshold voltage of the device, while the field-effect mobility of the charge carriers in the channel remained unchanged. Such a feature indicated the usefulness of the illumination in controlling, similarly to a gate-source voltage, the density of charge carriers in the device; in other words, the transistor could be switched on by applying either a negative gate voltage or a pulse of illumination.

From the recovery of current after irradiation, it was seen that, while the direct photocurrent disappeared within a few tens of seconds, the current remained at an elevated level due to the photovoltaic effect. The trapped electrons, responsible for this behavior, relaxed back with a time constant which could reach the tens of minutes. This property, i.e. the ability of storing the information about illumination power and duration for an extended amount of time, suggests the use of these transistors as a memory device. A full recovery of the devices after illumination was not always observed, while in the meantime a decrease in the mobility could occur due to the intrinsic degradation (Fig. 4.9). On the contrary, an illumination by an ultraviolet source induced a modification in the structure of the organic semiconductor. This mechanism was evident from the reduction of the mobility, over the whole irradiation period especially for a wavelength of 285 nm (Fig. 4.10), and it was related to the creation of electrically active defects.

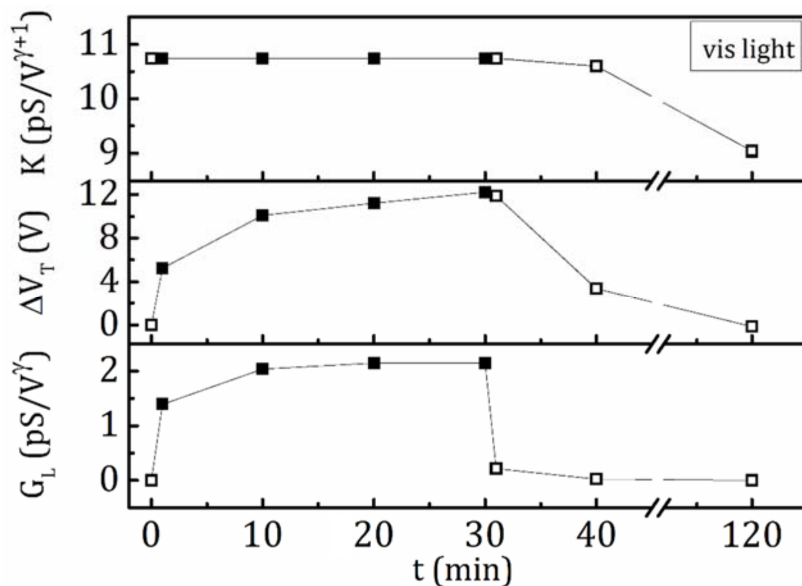


**Figure 4.9.** Evolutions of mobility factor ($K$), threshold voltage shift ($\Delta V_T$) and photoconductance factor ($G_L$) in dark (□), during visible light (591 nm) irradiation (■) and after irradiation (□).

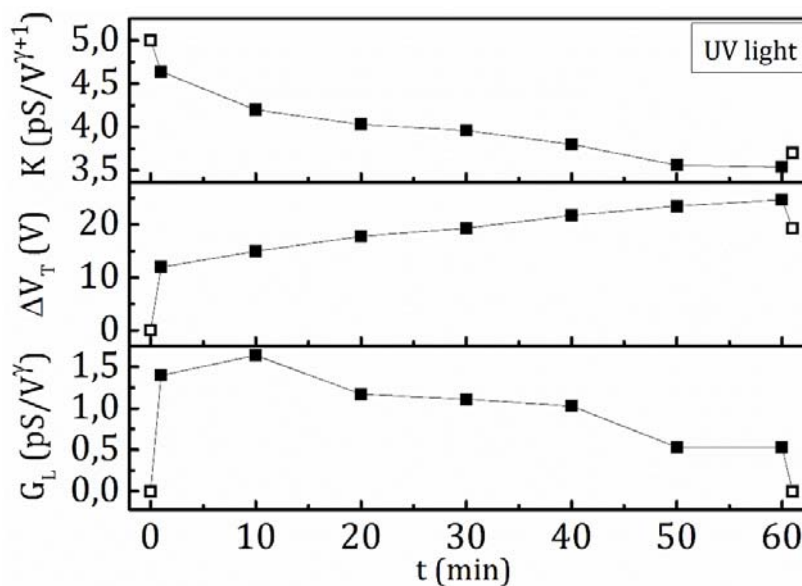


**Figure 4.10.** Evolutions of mobility factor ($K$), threshold voltage shift ($\Delta V_T$) and photoconductance factor ($G_L$) in dark (□), during ultraviolet light (285 nm) irradiation (■) and after irradiation (□).

Indeed, upon the increase of photoinduced traps, the threshold voltage shift was not seen to reach an equilibrium value but tended to a continuous growth as long as the light was on. Simultaneously, a decrease in photoconductance more rapid than the mobility degradation was observed, likely due to the enhancement of the hole trapping and the reduction of the exciton generation and dissociation efficiency.

Since the photoresponse in an organic transistor showed to be strongly time dependent, in order to compare different devices, especially if employed as phototransistors, it becomes fundamental to have information about the illumination time and the gate bias during illumination. The characteristic figures of merit used to define an inorganic phototransistor, such as the responsivity ($R = I_{ph} / P_{opt}$), the quantum efficiency ($\eta_{EQE}$) and the signal-to-noise ratio ($S/N = I_{illum} / I_d$), could not be relevant for an organic device if they were not supported by these details. An important and reliable parameter is the factor α which gives the direct relation between the main contribution to the photocurrent, i.e. the threshold shift, and the illumination time.

A comparison of the threshold voltage shift along the entire range of wavelengths could be difficult, because of the non-linear dependences on the optical power and illumination time. The problem could be solved by measuring the threshold voltage shift at a very low power density, so that Eq. (4.2) was approximated to:

$$\Delta V_T \cong \frac{AkT\eta_\lambda P_{opt}}{h\nu I_d}, \tag{4.11}$$

and a normalization to photon flux could be applied in order to evaluate the quantum efficiency (Fig. 4.11). The highest values appeared in correspondence to the Frenkel exciton levels of a pentacene thin film (2.1 and 2.3 eV). The threshold voltage shift, as was also seen through photocapacitance studies, could be used for the evaluation of the interface trap density.

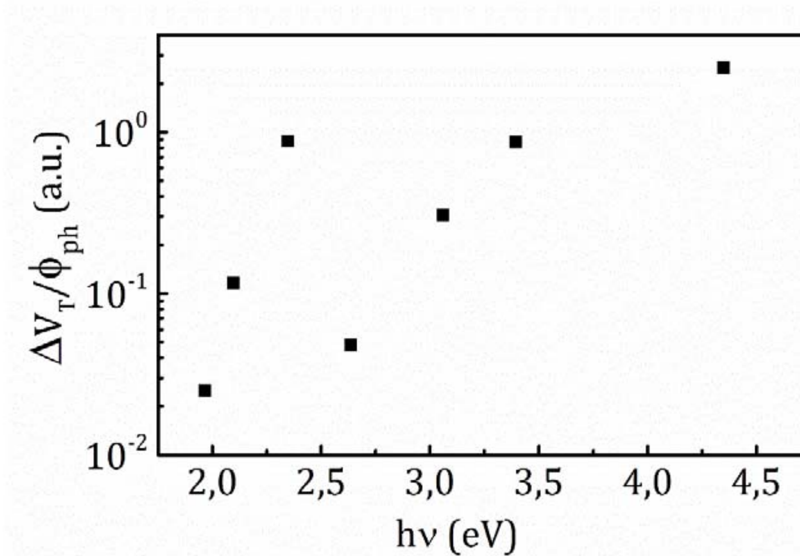


**Figure 4.11.** Light-induced threshold voltage shift weighted for incident photon flux density at different radiation energies. The extracted values are proportional to external quantum efficiency.

# 4.2 Defect evaluation through photocapacitance studies

Thin film transistors were fabricated with pentacene as active layer and with a copolymer. Capacitance measurements were performed under light conditions, in order to investigate the presence of traps in the pentacene film near the interface with the dielectric. From the study of the threshold voltage shift and the hysteresis phenomena induced by light irradiation, the type of trap states was investigated and trap surface density was extracted.

### 4.2.1 Pentacene based thin film transistors with PVP-co-PMMA dielectric

OTFT devices were fabricated in the bottom-gate top-contact geometry. The gate electrodes, consisting of 50 nm thick Al strips, were evaporated on a glass substrate. The insulating layer of the devices, having a thickness of 400 nm, was obtained from a solution of Poly(4-vinylphenol-co-methyl methacrylate) (PVP-co-PMMA) in xylene (5 wt%) by spin-coating. At this stage, two different approaches were developed: some devices were obtained with the as-deposited insulating film, the others by irradiating with UV light ($\lambda$=250 nm) for 15 minutes, yielding a cross-linked polymeric film. Then a pentacene active layer with a thickness of 50 nm was deposited by thermal evaporation for both the devices with base vacuum level of $2 \cdot 10^{-7}$ mbar. Gold source and drain electrodes were evaporated on the top through a shadow mask, while the gate dielectric and the organic semiconductor remained unpatterned.

OTFTs were electrically characterized at room temperature in ambient air and parameters were estimated in the saturation region where the current through the channel followed this equation:

$$I_{DS} = \frac{1}{2} \mu_{FE} C_i \frac{W}{L} \left( V_{GS} - V_T \right)^2 , \qquad (4.12)$$

where $I_{DS}$ is the drain current, $\mu_{FE}$ is the effective field effect mobility which was revealed to be independent from gate bias, $W$ and $L$ are the channel width and length, respectively, $C_i$ is the insulator capacitance, $V_{GS}$ and $V_T$ are the gate and threshold voltage, respectively. The threshold voltage and the mobility were determined on the base of Eq. (1b) from x-axis intercept and slope, respectively, of the $\sqrt{I_{DS}}$ - $V_{GS}$ curve [26]. Threshold voltages of -2.5V and 2.5V were obtained for untreated and UV-irradiated OTFTs, respectively. These results showed that the treatment after the dielectric deposition reduced trap states localized near the channel region and then a smaller voltage was needed so that the free carrier concentration could exceed the trap concentration. A good value for charge carrier mobility of 0.15 cm$^2$/Vs was measured in both transistors.

To obtain the transfer characteristics (Fig. 4.12), the gate-to-source voltage was swept between 40 V and -40 V in both directions, while keeping the drain-to-source voltage at -10 V. A slight and reversible hysteresis behavior was observed, with higher currents during on-to-off sweep compared to off-to-on sweep. The width of the hysteresis loop for the untreated devices was greater than in the TFTs with dielectric subjected to the cross-link reaction by UV light. This hysteresis effect, which resembled the metastable behavior observed in ferroelectric materials [27], could be attributed to polar groups, movable chains or solvent residuals contained in the PVP-co-PMMA layer; they could produce mobile dipoles, then oriented by the gate electric field. This polarization gave a further contribution to the externally applied gate field, so that the back sweep current was higher leading to a clockwise hysteresis loop. Over time, under bias stress and for effect of oxygen and moisture absorption, the size of hysteresis increased in both OTFTs, most likely due to water molecules, which increased the polarization effect with the introduction of polar O-H bonds [28].

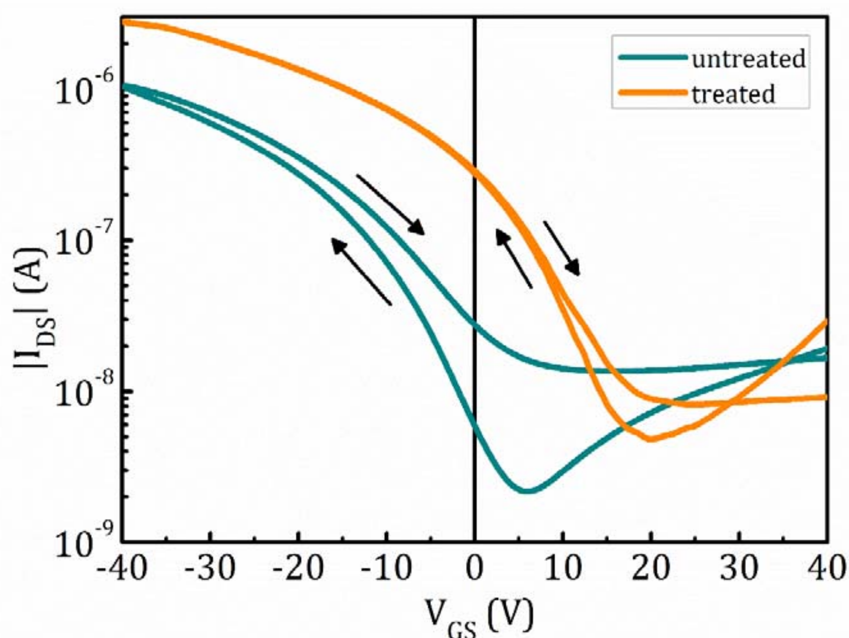


**Figure 4.12.** Transfer characteristics of an untreated (solid lines) and a treated (dashed lines) pentacene-based OTFT for $V_{DS}$=-10V. A clockwise hysteresis loop occurred in both cases.

### 4.2.2 Capacitance measurements in dark

The admittance measurements $Y=G+j\omega C$, where $G$ and $C$ are the conductance and the capacitance, respectively, of the parallel model of the MIS capacitor, were performed by electrically shorting the source and drain electrodes of the fabricated OTFTs to the low terminal of a LCR meter (Agilent E4980A), while the gate contact was connected to the high one. The input signal at LCR meter terminals was given by superimposing a small amplitude ac signal (100 mV) to a dc bias voltage (Fig. 4.13). By sweeping the bias voltage $V_{bias}$ between -40 and 40 V and by setting the frequency in the range from 20 Hz to 2 MHz, capacitance-voltage and conductance-voltage curves were simultaneously collected; the bias voltage was swept in both directions between off and on states in order to appraise hysteresis phenomena.

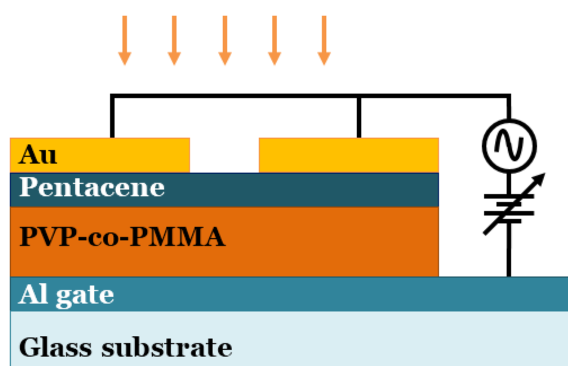


**Figure 4.13.** Cross section of the fabricated OTFTs and basic setup for capacitance measurements. Arrows indicate the photo-irradiation from the top.

The physical nature of pentacene, i.e. a p-type semiconductor where conduction occurred along a hole-accumulated channel, was evident from the C-V curves (Fig. 4.14): when the device was depleted of mobile charges, the measured capacitance was given by the series sum of the insulator and depletion capacitances; going toward the accumulation regime, the capacitance rapidly increased, similarly to the dc current in the transfer characteristics when the charges were accumulated at the interface with the insulator layer; in this case, the measured level consisted just of the insulator capacitance. In a MIS

structure, the dielectric is stacked between a metal electrode and an organic semiconductor. Thus, when a negative gate bias made the devices work in accumulation region, the permittivity of the polymer was determined (inset of Fig. 4.14).

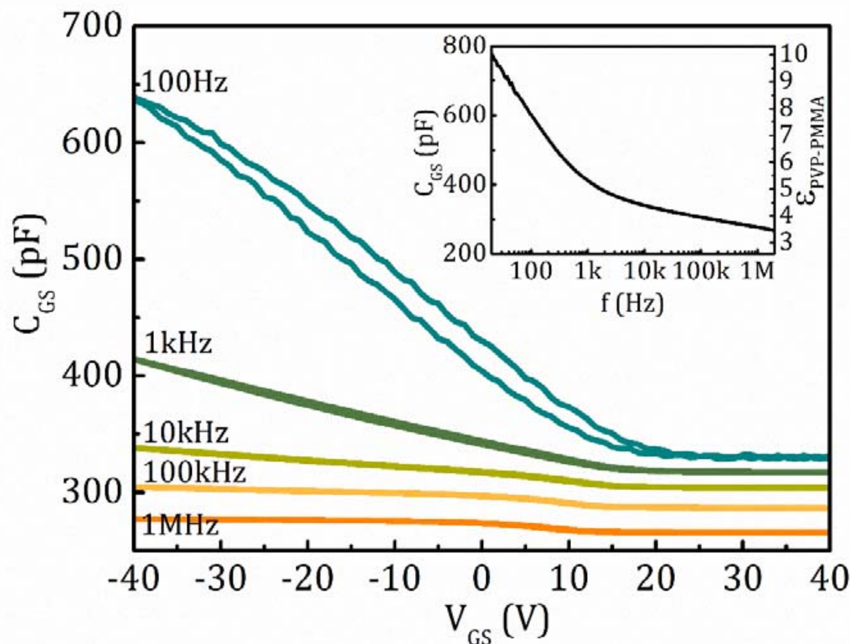


**Figure 4.14.** Capacitance-voltage curves for an Al/PVP-co-PMMA/Pentacene TFT. Inset: Overall capacitance in the accumulation region and extracted PVP-co-PMMA dielectric constant. Treated sample.

Here a strong frequency dependence arose. The frequency dispersion during C-V measurement in the accumulation region and the high value [29] of extracted permittivity persuaded of the presence of a parallel contribution to the overall capacitance. The misalignment between gate and top electrodes and the deposition of unpatterned insulator and semiconductor layers might create an edge parasitic effect, which became larger when the gate voltage shifted toward negative values. This phenomenon was confirmed by mechanically removing the organic material outside the channel region and not interposed between the overlapping electrodes. In this manner, it was seen that the peripheral pentacene region could significantly distort the C-V characteristics, especially at low frequencies. The contribution given by holes, available in the bulk of the semiconductor adjacent to

the MIS structure, to the extension of accumulation layer has been accurately obtained in [31]. This problem was later resolved by performing ac measurements on an organic based MIS capacitor.

In addition to this phenomenon associated to the peripheral semiconductor area, a decrease of the accumulation capacitance was present along the entire frequency range and was related to the Maxwell-Wagner dispersion because of the inability of majority holes in pentacene to follow the applied bias at higher frequencies.

### 4.2.3 Photo-capacitance measurements

In order to evaluate the presence of majority and minority carrier traps, high concentrations of both holes and electrons were needed. For this purpose, light sources at particular wavelengths were used to illuminate the devices, allowing the limitation of the low density of minority carriers to be overcome.

The optical experiments were developed over the range between 285 nm and 630 nm, using LEDs located at a few millimeters from the top of the device. It was fundamental to ensure that the irradiation hit the interface, where the major effects were expected to manifest. Thanks to the reduced thickness of the metal electrodes and the semiconductor layer, it was possible to irradiate the capacitor from the top, also avoiding the problem of the absorption in the glass substrate in the case of ultraviolet light.

Figure 4.15 shows the effect on a capacitance-voltage measurement (at signal frequency of 10 kHz) of two Al/PVP-co-PMMA/Pen devices when the structures were illuminated from the top (Fig. 4.13) by a LED at 365 nm with an irradiance of 1.4 mW/cm$^2$. The C-V curves exhibited a displacement to higher values, in addition to a translation along the voltage axis, suggesting an increase in the charge density. Moreover, a distinction was recognized between the untreated device (Fig. 4.15a) and the cured one (Fig. 4.15b).

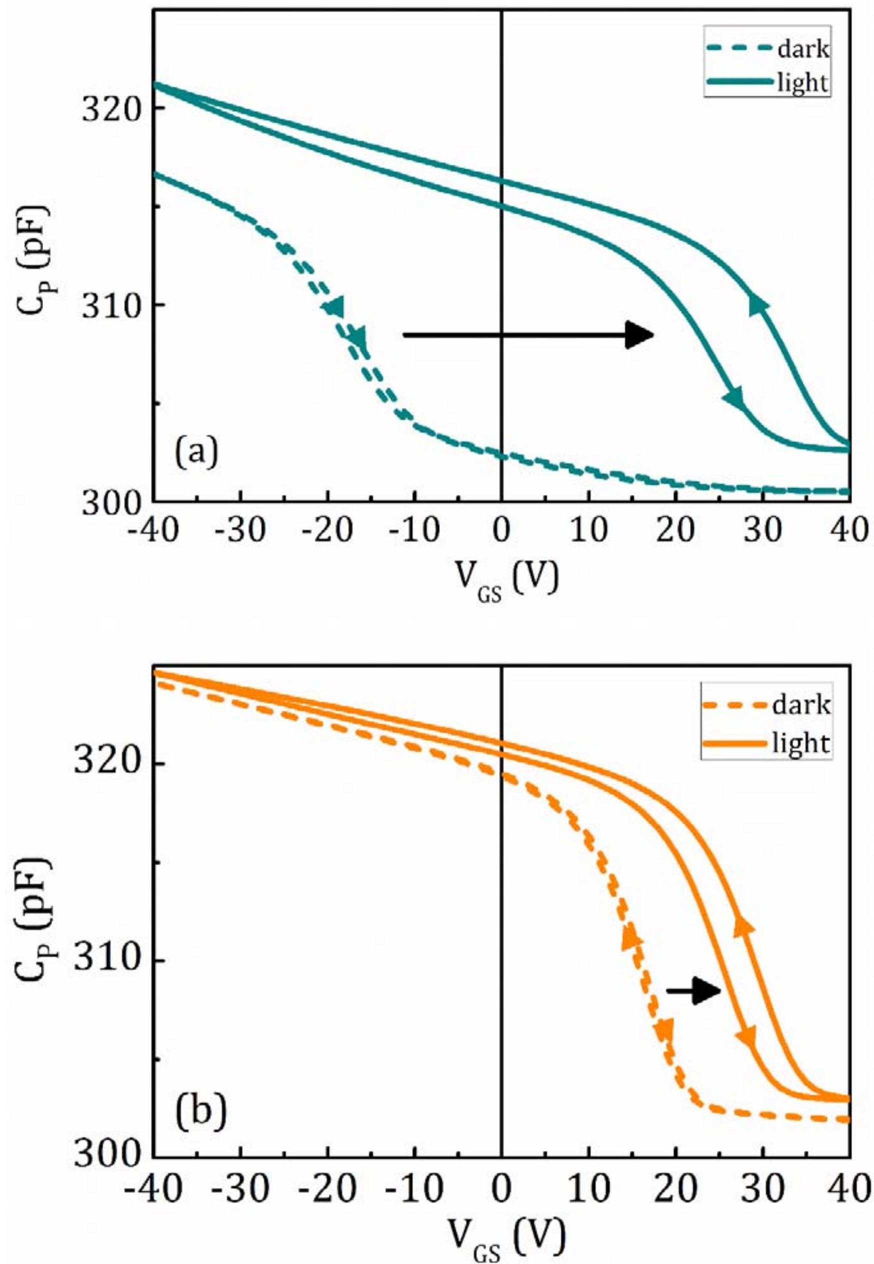


**Figure 4.15.** Capacitance-voltage curves in dark (dashed line) and under light ($\lambda$= 365 nm) conditions (solid line) at signal frequency of 10 kHz. Typical behaviour observed for all wavelenghts. The arrows on curves indicate the direction of hysteresis. Untreated (a) and treated (b) samples.

The behavior at $V_{GS}$=0 V could be used as a significant example. The non-irradiated OTFT was switched on at negative voltages, but photo-irradiation affected the device working region so that, when $V_{GS}$ was 0 V, it moved from depletion region in dark to accumulation under illumination; a different response was detected if the device was treated, because the OTFT worked already in accumulation mode and the shift of the capacitance under light was revealed to be smaller.

The shift seen in the C-V plots upon illumination, along with the introduction of hysteresis phenomena, was attributed to the presence of interfacial trap states, as well as the difference induced in devices by UV curing was related to the different quality of the semiconductor-insulator interface.

When light was absorbed, minority electrons were generated, together with majority holes, but due to their lower mobility they became trapped in the pentacene layer. Specifically under gate electric field in the depletion regime, they drifted toward the interface with insulator, where they were trapped and screened the semiconductor from the applied gate voltage. As a result, a higher positive voltage was needed to deplete the semiconductor [30]. This effect was reversible; indeed, after putting out the irradiation, the curves relaxed back to the pre-irradiation dark curve with no change in shape, indicating that interface states had thermally emitted their trapped electrons (Fig. 4.16).

Conversely, hole trapping at the semiconductor-insulator interface should be ruled out: indeed, if hole trapping centers had been present at the interface, when in accumulation, the probability of hole trapping in interface states would have been enhanced and a net positive charge would have reduced the hole concentration in the accumulation channel, by screening the negative voltage applied to the gate electrode. Consequently, the curves under light would have shifted in the direction opposite to that observed.

The threshold voltage of the transistors could be useful to estimate the upper limit for the density of charges trapped in interface states, $N_I$, through the following expression [31]:

$$N_I = -\frac{C_i}{q}\left[V_T - \left(\phi_m - \phi_s\right) + V_{inj}\right] \leq -\frac{C_i}{q} V_T, \qquad (4.13)$$

where $C_i$ is the insulator capacitance per unit area, $(\phi_m - \phi_s)$ is the difference between gate and organic semiconductor work-functions, $V_{inj}$ is a barrier depending on the injecting contact.

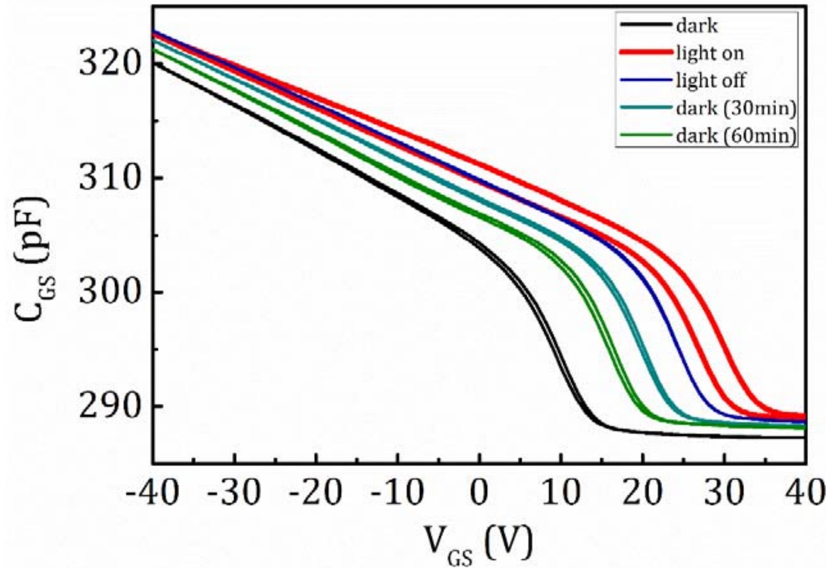


**Figure 4.16.** Typical recovery of capacitance characteristics after exposure to visible and near-UV light. Treated sample.

According to this relationship, the threshold voltage could give information about the sign of the net charge trapped in interface states. Similarly, under light conditions, the threshold voltage shift direction could indicate the type of interfacial states and provide an estimation of their density. By comparing the as-deposited and treated devices in dark, it was evident that the UV curing of the insulator layer generated mainly a negative interfacial fix charge, since for $V_{GS}$=0 V the accumulation layer was already formed in pentacene. Moreover, by analyzing the behavior under light conditions, the UV curing was also revealed to favor a better quality of the interface with a lower trap density. For both devices, illumination yielded a translation towards positive voltages, indicating the filling of electron traps at the interface.

The C-V characteristics could be employed to detect the gate voltage required to create a conducting channel [32], but, in an organic transistor operating in accumulation, due to the presence of trap states, the induced charges are not immediately available for conduction and a

threshold voltage is ill defined. However, from the C-V measurements it was possible to extract the threshold voltage shift upon illumination, thanks to the comparison between the dark and light curves. The voltage next to the inflection point of the C-V plots in the transition region (i.e. where concavity changed sign, $\partial^2 C / \partial V_G^2 = 0$) was taken as reference value for both curves. Therefore, the difference between the two measures, in dark and under light irradiation, gave the threshold translation and this value was supposed to be proportional to trapped electron surface density, through the following relation [33]:

$$\Delta V_T = \frac{q n_{it}}{C_i} \tag{4.14}$$

where $\Delta V_T$ is the shift in threshold voltage, $n_{it}$ is the variation in the carrier surface density trapped at the interface.

The amount of the resulting translation was revealed to depend on the wavelength, intensity (Figs. 4.17 and 4.18) and duration of the optical irradiation. The threshold voltage shift seemed to saturate to a maximum value, almost similar for every photon energy, when the devices were irradiated for prolonged periods. In addition, when high irradiancies were used, the behavior resembled the variation of the photovoltaic effect with optical power, previously illustrated in Eq. (4.2). These observations suggested the dependence of the irradiation effects on the photon dose. Finally, by removing the irradiation source, the curves relaxed back to the original condition (Fig. 4.16), except for an irradiation at a wavelength of 285 nm (Fig. 4.19).

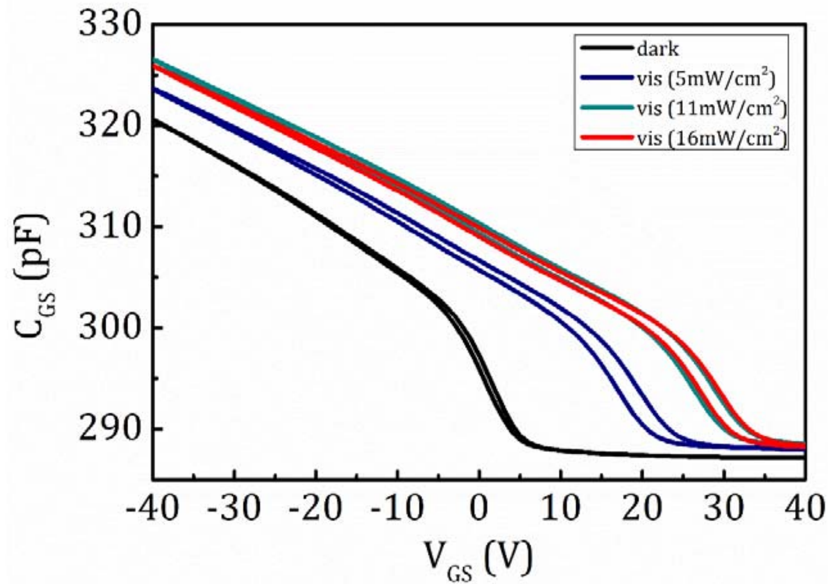


**Figure 4.17.** Capacitance-voltage curves under visible light (630 nm) irradiation for different irradiances. Treated sample.

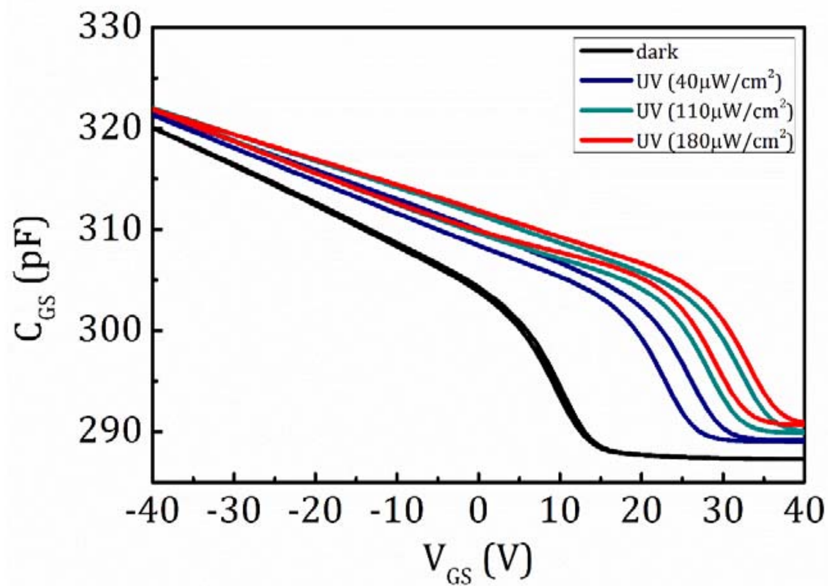


**Figure 4.18.** Capacitance-voltage curves under ultraviolet light (365 nm) irradiation for different irradiances. Treated sample.

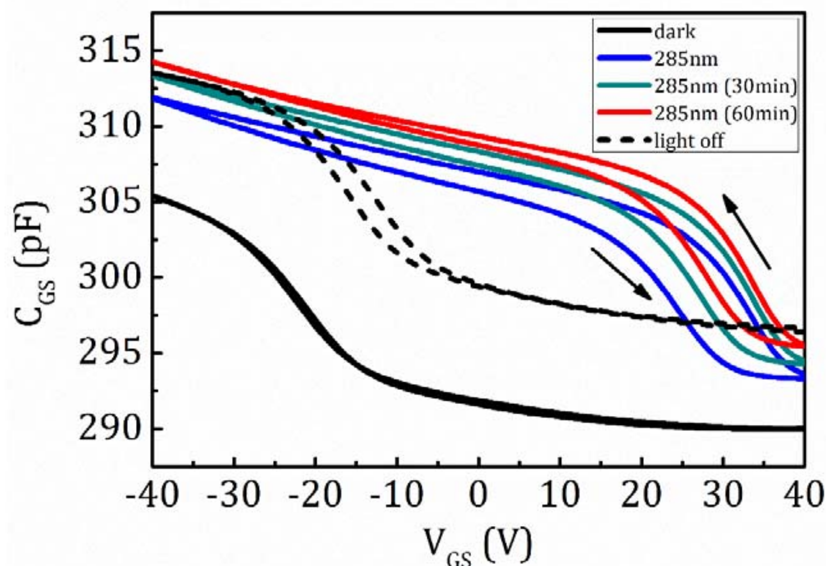


**Figure 4.19.** Capacitance-voltage curves under and after ultraviolet light (285 nm) irradiation at 170 µW/cm$^2$. Untreated sample.

## 4.2.4 Interface trapping

It was seen that, as a consequence of irradiation, the photogenerated electrons in pentacene layer, upon drifting to the interface especially when a positive gate bias was applied, became deeply trapped, inducing a shift in the threshold voltage toward more positive values. This shift was combined with a reduced slope during the off-to-on sweep, indicating the gradual detrapping of electrons accumulated at the interface states, as further confirmed by the hysteresis which occurred when the voltage sweep was reversed. At the same time, the minimum of the capacitance, exhibited by the device when it was driven into depletion, was higher and more stable than the value reached in the dark. This behavior suggested a change in the dependence of the depletion region width on the applied bias and was correlated to the variation of the flatband voltage. Both threshold voltage shift and variation of the minimum capacitance level were revealed to change with photon energy and light intensity, as well as with exposure time,

indicating that both parameters depended on photon dose and could reach a saturation level.

In the pentacene layer, the concentration of electrons should be so low that trapping was not observed in dark. On the contrary, under illumination the photons absorbed could generate a large number of charge carriers. The photogeneration in an organic material proceeds mainly via formation of strongly bound Frenkel-type molecular excitons. High transverse electric fields could be effective in dissociating excitons into holes and electrons (Fig. 4.20). In particular, when high positive biases were applied, the semiconductor was depleted of holes, while electrons, escaped from recombination, drifted to the interface.

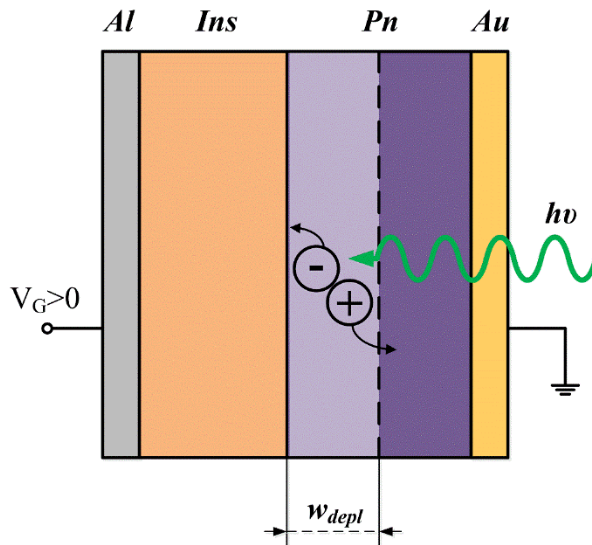


**Figure 4.20.** Dissociation of an exciton in the section of a metal-insulator-organic semiconductor structure. Device is polarized in depletion region.

According to the geminate recombination theory [34], the dissociation probability, $P_{diss}$, strongly depends on the external electric field and temperature, following this relation:

$$P_{diss}(E,T) = \frac{k_D(E)}{k_D(E)+k_F} \quad , \tag{4.14}$$

where $T$ is the temperature, $E$ is the electric field, $k_F$ is the decay rate to the ground state. The dissociation rate of a bound pair, $k_D$, has the form:

$$k_D(E) = k_D(0)\left(1 + b + \frac{b^2}{3} + \dots\right), \tag{4.15}$$

with $k_D(0)$ depending on the exciton binding energy and $b = q^3 E / \left(8\pi\varepsilon k_B^2 T^2\right)$.

The increase of electron density shifted the electron quasi Fermi level toward the LUMO, so that more interfacial traps could be filled (Fig. 4.21). The result was the reduction in the band bending and the width of depletion region, visible through the screening effect of the gate voltage and the shift in depletion capacitance.

The instantaneous width of the depletion region [35], $w_{depl}$, should change over time according to this expression:

$$w_{depl}(\mathrm{t}) = \sqrt{\frac{\varepsilon^2}{C_i^2} + \frac{2\varepsilon}{qN_A}\left(V_G(t) - V_{fb}(t)\right)} - \frac{\varepsilon}{C_i}, \tag{4.16}$$

where $\varepsilon$ is the permittivity of the organic semiconductor, $N_A$ is the doping density and $V_{fb}$ is the flatband voltage. The time indicates the dependence on the photon dose. Therefore, the flatband voltage and the threshold voltage shift were proportional to the total electron density trapped during exposure time:

$$\Delta V_T(\mathrm{t}) = \frac{qn_{it}(t)}{C_i} = \frac{q}{C_i}\int_0^t n_{it}(\tau)\, d\tau, \tag{4.17}$$

where $n_{it}(t)$ represents the rate of interface electron trapping.

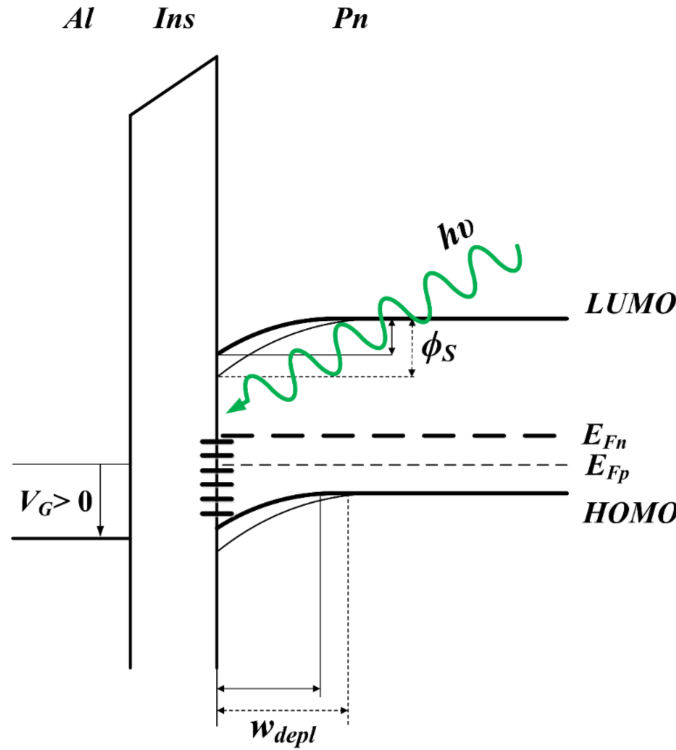


**Figure 4.21.** Effect of photon absorption in the band diagram of the MIS structure. $\phi_S$ is the surface potential, $w_{depl}$ is the width of depletion region.

The low frequency capacitance $C_O$, at a given gate voltage, corresponded to the series sum of the insulator and depletion capacitances:

$$C_O^{-1}\left(V_G\left(t\right),t\right)=C_i^{-1}+\frac{w_{depl}\left(V_G\left(t\right),t\right)}{\varepsilon}, \tag{4.18}$$

where, in particular, the dependence on time was introduced to consider the shift effect that light exposure, along with gate bias, had on the threshold voltage. It followed that the minimum value of capacitance reached under illumination should be higher than the geometric capacitance observed in dark. The capacitance measured in depletion region under illumination was also fairly constant. This stability indicated that the exciton dissociation and the trapping efficiency were high enough to let the flatband voltage follow perfectly the gate voltage

sweep. In this case, the depletion region was not able to expand up to the full depletion of the semiconductor layer. Thus, the charge space was replaced by free charge, and moreover, at sufficiently high free electron concentrations, the formation of an inversion layer could also be supposed.

The results obtained upon applying an optical excitation were compared for different wavelengths.

If all interface traps were filled, the values of threshold voltage shift were not weighted for the number of photons. In this case, the translations exhibited a maximum value, which was found to be nearly independent from wavelength in the visible range, confirming that saturation was reached. However, the behavior under ultraviolet light was different, since the shorter the wavelength of UV radiation was, the wider the threshold voltage translation seemed to be, indicating that an even higher number of electrons was trapped. A possible explanation for this phenomenon was sought in the increase of the optical cross-section with the energy of the incident light [36], or otherwise in the UV light induced creation of defects in the pentacene film [37], correlated with the lack of trapping saturation. Moreover, as a consequence of UV light at 285 nm, the recovery curve (Fig. 4.19) in the following dark exhibited a threshold voltage which tended to restore to the original value, but, at the same time, a minimum capacitance in depletion region which remained even higher. This behavior could be due to an increase in the doping density $N_A$ and it was attributed to an accelerating oxidation of the pentacene layer under ultraviolet light.

Thanks to reduced localized trap states at the interface in the OTFTs with cured polymer, the threshold voltage shift in the visible light range was lower than in the untreated samples (Fig. 4.22). For an insulator capacitance $C_i$= 8.8 F/cm$^2$, the interface electron trap densities were extracted from the threshold voltage shift and were discovered to be about $2.8 \cdot 10^{12}$ cm$^{-2}$ and $5 \cdot 10^{11}$ cm$^{-2}$ for the untreated and cured OTFTs, respectively.

On the other hand, far from the trapping saturation, where the magnitude of the threshold voltage shift should be still proportional to the optical power, the measured translation values could be normalized to the incident photon flux density. The dependence of the minimum capacitance difference and the threshold voltage shift, between dark and light conditions at a given wavelength, could allow to estimate the quantum efficiency as a function of radiation energy. However, some radiation wavelengths induced a rapid saturation and it was not possible

to estimate the quantum efficiency in the entire energy range. The remaining results, not shown here, demonstrated that the pentacene film accumulated charges at the interface especially under illumination at 2.1 and 2.3 eV, confirming that photogeneration occurred especially through the Frenkel exciton states of pentacene.

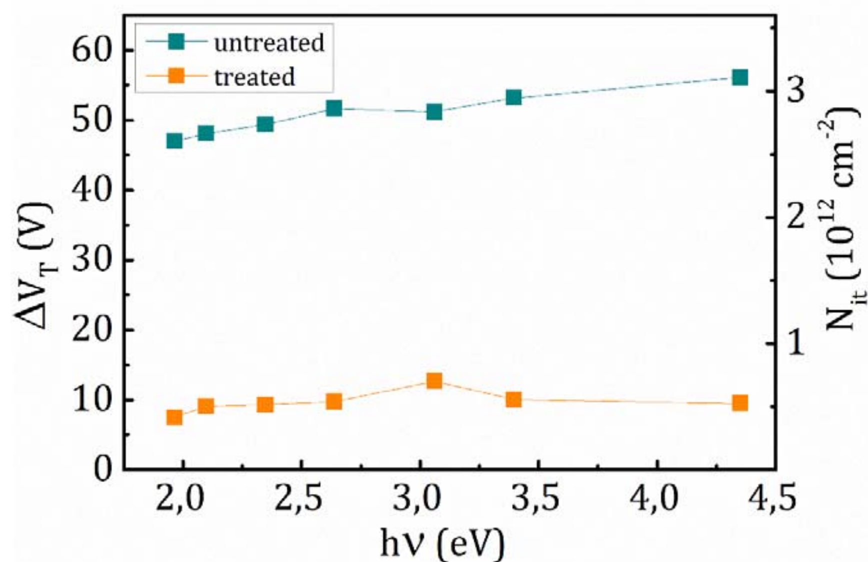


**Figure 4.22.** Maximum threshold voltage shift at various light wavelengths, for untreated and treated samples, and exctracted interface trap density.

### 4.2.5 Light-induced hysteresis

While in dark both the forward and the reverse voltage sweeps traced nearly overlaying paths, with a narrow clockwise hysteresis, under light conditions strong hysteresis phenomena, with an anticlockwise loop, were generated. The scan of the C-V curves was started from the off state ($V_{GS}$=40 V), with the devices working in depletion region. Then the gate voltage was swept toward negative values, when an accumulation layer created a conductive channel at the insulator-semiconductor interface and the capacitance was equivalent to that of the dielectric layer. Upon reaching a gate voltage of -40 V, $V_{GS}$ was swept back to positive voltages. In this case, the resulting capacitance was lower and the C-V curve looked like translated toward

negative values along voltage axis (Fig. 4.15). This kind of hysteresis had a different origin in contrast with insulator-based dark hysteresis; in particular, it could be the result of two mechanisms: hole traps filled at negative gate voltages and electron traps filled at positive gate voltages. The dominant factor was supposed to be the fast filling and the slow emptying of traps in the semiconductor near the interface with the dielectric.

If the presence of majority traps was supposed, at the beginning of $V_{GS}$ sweep they would be expected to be empty. During the off-to-on scan, while positive charges drifted to the interface, some of the accumulated holes would be trapped. As a consequence of the positive trap filling, upon sweeping the gate voltage back from accumulation to depletion region, free available charge carrier density in the channel at any given negative value of $V_{GS}$ would decrease. This process might result in a translation of threshold voltage toward more negative values, due to a release rate of hole traps slower than the scan rate.

If minority traps were supposed in pentacene, at the beginning of $V_{GS}$ sweep the fast centers should be filled. When the applied gate voltage was swept from positive values toward the on state, the negatively charged traps at the semiconductor-insulator interface should induce more mobile holes than the number of field-induced positive charges corresponding to a given gate voltage. This would cause capacitance values to increase at each transverse electric field. While keeping the device in accumulation region, electrons should be released. Because negative traps should have been emptied, lower capacitance occurred in the back sweep, resulting in an anticlockwise hysteresis loop, indicating again that the scan rate of the gate voltage was faster than the time needed to reach thermal equilibrium.

Although the hysteresis with an anticlockwise direction could be generated by both types of traps, it was reasonable to rule out the prevalence of hole traps according to various justifications. First of all, this hysteresis phenomenon was observed only when the devices were subjected to light irradiation, which created high density of electrons as well as holes. Since pentacene acted as a p-type semiconductor, the majority charge carriers were holes but they did not generate hysteresis in dark. This demonstrated that hole traps were either absent or emptied very rapidly. In addition, the threshold voltage translation toward positive values under light irradiation represented a clear proof of the prevalence of electron traps, whose surface density at the

semiconductor-dielectric interface was extracted from the width of the maximum threshold voltage shift.

In addition, as illustrated in Fig. 4.23, the hysteresis loop width changed with the signal frequency at which the capacitance measurements were performed. In particular, the hysteresis size exhibited a minimum at a signal frequency of about 300 kHz, while increased toward both lower and higher frequencies.

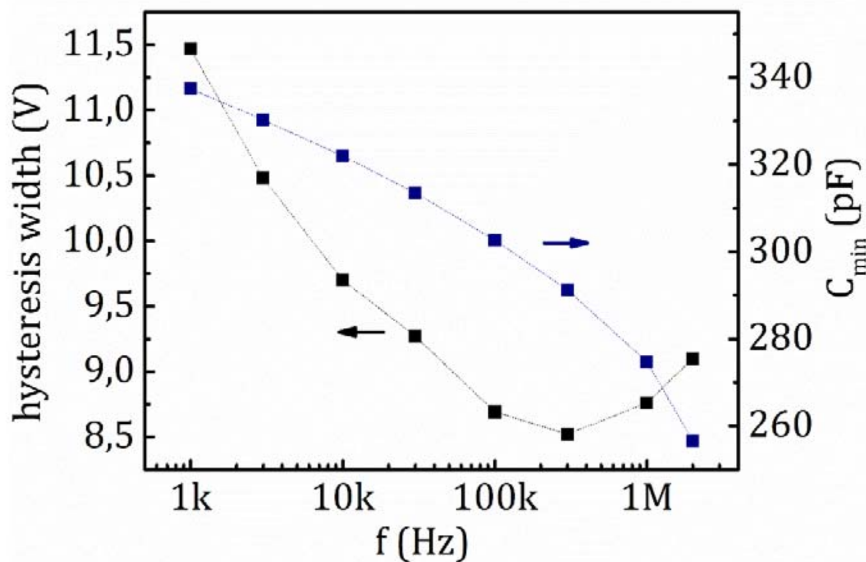


**Figure 4.23.** Dependence of light-induced hysteresis width and minimum capacitance measured in depletion region on ac signal frequency.

Since the presence of long-lived deep traps was indicated as the origin of curves shift and hysteresis phenomena, the faster the measurement was with respect to the release rate of charge from traps, the greater the number of filled traps was when the voltage was swept from off to on state. For this reason, at a high signal frequency more holes were induced in proximity of interface, resulting in an earlier threshold voltage. This phenomenon explained the larger hysteresis seen for very rapid sweeps. However, with a slower ac signal, the dc level took a longer time to sweep in the same voltage range during the measurement, causing the device to be exposed to a greater photon dose and a larger density of electrons to become trapped at the interface during the depletion regime. This mechanism induced an even greater magnitude of the hysteresis loop for very low frequencies. At the same

time, in regards to the dispersive transport of the pentacene semiconductor, with a slower measurement a larger majority carrier density was induced as well. Meanwhile, by reducing the signal frequency, $C_{min}$ always showed a trend reflecting the increase in the photon dose absorbed.

### 4.2.6 Admittance spectroscopy

Admittance-frequency curves were also collected, over the range from 20 Hz to 2 MHz. The study of the admittance spectra should be useful to construct the distribution of states, as discussed further on. The imaginary and the real part of admittance of the MIS structure when $V_{GS}$ is 40 V was illustrated in Fig. 4.24.

Since the device worked in depletion region, it should be possible to define the properties of the semiconductor bulk. Sharp peaks were not observed, but a wide plateau appeared in the loss plot, i.e. the conductance divided by the angular frequency ($G/\omega$), in the middle of the frequency range, while the capacitance always decreased as frequency rose. Since low signal frequency lets deep states to be investigated, on the basis of these plots it was concluded that deposited pentacene thin film was characterized by a broad peak in density of state distribution near midgap and a hole tail near HOMO. These results reflected the studies of Lang and Cohen [38], who proposed a variety of examples of matching between arbitrarily shaped density of state distribution and the expected results for admittance versus temperature for silicon and amorphous semiconductors. For this reason, it was evident that the UV curing of the polymer insulator yielded the growing of the pentacene film with a narrower band tail. Moreover, by illuminating the transistor with LEDs, an increase in capacitance and conductance was observed and was attributed to the reduction of the depletion layer and the enhancement of free carriers.

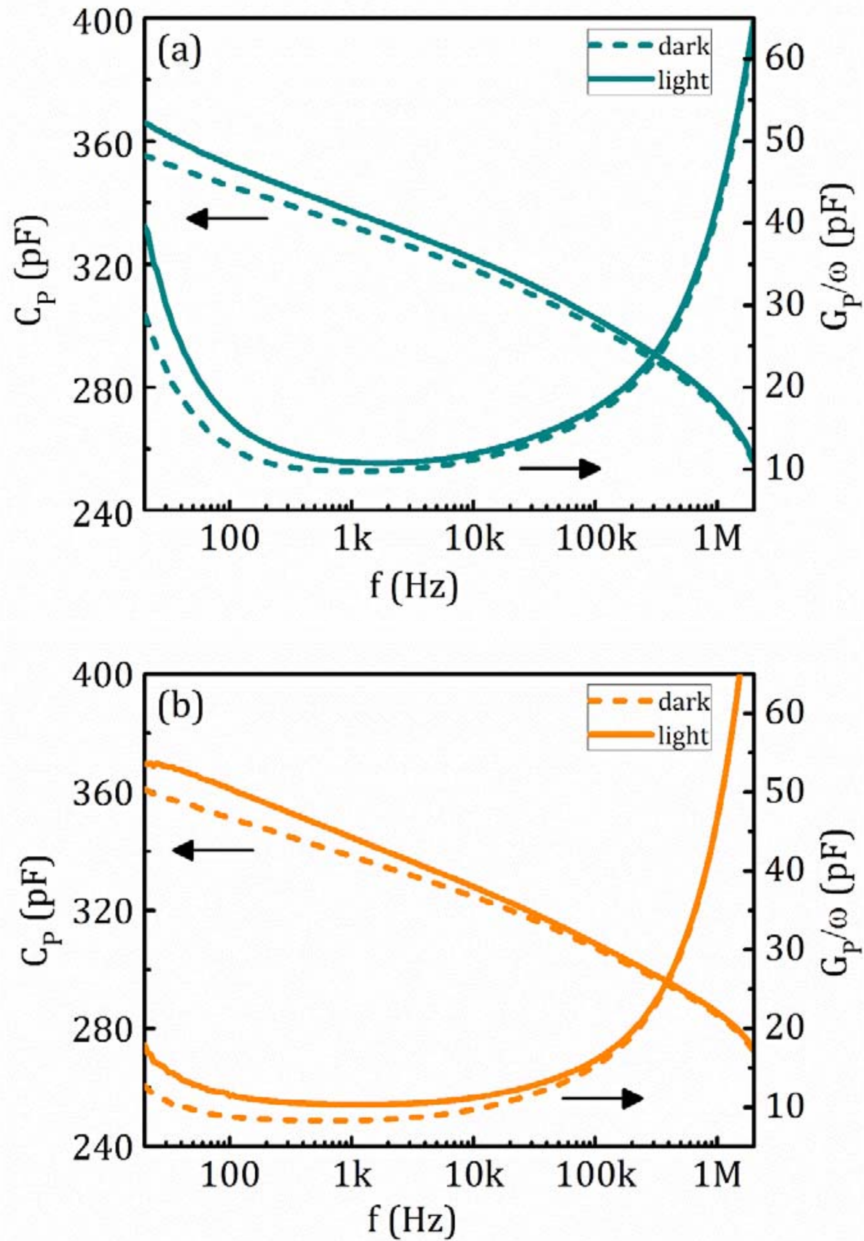


**Figure 4.24.** Frequency-dependence of the parallel capacitance, $C_P$, and loss, $G_P/\omega$, of the MIS devices in depletion region ($V_{GS}$=40 V) for untreated (a) and treated (b) samples.

## 4.3 Conclusion

The presence of interface traps in a pentacene-based thin film transistor was discussed. The long-lived trapping at the insulator-semiconductor interface and in dielectric states are not wished in a transistor because it was revealed to cause threshold voltage instability; on the contrary, the presence of deep traps, in case they were controllable, could be exploited in the realization of charge storage transistors.

The comparison between the electrical characterizations in dark and the results obtained under light conditions was used to analyze the conduction properties and the trapping mechanisms occurring at the insulator-semiconductor interface in an OTFT. Examples of both current and capacitance measurements were reported.

Photocurrent studies on an organic transistor allowed to distinguish the photovoltaic and photoconductive effects. Then, photocapacitance measurements were proposed as an efficient alternative to photocurrent techniques in order to investigate the origin of the threshold voltage shift introduced by irradiation and to obtain information about trap states and photoconductive efficiency in the organic semiconductor.

At a certain photon energy, a high concentration of free charges was induced by exciton dissociation. When a fraction of free electrons, escaped from exciton recombination, drifted to the interface they became trapped and induced a positive shift of flatband voltage. At the same time, the depletion layer width reduced. The interface states were mainly electron traps, which filled fast and emptied slowly leading to an anticlockwise hysteresis under light conditions.

In order to obtain meaningful results, a structure different from a transistor was required. Working with a patterned MIS capacitor was revealed to be more effective, since the contribution of the orthogonal current flowing through the accumulation channel and the effect of peripheral semiconductor were limited. Furthermore, it became necessary to conceive a model which took into account the dispersion in the organic material at low frequencies.

# References

1. C.D. Dimitrakopoulos and P.R.L. Malenfant, Adv. Mater. **14**, 99 (2002)
2. M. Dong, L. Zhong, IEEE Trans. Mobile Computing **11**, 1587 (2012)
3. H. Klauk, M. Halik, U. Zschieschang, G. Schmid, W. Radlik, and W. Weber, J. Appl. Phys. **92**, 5259 (2002)
4. M. Kaltenbrunner, M.S. White, E.D. Glowacki, T. Sekitani, T. Someya, N.S. Sariciftci, and S. Bauer, Nature Communications **3**, 770 (2012)
5. D.K. Hwang, J.H. Park, J. Lee, J-M. Choi, J.H. Kim, E. Kim, and S. Im, J. Electrochem. Soc. **153**, (1) G23 (2006)
6. G. Horowitz, J. Mater. Res. **19**, 1946 (2004)
7. Y-Y. Lin, D.J. Gundlach, S. Nelson, and T.N. Jackson, IEEE Trans. Electron Devices **44**, 1325 (1997)
8. R. Liguori, E. Santoro, M. Petrosino, and A. Rubino, Proc. 45th GE Conf., 31 (2013)
9. R. Liguori, W. C. Sheets, A. Facchetti, and A. Rubino, “Light- and bias-induced effects in pentacene-based thin film transistors with photocurable polymer dielectric”, Organic Electronics. Submitted.
10. R. Liguori, M. Petrelli, M. Petrosino, and A. Rubino, “Defect evaluation in pentacene thin film transistors through photocapacitance studies”, 9th International Conference on Organic Electronics (Grenoble, 2013)
11. R. Liguori, and A. Rubino, “Defect evaluation in pentacene thin film transistors through photocapacitance studies”, Organic Electronics. Submitted.
12. D.M. Taylor, J.A. Drysdale, I. Torres, and O. Fernández, Appl. Phys. Lett. **89**, 183512 (2006)
13. K. Kim, and Y. Kim, IEEE Trans. Electron Devices **57**, 2344 (2010)
14. Y-M. Chen, C-F. Lin, J-H. Lee, and J.J. Huang, Solid-State Electr. **52**, 269 (2008)
15. R.S. Crandall, Appl. Phys. Lett. **42**, 451 (1983)
16. J. D. Cohen and D. V. Lang, Phys. Rev. B **25**, 5321 (1982)
17. T. Walter, R. Herberholz, C. Müller, and H.W. Schock, J. Appl. Phys. **80**, 4411 (1996)
18. D.M. Taylor, I. Torres, and J. Drysdale, Proceedings of the 12th International Symposium on Electrets (ISE 12), 370 (2005)
19. I. Torres, and D.M. Taylor, J. Appl. Phys. **98**, 073710 (2005)
20. N. Alves, and D.M. Taylor, Appl. Phys. Lett. **92**, 103312 (2008)

21. A. Vollmer, O.D. Jurchescu, I. Arfaoui, I. Salzmann, T.T.M. Palstra, P. Rudolf, J. Niemax, J. Pflaum, J. P. Rabe, and N. Koch, Eur. Phys. J. E **17**, 339 (2005)
22. D. Kawakami, Y. Yasutake, H. Hishizawa, and Y. Majima, Jpn. J. Appl. Phys. **45**, L1127 (2006)
23. C.-S. Choi, H.-S. Kang, W.-Y. Choi, H.-J. Kim, W.-J- Choi, D.-H. Kim, K.-C. Jang, and K.-S. Seo, IEEE Photonics Technol. Lett. **15**, 846 (2003)
24. M. C. Hamilton, S. Martin, and J. Kanicki, IEEE Trans. Electron Devices **51**, 877 (2004)
25. G. Horowitz, M. E. Hajlaoui, and R. Hajlaoui, J. Appl. Phys. **87**, 4456 (2000)
26. D. K. Schroder, *Semiconductor Material and Device Characterization*, 3rd ed. (Wiley, New York, 2006)
27. R. C. G. Naber, P. W. M. Blom, G. H. Gelinck, A. W. Marsman, and D. M. de Leeuw, Adv. Mater. **17**, 2692 (2005)
28. K-M. Byun and W-J. Lee, Thin Solid Films **376**, 26-31 (2000)
29. S.H. Kim, J. Jang, H. Jeon, W. M. Yun, S. Nam, Appl. Phys. Lett. **92**, 183306 (2008)
30. I. Torres, D.M. Taylor, and E. Itoh, Appl. Phys. Lett. **85**, 314 (2004)
31. C. S. Suchand Sangeeth, P. Stadler, S. Schaur, N. S. Sariciftvi, and R. Menon, J. Appl. Phys. **108**, 113703 (2010)
32. M. M. Lau, C. Y. T. Chiang, Y. T. Yeow, and Z. Q. Yao, IEEE Trans. Electron. Dev. **48**, 1742 (2001)
33. S.M. Sze, *Physics of Semiconductor Devices* (Wiley, New York, 1981)
34. C. L. Braun, J. Chem. Phys. **80**, 4157 (1984)
35. C. C. Hu, *Modern Semiconductor Devices for Integrated Circuits*, 1st ed., Prentice Hall (2009)
36. T.H. Gfroerer, D.G. Hampton, P.R. Simov, and M.W. Wanlass, J. Appl. Phys. **107**, 123719 (2010)
37. R. Liguori, and A. Rubino, “Metastable light induced effects in pentacene”, Organic Electronics. Submitted
38. J. D. Cohen and D. V. Lang, Phys. Rev. B **25**, 5321 (1982)

# Chapter 5

# Admittance spectroscopy in an organic based MIS capacitor

Organic thin film transistors hold promise for low-temperature, large-area and low-cost applications. However, due to the considerable variability often observed in device behavior, the electrical performance and stability [1] need to be improved. This purpose could be achieved chiefly by the development of the theoretical interpretation of electronic and optical properties of OTFTs. Considerable effort has been devoted to the understanding of device physics, including the transport mechanisms in organic material, charge injection processes and carrier trapping phenomena [2-9]. The disorder degree could significantly affect the device operation, but the most critical aspect is represented by the interface formed between the organic semiconductor and the dielectric layer used [10,11].

In the previous chapter, photocapacitance measurements were revealed to be effective in investigating the presence of traps located at insulator-semiconductor interface. Experiments suggested that the instability of threshold voltage showed by organic thin film transistors could be induced by electron traps and that the effects were enhanced by the operation in depletion region. However, also holes traps play a critical role in the device performance. A good evidence was given by the dependence of mobility on gate bias versus threshold voltage. The multiple trapping and release mechanism for holes was used to explain this behavior.

Accurate analytical models, with their basis in physical theory, are required to predict the device behavior. For this purpose, two terminal devices were fabricated, with the same layer structure of thin film transistors. They formed organic-based metal-insulator-semiconductor (MIS) capacitors and were studied in order to investigate the mechanisms occurring in each layer of an organic field effect device.

The dynamic electrical response was analyzed under ambient conditions over a wide frequency range as a function of the dc bias. In particular, admittance spectra were employed. This technique was revealed to be a powerful tool able to discriminate the different processes involved in the device. The results, obtained by the application of this method to organic-based junctions, were usually interpreted by relying on models based on the Shockley-Read-Hall statistics, but they were often found to be unappropriated to organic materials.

A new electrical model was developed as an alternative to the previous works. It allowed the description of the different dynamics observed in organic devices fabricated with different materials. The parameters used in the proposed model were related to the device structure and fabrication processing. The number of factors was enough to describe a large amount of device properties and physical processes, while empirical parameters were avoided. The model allowed meaningful simulations and an efficient parameter extraction method.

## 5.1 Admittance measurements in pentacene-based MIS capacitors

MIS capacitors (Fig. 5.1) were fabricated starting from a heavily p-doped silicon wafer, whose thermal silicon dioxide layer with a thickness of about 400 nm was used as gate dielectric. A pentacene film with a thickness of about 60 nm was deposited by thermal evaporation, with a base vacuum level of about $2 \cdot 10^{-7}$ mbar. The small molecule film was grown with a deposition rate of 0.5 Å/s, keeping the substrate at room temperature. Subsequently, a gold electrode – hereinafter referred to as source – with a diameter of 2 mm was evaporated on the top. The same shadow mask was used to pattern the semiconductor layer and the electrode, in order to avoid peripheral effects. For each sample, a small part of surface was left free of organic semiconductor, in order to allow the access on the equivalent MIM junction. It was used for the reference measurements to be compared with the organic MIS structure.

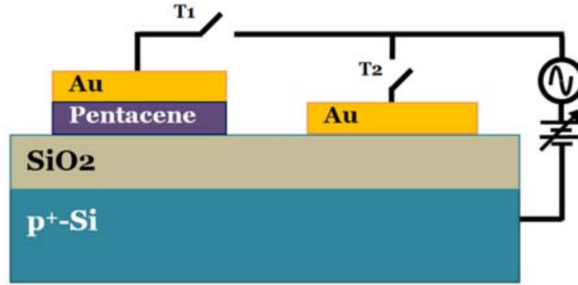


**Figure 5.1.** Cross section of the MIS and MIM junctions, fabricated on a silicon wafer. The connections represent the basic setup used for capacitance measurements: $T_1$ on for MIS capacitance measurement, $T_2$ on for MIM measurements.

The admittance of the device was measured using an Agilent E4980A LCR meter. Due to the high impedance values, measurements were performed with a three-terminal configuration. The gate contact of the capacitor under test was connected to the high terminal of the instrument, while the source electrode to the low one. Moreover, in order to improve the measurement accuracy and reduce the noise, the outer shielding conductors of the coaxial cables were connected to the guard terminal. A better improvement was achieved by connecting the two outer conductors to each other at the ends of the cables (Fig. 5.2). A small signal with an amplitude of 100 mV was superimposed to the dc bias between gate and source terminals, while frequency ranged from 200 Hz to 2 MHz. The input signal was swept between -40 and 40 V. Two kinds of compensation were executed before measurements: open and short compensations allowed reducing the effects of the residual series impedance and parallel admittance, respectively, of measuring connections and cables, as well as the error introduced by contact resistances.

The instrument was set in order to provide the capacitance $C_P$ and the conductance $G_P$, according to the parallel circuit model. The complex admittance, $Y(\omega)$, could be written as:

$$Y(\omega) = j\omega C_P(\omega) + G_P(\omega) = j\omega\left[C_P(\omega) - j\frac{G_P(\omega)}{\omega}\right], \tag{5.1}$$

where ω is the angular frequency. $C_P$ contained information about the polarization properties, including the response of both fast species, able to follow instantaneously the electric field, and slow species, such as

ions, defects and impurities. The imaginary part of the capacitance, i.e. conductance divided by angular frequency, $G_P/\omega$, took account of the energy dissipated by the device and was referred to as loss ($L_P$).

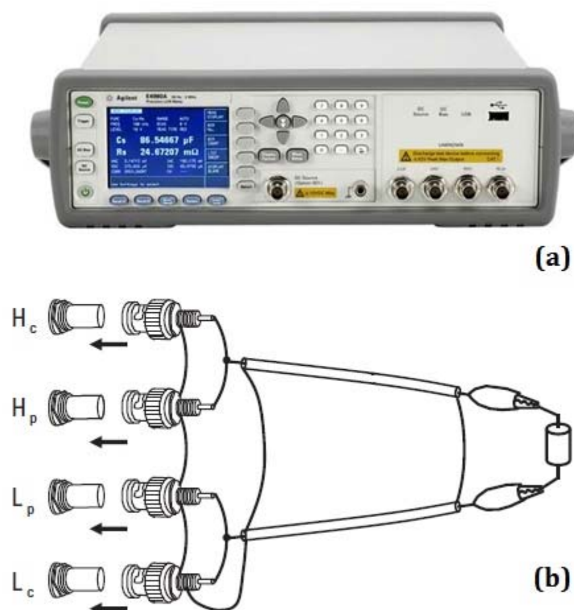


**Figure 5.2.** Agilent E4980A Precision LCR Meter (a) and terminal configuration used for admittance measurements (b). The four terminals are $H_{cur}$ (high current), $H_{pot}$ (high potential), $L_{pot}$ (low potential), $L_{cur}$ (low current).

The admittance characteristics of the MIS and MIM junctions were reported in Figures 5.3 and 5.4 as function of the signal frequency; the linear plot (Fig. 5.3) underlined the variations along the capacitance curves, while the logarithmic scale (Fig. 5.4) pointed out the dispersion peaks exhibited by the loss curves.

Different biases were used, ranging from accumulation regime at $V_{GS}$=-40 V to depletion regime at $V_{GS}$=40 V. Since the MIS structure was based on a wide bandgap semiconductor, inversion was not observed, because of the extremely long generation times of the minority carriers, but, for high positive gate voltages, the device was driven into deep depletion, i.e. the depletion region extended across the full thickness of the semiconductor layer up to the contact.

At the lowest frequencies, the capacitance depended on the bias. In particular, the highest capacitance value was exhibited when the device

worked in accumulation and should correspond to the insulator capacitance. Then, while the pentacene layer was being depleted, the capacitance decreased and should equal the series sum of the insulator and depletion layer capacitances. When the device was fully depleted, the capacitance reached the lowest level, defined as the device geometric capacitance, given by the series sum of the insulator and semiconductor layer capacitances.

On the contrary, the capacitance observed at higher frequencies (10÷100 kHz) was weakly dependent on the bias and, in particular, was close to the geometric capacitance. This phenomenon was related to the finite conductivity of the semiconductor bulk. The dispersive transport, due to the structural disorder of organic layer, imposed an upper limit on the frequency up to which the injected holes were able to follow the applied ac signal. This critical frequency was evident from the loss curves: it fell in the range 1÷10 kHz and gave information about the transport properties of pentacene bulk in direction perpendicular to the interface.

Before semiconductor relaxation occurred, another dispersion phenomenon was observed in the range from 20 Hz up to about 1 kHz (Fig. 5.3). Its gradual shift to lower frequencies, as the device was driven into depletion, suggested that it was originated by the presence of interface states at the insulator-semiconductor interface. From the dependence of the loss on frequency, information about density and depth of interface states could be extracted.

Finally, a third dispersion appeared at very high frequencies (»100 kHz), causing the capacitance to fall almost to zero. It was attributed to the interface with the gold contact, which was expected to show a small resistance.

The three dispersions, described above, were highlighted in a Cole-Cole plot (Fig. 5.5), where the imaginary and real parts of the admittance, describing a dispersion phenomenon, assumed the shape of a circle with the center located on the real axis ($L_P$=0) or below it.

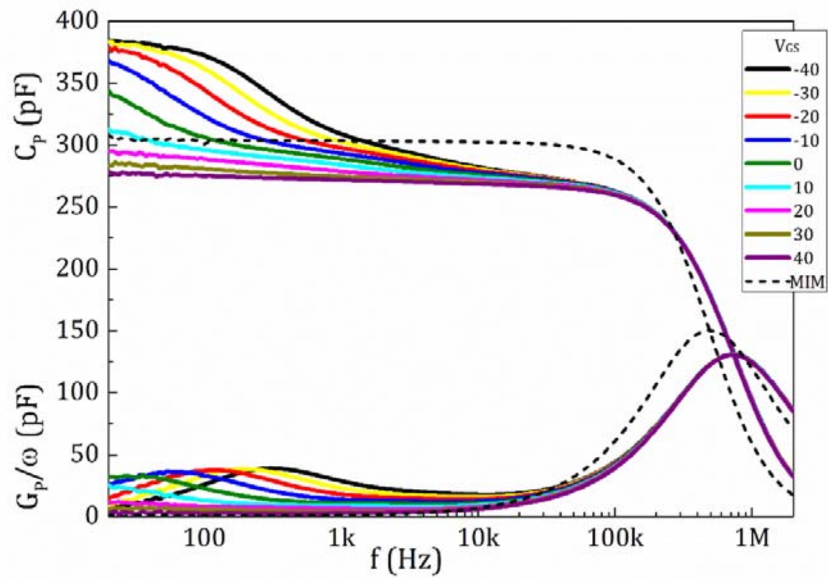


**Figure 5.3.** Frequency-dependence of the capacitance, *C*, and the loss, *G/ω*, of a MIS capacitor fabricated with pentacene and of a MIM with silicon dioxide. Linear scale for admittance axis.

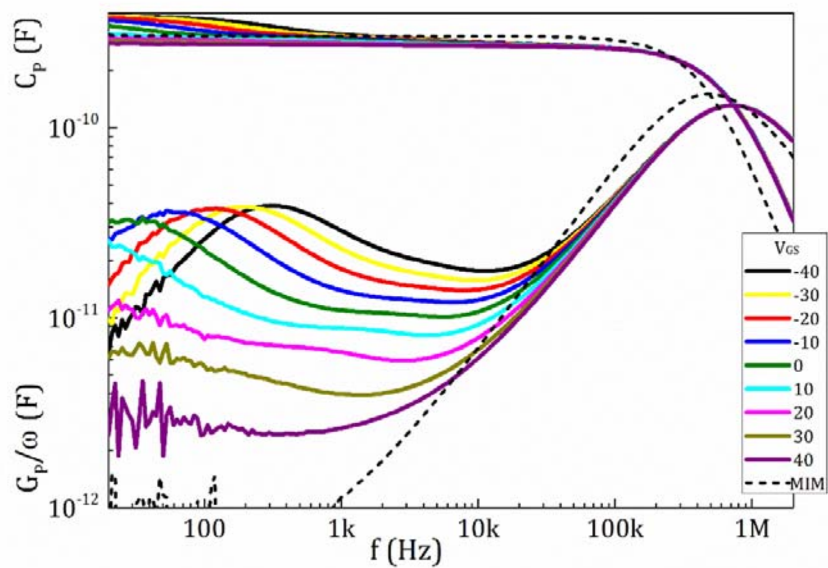


**Figure 5.4.** Frequency-dependence of the capacitance, *C*, and the loss, *G/ω*, of a MIS capacitor fabricated with pentacene and of a MIM with silicon dioxide. Logarithmic scale for admittance axis.

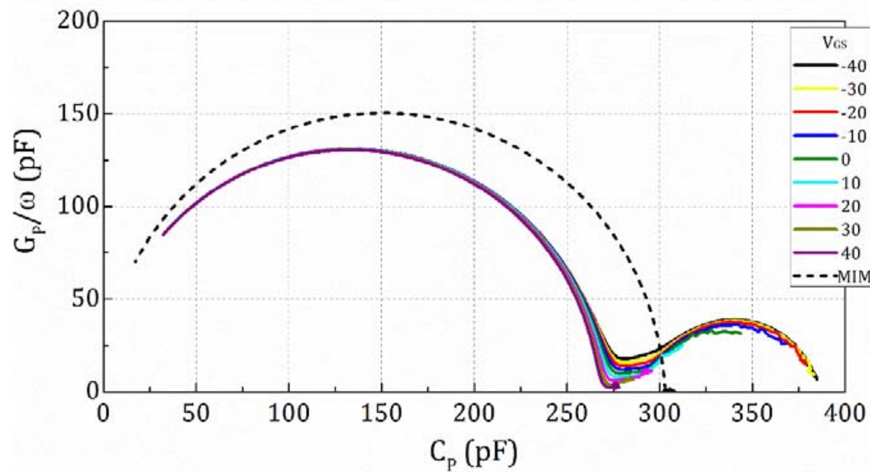


**Figure 5.5.** Cole-Cole plot for a MIS capacitor fabricated with pentacene and of a MIM with silicon dioxide. For almost every gate voltages, three circles are visible for the MIS capacitor: the right one, the largest, is related to contact resistance; the left one is due to the trap states at the insulator-semiconductor interface; the suppressed circle in the middle arises from the bulk semiconductor traps.

## 5.2 Equivalent electrical model

The results were explained through the modeling of an equivalent circuit (Fig. 5.6). The electrical model was capable to distinguish the dynamics of each physical process occurring in the MIS device. Starting from a theoretical approach, the model was progressively built through the experimental observations and was increasingly improved by the introduction of new elements. They were connected to each other through different relationships, each describing a single process in the device. This particular procedure yielded a direct physical identification of electrical parameters. As shown below, each layer, in principle, could be described by the parallel combination of equivalent capacitances and conductances. In detail, their values depended on the operating region of the device. Afterwards, these components were combined with more complicated elements, describing the trapping and transport mechanisms typical of organic materials.

The admittance techniques were revealed to be very useful for the characterization of trap states. Indeed, the capacitance could be directly linked with the trap density involved in the processes, since it represents the ability of storing charge on these states [12]. In particular, the relaxation time constant usually gave information about trap state thermalization time, which in turn depends on the trap state depth in energy.

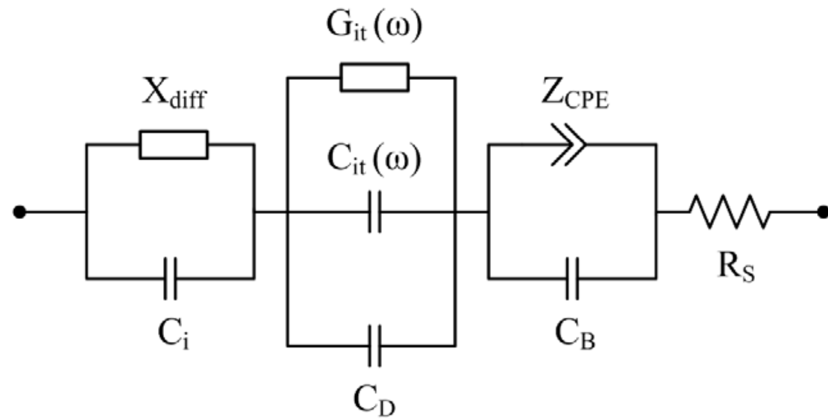


**Figure 5.6.** Equivalent circuit for an organic based MIS capacitor. It is constituted of four main blocks, arranged in the order: gate insulator layer, depletion layer in the semiconductor with interface trap states, organic semiconductor bulk and contact resistance.

### 5.2.1 Insulator layer

The insulator layer was described by a capacitor, with plates of cross-sectional area $A$ and separated by a distance $t_i$:

$$C_i = \varepsilon_0 \varepsilon_i \frac{A}{t_i}, \qquad (5.2)$$

where $\varepsilon_0$ is the vacuum permittivity and $\varepsilon_i$ is the dielectric constant of the insulator. This capacitance could be measured either directly through the MIM capacitor, fabricated on the same substrate of the devices, or though the maximum capacitance of the MIS junction, measured at low frequency in accumulation regime. In both cases, an

anomalous dispersion was seen along the entire range of frequency. This behavior was attributed to the diffusion current of slow ions through the insulator and could be related to the bias stress effects observed in organic field effect transistors. The response of slow species was well described by a complex susceptibility [13], $X_{diff}$, placed in parallel to the insulator capacitance:

$$X_{diff} = A_{diff}\left(j\omega\right)^{-\delta}, \tag{5.3}$$

where the amplitude $A_{diff}$ depends on the ion concentration, the insulator thickness and the temperature. $\delta$ is a parameter defining the continuous time random walk of particles: for $0<\delta<0.5$ the diffusion is anomalous, while the case $\delta=0.5$ corresponds to normal diffusion.

This component gave the major contribution at very low frequencies. It was observed in silicon dioxide, where it was supposed to be generated by the reaction between the Si-OH bonds present at the surface and water molecules diffused through the organic film. However, it was prevalent when a polymeric insulator was used.

The diffusion equation justified the dependence of capacitance on time, because of the intrusion of ions in the insulator, and contributed to the loss part of the MIM admittance at low frequency. The dispersion observed in the MIM junction at very high frequencies, as well as in the MIS capacitor, was related to the contact resistance, as will be illustrated further on.

### 5.2.2 Depletion layer and interface states

When the dc voltage was swept from -40 V towards 40 V, the majority carrier density decreased and the semiconductor film was gradually driven from accumulation into depletion regime. The depletion layer, i.e. the region free of charges, should react as a dielectric and it was represented through the capacitor:

$$C_D = \varepsilon_0 \varepsilon_{osc} \frac{A}{w_D}, \tag{5.4}$$

where $\varepsilon_{osc}$ is the dielectric constant of the organic semiconductor and $w_D$ is the depletion layer width.

In depletion region, the effects of interface trap states might be probed. Each trap level should contribute to some energy dispersion and introduce a relaxation time constant, $\tau_{it}$, described by the series combination of a capacitance $C_T$ and a conductance $G_T$ [14].

The admittance for the depletion layer, taking into account the interface trap states, could be represented by the parallel combination of the depletion capacitance $C_D$, an equivalent trap capacitance $C_{it}(\omega)$ and an equivalent trap conductance $G_{it}(\omega)$:

$$Y_D(\omega) = j\omega\left[C_D + C_{it}(\omega)\right] + \omega L_{it}(\omega), \tag{5.5}$$

where $L_{it}(\omega)=G_{it}(\omega)/\omega$ is the loss associated to the trap states.
According to the single time constant model, the equivalent admittance of depletion layer is:

$$Y_D(\omega) = j\omega\left[C_D + \frac{C_T}{1+\left(\omega\tau_{it}\right)^2}\right] + \omega\frac{C_T\omega\tau_{it}}{1+\left(\omega\tau_{it}\right)^2}, \tag{5.6}$$

with $\tau_{it}=C_T/G_T$. At low values of $\omega\tau_{it}$, interface traps respond immediately to the ac gate voltage, so that the sum $C_D+C_T$ is observed. Moreover, since their occupancy changes in phase with the signal maintaining the equilibrium, there is no energy loss. As $\omega\tau_{it}$ increases, traps lag behind the ac voltage, making the capacitance decrease. The energy loss reaches a peak, matching half the level of the corresponding capacitance when $\omega\tau_{it}$=1. Finally, at large values of $\omega\tau_{it}$, interface traps hardly change occupancy in response to the ac signal, so that loss again drops to zero and the only depletion capacitance is measured. Thus, a peak in loss spectrum at $\omega_{max}$ suggests the presence of a physical process with relaxation time $\tau_{it}=1/\omega_{max}$.

These effects are cumulative: when more than one process is occurring in the device, a peak for every process is observed in the loss plot. For a distribution of interface trap levels over the semiconductor bandgap, each interface trap level, in an energy interval a few $kT$ around surface Fermi level, contributes with a different energy loss, depending on its distance in energy from the majority carrier band. Consequently, a continuous distribution of relaxation times is introduced and the plots become more complicated.

According to the model for a distribution of single trap levels, the equivalent admittance is:

$$Y_D(\omega) = j\omega\left[C_D + \frac{qD_{it}}{\omega\tau_{it}}\arctan\left(\omega\tau_{it}\right)\right] + \omega\frac{qD_{it}}{2\omega\tau_{it}}\ln\left[1+\left(\omega\tau_{it}\right)^2\right], \quad (5.7)$$

where $D_{it}$ is commonly referred to as the density of interface trap levels per unit area per electron volt. In this case, the capacitance and conductance plots are broader along the ω axis: the loss peak occurs at $\omega\tau_{it}$=1.98 and its value is $G_{it}/\omega|_{max}$=0.4$qD_{it}$. These two equations are used to determine the relaxation time $\tau_{it}$ and the density of interface traps $D_{it}$.

### 5.2.3 Organic semiconductor bulk

Semiconductor bulk traps were also known to cause a frequency dispersive capacitance and a conductance contribution [14]. It was supposed that the pentacene layer, out of the depletion region, could be described by a capacitance $C_B$ and a resistance $R_B$:

$$C_B = \varepsilon_0\varepsilon_{osc}\frac{A}{t_{osc} - w_D}, \quad (5.8a)$$

and

$$R_B = \rho_{osc}\frac{t_{osc} - w_D}{A}, \quad (5.8b)$$

where $\varepsilon_{osc}$ and $\rho_{osc}$ are the dielectric constant and the resistivity, respectively, of the organic semiconductor, $t_{osc}$ is the width of the semiconductor layer, $w_D$ is the depletion region width.

The series sum of depletion and bulk capacitances should equal the capacitance of the organic semiconductor layer:

$$C_{osc} = \left(C_D^{-1} + C_B^{-1}\right)^{-1} = \varepsilon_0\varepsilon_{osc}\frac{A}{t_{osc}}. \quad (5.9)$$

For any operating regime, the product of bulk capacitance and resistance gave the relaxation time of the organic material, defined as:

$$\tau_B = C_B R_B = \varepsilon_{osc}\,\rho_{osc}, \quad (5.10)$$

that is, the time needed by the majority carriers to neutralize a disturbance. When the period of the electric field becomes comparable to the relaxation time of semiconductor, a Debye-type dispersion is expected to appear at a frequency $f_B$, whose value depends on the operating regime:

$$f_B = \frac{1}{2\pi R_B \left(C_0 + C_B\right)}, \tag{5.11}$$

with

$$C_0 = \frac{C_I C_D}{C_I + C_D}. \tag{5.12}$$

The relaxation frequency of the dispersion in the bulk should start from the minimum value:

$$f_B^{\min} = \frac{1}{2\pi R_B \left(C_I + C_B\right)}, \tag{5.13}$$

when the device is in accumulation, and should be upper-limited by the relaxation time constant:

$$f_B^{\max} = \frac{1}{2\pi \tau_B}, \tag{5.14}$$

when the organic semiconductor layer is fully depleted.

However, in the bulk of the organic semiconductor, where deeper traps were present, the Debye relaxation model was revealed not to be appropriate. Indeed, the relaxation appeared stretched over a wider range and the loss did not achieve half-way the low frequency capacitance. In particular, the Cole-Cole plots (loss vs. capacitance) had the shape of depressed arcs, with the center displaced below the real axis ($L_P$=0). These plots could result from a system with traps homogenously distributed in energy, with relaxation times $\tau$ exponentially depending on the depth (Fig. 5.7).

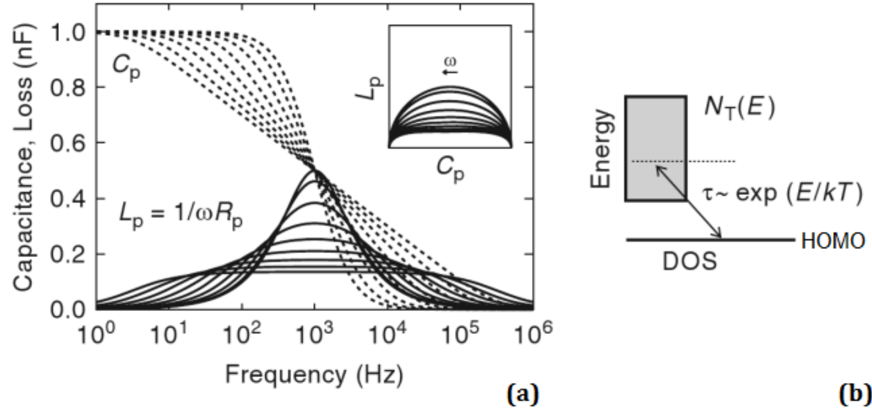


**Figure 5.7.** (a) Simulation of spectra of capacitance and loss for homogeneous state distributions. Inset: Cole-Cole plot with flattened arcs. (b) Energy diagram for a uniform distribution. The larger the distribution is, the more stretched the plots are. From Ref. [12].

In order to describe this behavior, the Cole-Cole theory [15], usually used for polar liquid and solids, was found to be more adequate. Differently from the classical theory, which described the dielectric constant in the complex plane as semicircles in the form:

$$\varepsilon^* - \varepsilon_\infty = \frac{\varepsilon_0 - \varepsilon_\infty}{1 + j\omega\tau_0}, \tag{5.15}$$

Cole and Cole represented the dispersion and absorption of a large number of nonhomogeneous dielectrics by the formula:

$$\varepsilon^* - \varepsilon_\infty = \frac{\varepsilon_0 - \varepsilon_\infty}{1 + \left(j\omega\tau_0\right)^{1-\gamma}}, \tag{5.16}$$

where $\varepsilon^*$ is the complex dielectric constant, $\varepsilon_0$ and $\varepsilon_\infty$ are the static and high frequency limits of the dielectric constant, respectively, $\tau_0$ is the most probable relaxation time and the parameter $\gamma$, assuming a value between 0 and 1, indicates the width of distribution of relaxation times. The case $\gamma$=0 corresponds to Debye equation.

Relying on Eq. (5.16), the dielectric response of the polycrystalline organic semiconductor was described by a complex impedance, which could consider the capture processes from deep traps in the bandgap

and the relaxation process related to the excitation from them. In particular, the semiconductor layer was represented by the parallel combination of a capacitor, $C_B$, and a constant phase element (CPE) of the form:

$$Z_{CPE} = R_B \left( j\omega\tau_B \right)^{-\alpha}, \tag{5.17}$$

where Eqs. (5.8a), (5.8b) and (10) are still valid, and $\alpha$ is the dispersion parameter.

This expression for the CPE was designed in order to generate an admittance for the organic semiconductor layer, which could yield an infinite capacitance for low frequencies ($\omega \ll 1/\tau_B$) and a capacitance coinciding with the bulk layer for high frequencies ($\omega \gg 1/\tau_B$).
The resulting equation was:

$$Y_B = j\omega C_B \left[ 1 + \left( j\omega\tau_B \right)^{\alpha-1} \right], \tag{5.18}$$

which, combined with the series of the insulator and depletion capacitances, led to an expression, for the total admittance of the circuit in Figure 5.8, reproducing the Cole-Cole equation:

$$Y_{tot} = j\omega \left[ \frac{C_0 C_B}{C_0 + C_B} + \frac{C_0^2}{C_0 + C_B} \cdot \frac{1}{1 + \frac{C_0 + C_B}{C_B} \left( j\omega\tau_B \right)^{1-\alpha}} \right]. \tag{5.19}$$

Here, the static limit of the capacitance is $C_0$, matching Eq. (5.12), and the high frequency limit is:

$$C_\infty = \frac{C_0 C_B}{C_0 + C_B} = \frac{C_i C_{osc}}{C_i + C_{osc}}, \tag{5.20}$$

i.e. the geometric capacitance of the device, $C_{geo}$, independent from the operating regime.

The dispersion peaks occurred at the frequency:

$$f_B = \frac{1}{2\pi R_B \sqrt[1-\alpha]{\dfrac{C_0 + C_B}{C_0^\alpha}}}, \tag{5.21}$$

which, oppositely to Eq. (5.11), decreased when devices were driven from accumulation into depletion region, in accordance to experimental data.

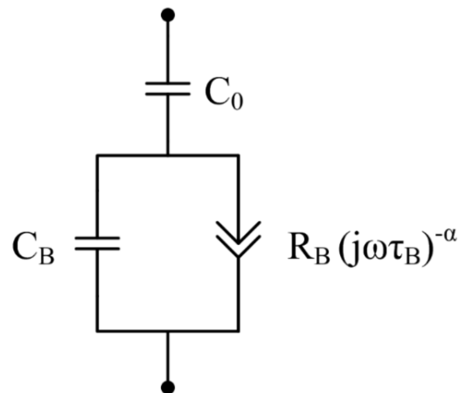


**Figure 5.8.** Equivalent circuit for an organic semiconductor bulk. $C_0$ represents the series sum of insulator and depletion capacitances.

The constant phase element is not supported in time-domain compact circuit simulators, but it could be replaced with a set of series-RC branches in parallel [16]. The number of branches is theoretically infinite, but given a required phase tolerance and a finite frequency range over which the approximation must hold, the number of branches could be limited.

### 5.2.4 Contact resistance

A series resistance $R_S$ was added to the equivalent circuit, in order to justify the dispersion occurring at very high frequencies. The peak amplitude and position of the loss curves appeared nearly independent from the operating regime. It was reasonably attributed to the energy barrier at the interface between the organic film and the metallic contact. Thanks to the low charge injection barrier for holes, defined by the difference between the work function of gold and the HOMO level

in pentacene, the contact resistance should be small and the dispersion was expected to appear at high frequency.

According to the circuit in Figure 5.6, the relaxation frequency, introduced by the electrode, was:

$$f_C = \frac{1}{2\pi R_S C_{geo}}, \tag{5.22}$$

where $R_S$ is the contact resistance and $C_{geo}$ is the capacitance seen by the resistance, that is, the geometric capacitance of the device.

## 5.3 Model simulations

The equations, developed for an organic MIS capacitor and illustrated in the previous paragraph, were entered into a MATLAB® program in order to generate the curves of the imaginary and real components of the admittance as a function of the signal frequency.

For the calculations, a device with a 350 nm thick $SiO_2$ layer and 100 nm thick pentacene film was considered. The relative dielectric constants used for dielectric and semiconductor were the typical values of 3.9 and 4, respectively. The anomalous diffusion through the insulator was defined by an amplitude $A_{diff}$ of 50 pF(rad/s)$^{\delta}$ and an exponent $\delta$ of 0.07, representing the mean value estimated from the frequency dependence of capacitance in a MIM junction. The dispersion in the organic bulk was described by a parameter $\alpha$=0.2, while its resistivity was set to yield a relaxation time $\tau_B$ of about 50 µs [17].

The evolution of depletion and bulk capacitances was defined through the following equation describing the dependence of depletion region width from the gate voltage:

$$w_D = \sqrt{\left(\frac{\varepsilon_0 \varepsilon_{osc} A}{C_i}\right)^2 + \frac{2\varepsilon_0 \varepsilon_{osc}}{qN_A}\left(V_{GS} - V_{FB}\right)} - \frac{\varepsilon_0 \varepsilon_{osc} A}{C_i}, \tag{5.23}$$

where the flatband voltage $V_{FB}$ and the doping density $N_A$ were selected in order to drive the device from accumulation at $V_{GS}$=-40 V to full depletion at $V_{GS}$=40 V.

In addition, an exponential trap state distribution, following the single time constant model of Eq. (5.6), was introduced at the interface starting from a density $D_{it}$ of $7 \cdot 10^{12}$ cm$^{-2}$eV$^{-1}$ with a relaxation time $\tau_{it}$ of 1 ms [18].

Finally, a contact sheet resistance of about 25Ω/□ was considered, as it was extracted from previous measurements through the transfer length method (TLM) on pentacene samples with top gold contacts.
The simulated curve for admittance at different biases were shown in Figures 5.9 (linear scale) and 5.10 (logarithmic scale). The results indicated that the proposed model could predict the dynamics of the various processes involved in an organic device and could allow particular features to be recognized from the comparison between the simulations and the experimental observations.

For low frequencies, the measured capacitance in accumulation was equal to the insulator capacitance including the effect of anomalous diffusion. When gate voltage was reduced, a depletion layer was created. While it expanded in the semiconductor layer, the low frequency capacitance dropped from the insulator capacitance to the series sum of $C_i$ and the capacitance of depletion layer including the contribution of interface trap states. In particular, interface defects, with a decreasing surface concentration as they became deeper into the bandgap, gave rise to loss peaks that shifted to lower frequencies, reflecting the real behavior observed in the pentacene device.

As regards the charge transport in the bulk of the semiconductor layer, a dispersion factor greater than zero was effective in describing the loss peaks, whose widths were broader than a peak related to a dispersion with a single time constant. Moreover, it reduced the magnitude of these peaks to a lower value compared with half the step deduced from the capacitance plots. The frequency $f_B$, the loss peaks were centered at, appeared to be nearly constant, while their amplitudes reduced as the depletion width $w_D$ increased from zero to $t_{osc}$.

Finally, the value used for the contact resistance produced a dispersion at a high frequency, coinciding for every gate dc bias.

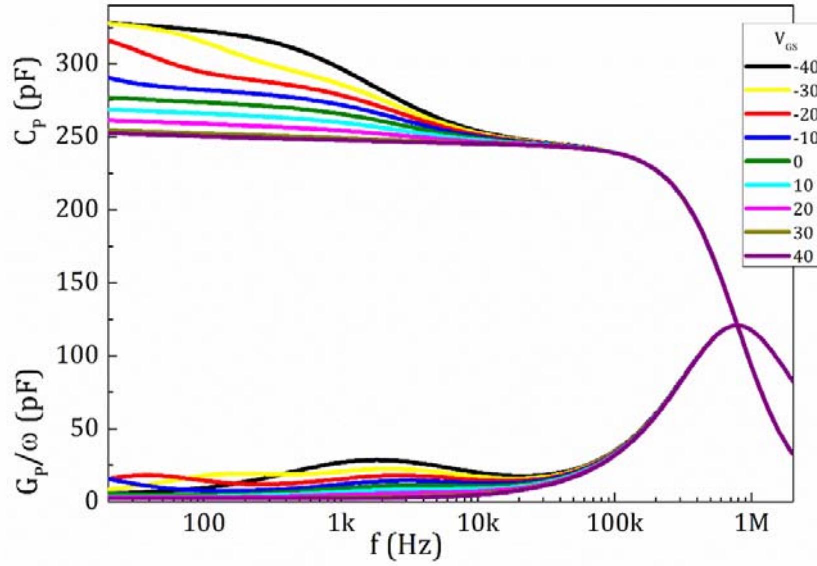


**Figure 5.9.** Simulations of the proposed electrical circuit for an organic based MIS capacitor: frequency-dependence of the capacitance, *C*, and the loss, *G/ω*. Linear scale for admittance axis.

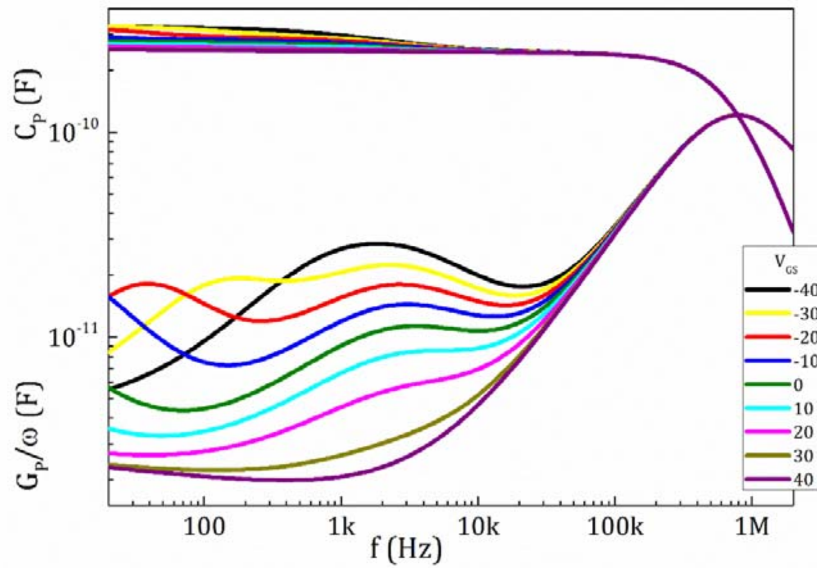


**Figure 5.10.** Simulations of the proposed electrical circuit for an organic based MIS capacitor: frequency-dependence of the capacitance, *C*, and the loss, *G/ω*. Logarithmic scale for admittance axis.

# 5.4 Experimental data fitting and model parameters

The analytic equations describing the proposed equivalent circuit were adopted to extract from the experimental data the physical and geometrical parameters, characteristic of the fabricated devices.

The fitting procedure was firstly adopted to the MIM structure. The low-frequency capacitance of the $SiO_2$ layer, sandwiched between the silicon substrate and the gold electrode, was 305 pF, given by an insulator capacitance of about 281 pF and a small contribution of slow charge diffusion. Assuming a dielectric constant of 3.9, the oxide thickness was estimated to be about 380 nm. However, by observing the curves of the MIS capacitor (Fig. 5.3), the low-frequency value measured at $V_{GS}$=-40 V revealed to be 385 pF, which was higher than the insulator capacitance, previously extracted. Since the curves at the highest negative $V_{GS}$ were nearly overlapping, it was deduced that a gate bias of -40 V was enough to reach the accumulation regime. For this reason, this high value should be attributed to the insulator layer, and, in first approximation, it was justified with a reduction in its thickness. The fitting procedure yielded an insulator capacitance, $C_i$, of 368 pF, corresponding to an oxide thickness of about 300 nm, and a small contribution from an anomalous diffusion phenomenon described by an amplitude $A_{diff}$=20 pF(rad/s)$^{\delta}$ and a parameter $\delta$=0.02.

The model equations were able to well describe the experimental data at different biases. The resulting fitting curves were reported in Figures 5.11 (linear scale) and 5.12 (logarithmic scale).

Each curve at a given bias arose from the combination of the four contributions illustrated above.

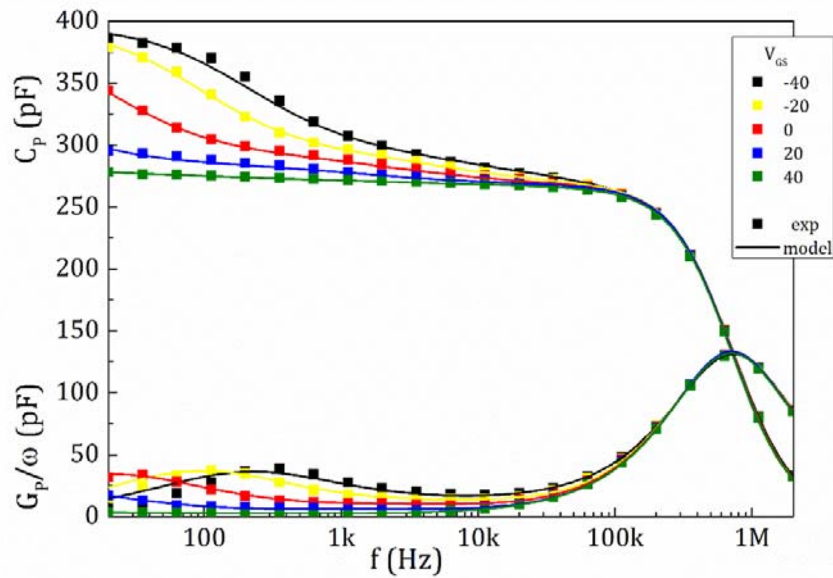


**Figure 5.11.** Frequency-dependence of the capacitance, *C*, and the loss, *G/ω* for a pentacene MIS capacitor. The solid lines are the fitting of experimental data to the proposed model equations. Linear scale for admittance axis.

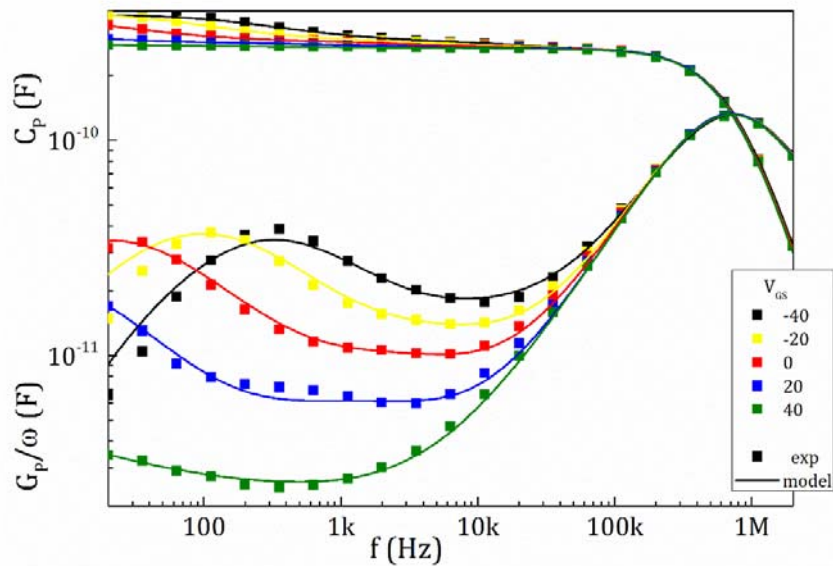


**Figure 5.12.** Frequency-dependence of the capacitance, *C*, and the loss, *G/ω* for a pentacene MIS capacitor. The solid lines are the fitting of experimental data to the proposed model equations. Logarithmic scale for admittance axis.

A representative example for the capacitance $C_P$ and the loss $G_P/\omega$ was shown in Figures 5.13 and 5.14, respectively, where four curves were traced.

The black curve represented the insulator capacitance $C_i$ given by Eq. (5.2) and included the contribution of the diffusion susceptibility $X_{diff}$ and the relaxation of the contact resistance. The anomalous diffusion described by Eq. (5.3) was also illustrated separately through a blue curve. In the capacitance plot, it introduced a line whose slope depended on the value of $\delta$; experiments, not reported here, revealed that this effect was greater in polymeric insulators. In the loss plot, the diffusion contributed with an increase in the losses for low frequencies.

As regards the contact resistance, it made a dispersion phenomenon occur at a high frequency given by Eq. (5.22). The fitting procedure gave the values of the contact resistance (Fig. 5.15), which was revealed to decrease as the device was driven into accumulation. This behavior could be attributed to the electrons, which, by accumulating under the contact, reduced the injection barrier, as it was observed in OTFTs [19] with a top-contact configuration.

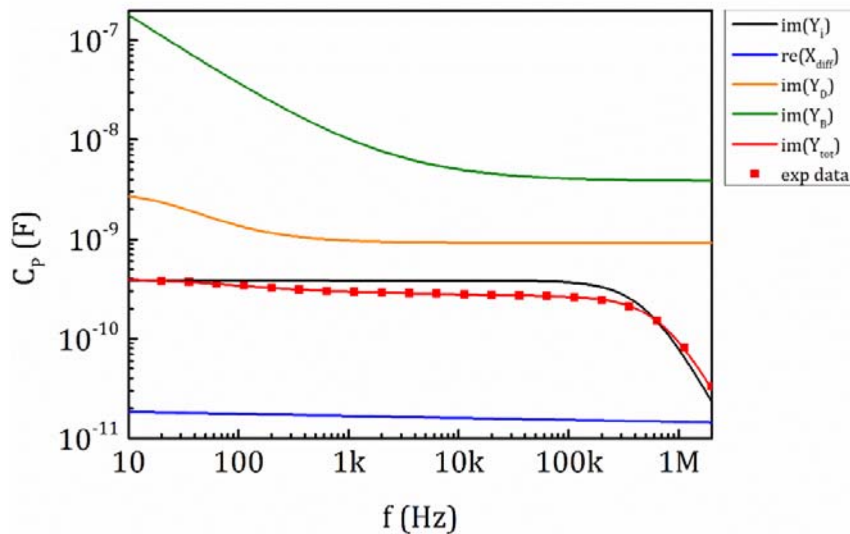


**Figure 5.13.** Example of the contributions to the imaginary part of the admittance ($V_{GS}$=-20 V). The experimental data are fitted with four contributions: dispersion for bulk defects from Eq. (5.18) (green line), depletion layer and interface traps from Eq. (5.7) (orange line), insulator layer including relaxation for contact resistance from Eq. (5.22) (black line), diffusion through the insulator from Eq. (5.3) (blue line). The resulting curve (red line) well describes the experimental data (red dots).

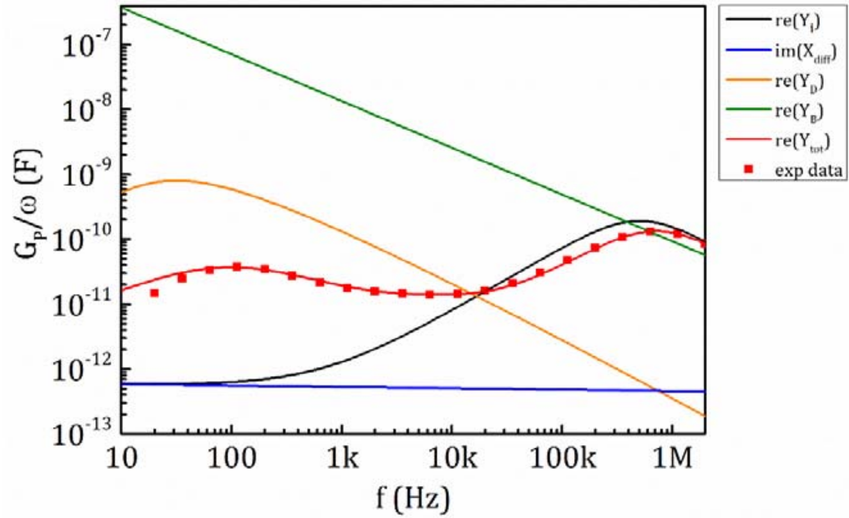


**Figure 5.14.** Example of the contributions to the real part of the admittance ($V_{GS}$=-20 V). The experimental data are fitted with four contributions: dispersion for bulk defects from Eq. (5.18) (green line), depletion layer and interface traps from Eq. (5.7) (orange line), insulator layer including relaxation for contact resistance from Eq. (5.22) (black line), diffusion through the insulator from Eq. (5.3) (blue line). The resulting curve (red line) well describes the experimental data (red dots).

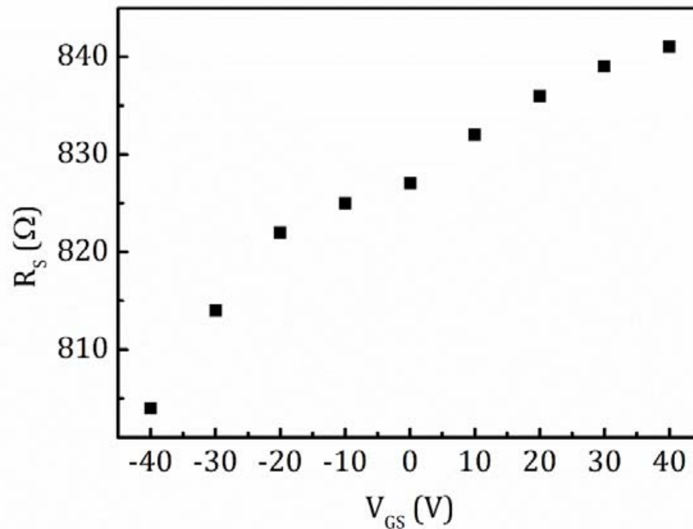


**Figure 5.15.** Extracted values for contact resistance, $R_S$.

The green curve in Figures 5.13 and 5.14 was described by Eq. (5.18) and it defined the features of the pentacene layer. It added a further contribution to the loss at intermediate frequencies and yielded a reduction in the overall capacitance over the introduction of the bulk capacitance $C_B$. Interestingly, the loss peak related to the dispersive transport in the bulk of the pentacene layer shifted to lower frequencies and became even broader, as the depletion width increased. This shift was higher than the value predicted by the model simulations where a constant $\tau_B$ was used, suggesting a gradual increase of the relaxation time constant of the material, as emerged from the extracted values (Fig. 5.16). By moving the dc bias towards the depletion regime, the probed region of the bulk was that far from the insulator interface and closer to the gold contact. This behavior indicated an increase of the resistivity, reasonably associated with a greater disorder near the contact. The origin could be the higher deposition rate during the thermal evaporation of the pentacene bulk or the diffusion of gold particles from the electrode. The hypothesis of an even more dispersed transport was also consistent with the growth of the parameter $\alpha$, which increased from to 0.26 to 0.4.

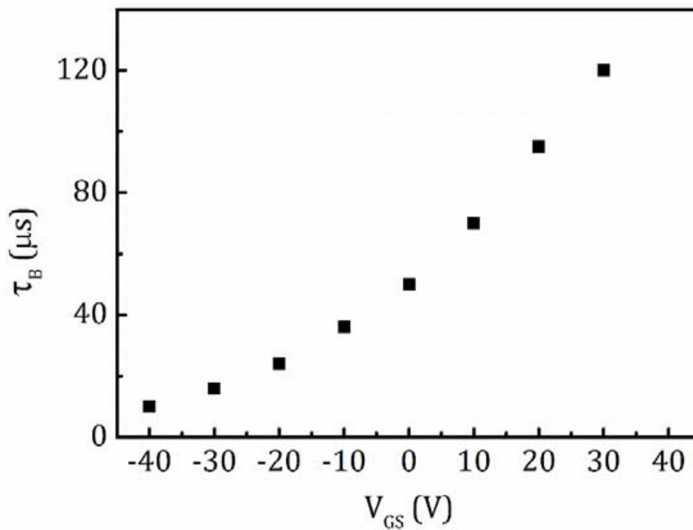


**Figure 5.16.** Extracted values for relaxation time, $\tau_B$, of pentacene bulk.

At last, the depletion regime gave rise to a capacitance $C_D$, according to Eq. (5.4), and allowed the observation of the energy levels

confined at the insulator-semiconductor interface. The equivalent capacitance at low frequency of the depletion layer was equal to the parallel sum of depletion and interface trap capacitances, while, above the frequency defined by the relaxation time $\tau_{it}$, it fell to $C_D$ (orange curve). This dispersion and the related peak manifested in the loss plot were well fitted through Eq. (5.7).

The equivalent admittance related to interface trap states described the capture and the following release of charge carriers from the trap level coinciding with the Fermi level at the surface. By tuning the gate-to-source bias, it should be possible to change the band bending at the surface of the organic semiconductor and examine the states that changed their occupancy. From the contribution given to the measured admittance, the surface density of interface states, $D_{it}$, within a range of a few $kT$ was extracted and reported, along with relaxation time constants $\tau_{it}$, in Figure 5.17. The maximum value of state density measured was about $1.2 \cdot 10^{12}$ cm$^{-2}$eV$^{-1}$.

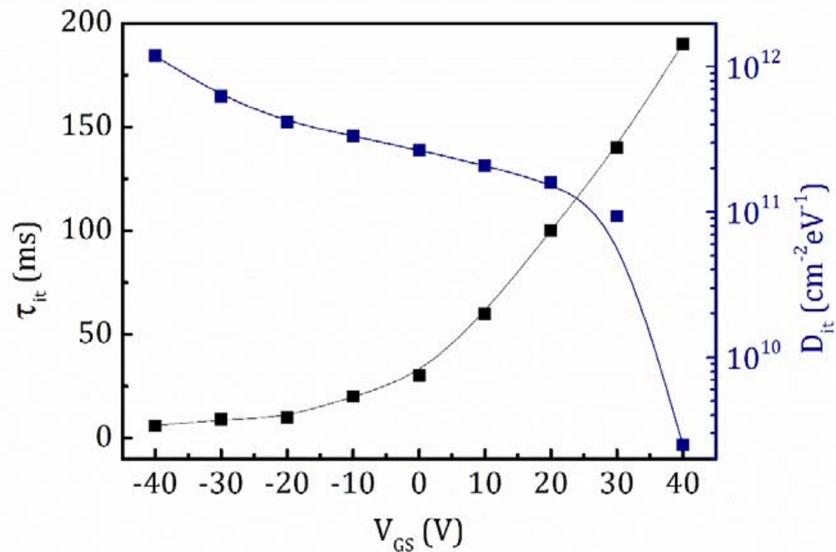


**Figure 5.17.** Extracted values for relaxation time, $\tau_{it}$, and surface density, $D_{it}$, of interface trap states.

The band bending, $\phi_S$, needed to probe a particular interface trap could be calculated from the solution of Poisson's equation in the depletion approximation:

$$\phi_S = \frac{qN_A w_D^2}{2\varepsilon_0 \varepsilon_{osc}}, \quad (5.24)$$

from the knowledge of the acceptor doping concentration, $N_A$, in the semiconductor and the depletion layer width. $N_A$ could be extracted from the capacitance-voltage measurements in the transition region between the accumulation and full depletion regimes, in particular from the linear part of the $C^{-2}$-$V$ curves, using the following expression:

$$\frac{\partial C^{-2}}{\partial V} = \frac{2}{\varepsilon_0 \varepsilon_{osc} q N_A A^2}. \quad (5.25)$$

However, it was not possible to apply the Schottky-Mott theory [20] to the C-V curves, since they were stretched at low frequencies by the presence of interface traps and were affected at intermediate frequencies by the dispersive transport in the pentacene bulk. These phenomena caused the doping density to be overestimated and, consequently, the extraction of an exact band bending was precluded. The inspection of the experimental curves provided also the values of depletion and bulk capacitances, which could be used to evaluate the depletion layer width. In this case, a particular feature arose. In detail, at every biases, the geometric capacitance of the semiconductor layer, given by the series sum of depletion and accumulation capacitances, exhibited a value (about 720 pF) related to a thickness larger than the actual thickness of organic semiconductor. Moreover, at $V_{GS}$=-40 V, while the extracted bulk capacitance was about 1.8 nF, corresponding to the total thickness of pentacene layer (60 nm) and indicating that the device was working in accumulation, a contribution of about 1.2 nF still manifested in the depletion capacitance. These results were interpreted through the presence of an interface layer between the insulator and the semiconductor, which introduced a contribution of 1.2 nF. Such a value, indeed, exactly compensated the difference between the extracted and the true geometrical capacitances of semiconductor layer, i.e. 720 pF and 1.8 nF, respectively. Furthermore, it justified the increase in the insulator capacitance from 281 pF, as appeared in the MIM device, to 368 pF, as extracted from the MIS junction. For this reason, this layer came across as a region of the $SiO_2$ film, at the interface with semiconductor, modified in its structure by the deposition of pentacene

or, anyhow, affected by the presence of trapping states, those which appeared through the loss peak revealed at $V_{GS}$=-40 V.

On the basis of this hypothesis, the depletion layer width was investigated as a function of gate voltage. The results, shown in Figure 5.18, revealed a disuniformity of the doping, or fixed charge, across the pentacene layer, in particular an increase towards the external surface of the film, presumably caused by the absorption of oxygen and moisture.

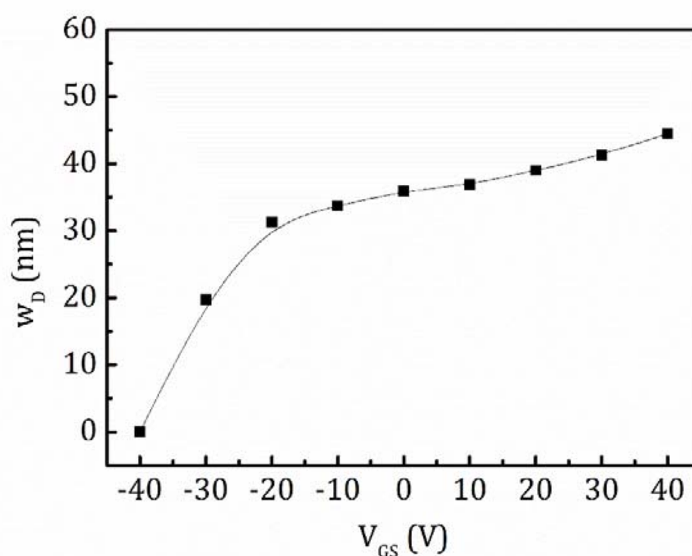


**Figure 5.18.** Extracted values for depletion layer width, $w_D$.

## 5.5 Temperature dependence of capacitance measurements

The temperature dependence of admittance-frequency characteristics of the organic based MIS capacitors was investigated, by considering in particular the effects of the interface states, the bulk defects and the series resistance. The devices were introduced in a cryostat (Janis CCS-450) and were characterized under a vacuum of about $5 \cdot 10^{-6}$ mbar (Fig. 5.19). A helium compressor and a heater (LakeShore Temperature

controller 335) were used to control the temperature over the range of 270-350 K.

**Figure 5.19.** Devices were located in a cryostat for admittance measurements at different temperatures.

It was found that, with increasing temperature, the capacitance plots and the loss peaks shifted in their position towards lower frequencies (Fig. 5.20). All characteristic frequencies, at different temperatures, were extracted. They showed a thermally activated behavior and, by the fitting to the Arrhenius equation:

$$f \sim \exp\left(-\frac{E_a}{kT}\right), \tag{5.26}$$

where $k$ is the Boltzmann constant and $T$ is the absolute temperature, it was possible to obtain the activation energy, $E_a$, of the related process.

The variations of the time constants, $\tau_{it}$ and $\tau_B$, and the contact resistance, $R_S$, were extracted, respectively, from the temperature dependence of $f_{it}$, $f_B$ and $f_S$.

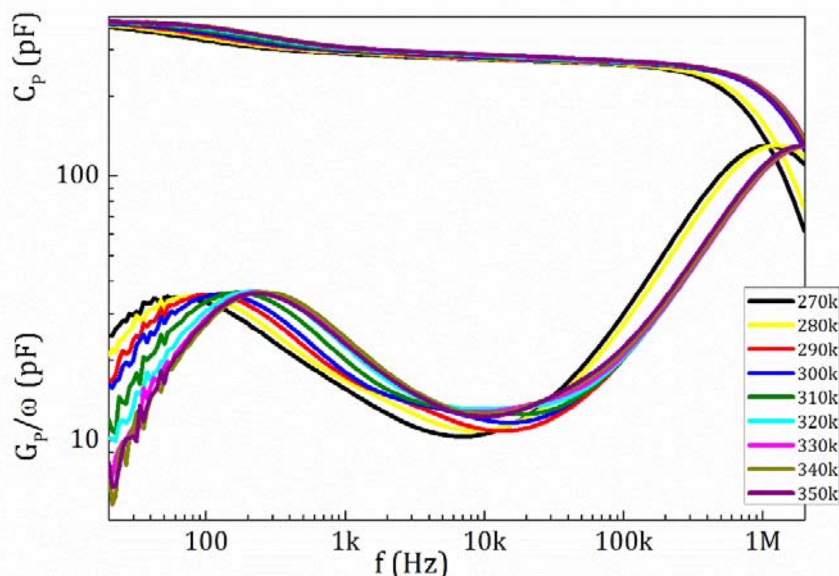


**Figure 5.20.** Temperature-dependence of admittance in a pentacene MIS capacitor ($V_{GS}$=-40 V).

The dispersion phenomena at low frequencies revealed the presence of hole traps at the insulator-semiconductor interface. The time constants $\tau_{it}$ represented their relaxation time and provided the distance of their energy level, $E_t$, from the highest occupied molecular orbital, $E_{HOMO}$, through the relation:

$$\tau_{it} \sim \exp\left(\frac{E_t - E_{HOMO}}{kT}\right). \tag{5.27}$$

From the analysis of interface trap levels for $V_{GS}$=-40 V a depth of 210 meV was deduced (Fig. 5.21).

As regards the dispersive transport in the pentacene bulk, the temperature dependence of the relaxation time indicated a distribution of traps centered at about 500 meV above the HOMO level (Fig. 5.22).

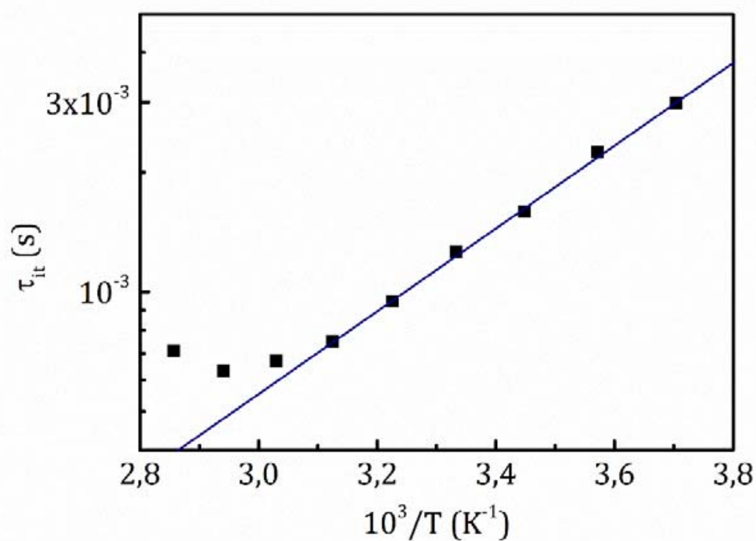


**Figure 5.21.** Arrhenius plot for relaxation time of interface traps. The slope of the linear region is proportional to the depth of trap states.

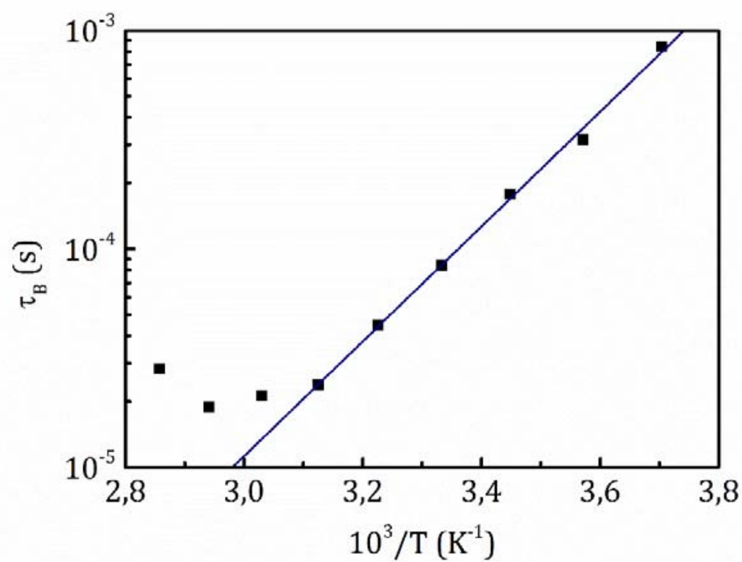


**Figure 5.22.** Arrhenius plot for relaxation time of pentacene bulk. The slope of the linear region is proportional to the depth of trap states.

Finally, reminding that the resistance exhibited by an ohmic contact, when the current is limited by thermionic emission through a barrier $\Phi_B$, has the form:

$$R_C \sim \exp\left(\frac{\Phi_B}{kT}\right) \tag{5.28}$$

the carrier injection barrier at the metal-organic contact was estimated to be about 0.13 eV.

## 5.6 Validation of the electrical model

It was seen that the inspection of the admittance plots by means of the proposed electrical model revealed plenty of features of an organic devices [21]. The model was initially tested with pentacene based MIS capacitor realized on silicon wafer and provided interesting information about the insulator-semiconductor interface. Subsequently, the validity of the model was studied over a set of different devices. In particular, the results obtained over a treatment of the silicon oxide surface were reported below.

The substrates with $SiO_2$ layer were covered by a polymeric solution of Poly(methyl methacrylate) (PMMA) in xylene, spin-coated with a rotation speed of 9000 rpm for 30 s, before the pentacene deposition. The frequency-dependence of admittance of the MIS devices and the related MIM capacitors were reported in Figures 5.23 (linear scale) and 5.24 (logarithmic scale).

It was evident that, contrary to the previous case, the maximum capacitance measured at low frequencies in the MIM device, when it operated in accumulation regime, corresponded to the insulator capacitance measured by means of the MIM junction.

The other parameters were obtained applying the model equations to the experimental data. The introduction of a polymeric layer increased the factors describing the anomalous diffusion ($A_{diff}$ =80 pF(rad/s)$^{\delta}$, $\delta$=0.07). Moreover, at the interface, shallower traps were discovered with a surface density of about $6{\cdot}10^{12}$ cm$^{-2}$eV$^{-1}$ with a relaxation time of 90 µs, while deeper traps showed a decreased concentration.

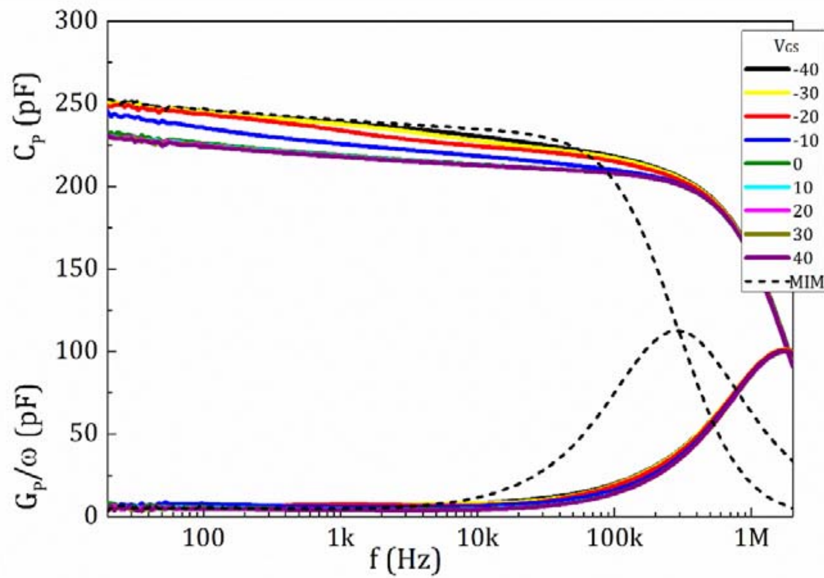


**Figure 5.23.** Frequency-dependence of the capacitance, *C*, and the loss, *G/ω*, of a MIS capacitor fabricated with pentacene and of a MIM with silicon dioxide covered with a PMMA film. Linear scale for admittance axis.

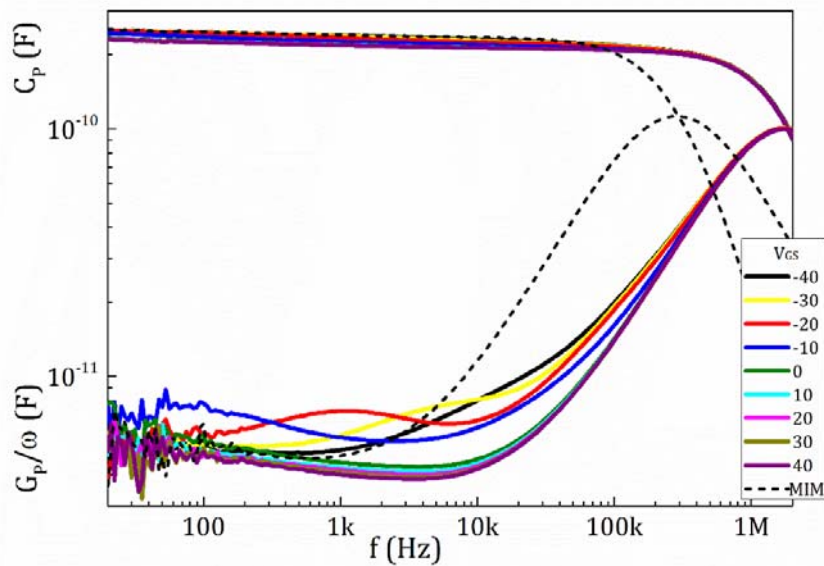


**Figure 5.24.** Frequency-dependence of the capacitance, *C*, and the loss, *G/ω*, of a MIS capacitor fabricated with pentacene and of a MIM with silicon dioxide covered with a PMMA film. Logarithmic scale for admittance axis.

The mobility in the bulk turned out to be enhanced with a greater relaxation time of 700 ns, indicating an improvement in the order degree of the pentacene structure.

These results reflected the modification of insulator surface energy. Thanks to the PMMA coating, the surface energy of the $SiO_2$ layer decreased from 73.5 mJ/m$^2$ to 47.1 mJ/m$^2$, especially for the effect of the reduction of the polar component from 36.5 mJ/m$^2$ to 8.4 mJ/m$^2$. This aspect had positive effects on the performance of the organic device, since a surface with a lower energy tends not to attract charge species, which could react with the organic materials and deteriorate them, and, at the same time, favors the growth of a more ordered film of pentacene.

## 5.7 Conclusion

The admittance of pentacene-based MIS capacitors was measured as a function of frequency and an electrical model able to provide a full description of their features was developed. The model simulations revealed that the proposed analytical equations are effective in predicting and explaining the dynamics of an electrical device realized with organic materials. Furthermore, the model is useful to compare the properties and the performance of devices fabricated with different geometries, materials and deposition conditions.

The results, obtained by the fitting of the experimental data with the equivalent circuit equations, suggested the presence of hole trapping states at the insulator-semiconductor interface, affecting the transport in the conduction channel. The shallower traps had a concentration of about $2 \cdot 10^{12}$ cm$^{-2}$ eV$^{-1}$, while going deeper inside the bandgap the density decreased to about $9 \cdot 10^{9}$ cm$^{-2}$ eV$^{-1}$. Meanwhile, in the bulk of pentacene layer a wide distribution was found centered at about 0.5 eV. The addition of a thin polymeric film of PMMA, which reduced the polarity of the silicon dioxide surface, increased the concentration of the shallower traps at the insulator-semiconductor interface but improved the mobility in the pentacene layer.

# References

1. S. D. Wnag, T. Minari, T. Miyadera, Y. Aoyagi, and K. Tsukagoshi, Appl. Phys. Lett. **92**, 063305 (2008)
2. D. Knipp, R. A. Street, and A. R. Völkel, Appl. Phys. Lett. **82**, 3907 (2003)
3. M. Koehler, and I. Biaggio, Phys. Rev. B **68**, 075205 (2003)
4. R. A. Street, J. E. Northrup, and A. Salleo, Phys. Rev. B **71**, 165202 (2005)
5. K. Berke, S. Tongay, M. A. McCarthy, A. G. Rinzler, B. R. Appleton, and A. F. Hebard, J. Phys. Condens. Matter **24**, 255802 (2012)
6. T. Miyadera, T. Minari, K. Tsukagoshi, H. Ito, and Y. Aoyagi, Appl. Phys. Lett. **91**, 013512 (2007)
7. R. Scholz, D. Lehmann, A.-D. Müller, and D. R. T. Zahn, Phys. Stat. Sol. (a) **205**, 591 (2008)
8. C. Siol, C. Melzer, and H. von Seggem, Appl. Phys. Lett. **93**, 133303 (2008)
9. C.-W. Sohn, T.-U. Rim, G.-B. Choi, and Y.-H. Jeong, IEEE Trans. on Electron Dev. **57**, 986 (2010)
10. C. S. Kim, S. J. Jo, S. W. Lee, W. J. Kim, H. K. Baik, ans S. J. Lee, Adv. Funct. Mater. **17**, 958 (2007)
11. X. Sun, C.-a. Di, and Y. Lin, J. Mater. Chem. **20**, 2599 (2010)
12. P. Stallinga, *Electrical Characterization of Organic Electronic Materials and Devices* (Wiley, Chichester, UK, 2009)
13. R. Ledru, S. Pleutin, B. Grouiez, D. Zander, H. Bejbouji, K. Lmimoun, and D. Vuillaume, Organic Electronics **13**, 1916 (2012)
14. E. H. Nicollian, and J. R. Brews, *MOS (Metal-Oxide-Semiconductor) Physics and Technology* (Wiley, New York, 2002)
15. K. S. Cole, and R. H. Cole, J. Chem. Phys. 9, 341 (1941)
16. J. Scott, and P. Single, IEEE Trans. Biomed. Circuits Syst. Accepted for future publications.
17. L. Zhang, D. Taguchi, J. Li, T. Manaka, and M. Iwamoto, Physics Procedia **14**, 46 (2011)
18. H. W. Zan, C.-W. Chou, K.-H. Yen, Thin Solid Films **516**, 2231 (2008)
19. G. Horowitz, P. Lang, M. Mottaghi, and H. Aubin, Adv. Funct. Mater. **14**, 1069 (2004)
20. S. M. Sze, *Physics of Semiconductor Devices*, 2nd ed. (Wiley, New York, 1981)

21. R. Liguori, and A. Rubino, “Electrical model for admittance spectroscopy in organic based MIS capacitors”, Organic Electronics. Manuscript in preparation.

# Conclusions

In this thesis, organic electronic devices were studied and modeled, focusing particularly on the relationship between the electrical characteristics and the physical processes occurring in the devices.

During the research activities, various models were introduced, able to describe charge transport in organic semiconductors, photocurrent phenomena and trapping mechanism dynamics in organic thin film transistors (OTFTs). The aim of the labor devoted to organic electronics was to provide reliable models, which could favor a better comprehension of the mechanisms underlying the organic transistor operation and which could be also employed on electrical simulations.

The fundamental effort of this thesis was addressed to one of the most critical topics of organic devices, that is, the investigation of interface trap states, which strongly affect the performance of organic thin film transistors. Indeed, the performance reliability under realistic atmospheric conditions is a fundamental need for the feasibility of organic electronics.

Electrical instability were observed in the fabricated organic thin film transistors. Most of the phenomena observed in the fabricated devices were justified by assuming a multiple trapping and release mechanism to occur, due to the high concentration of traps in organic materials.

Thus, in the first part of the work, particular analyses of the physical properties of organic materials were presented, exploiting in detail the photo-excitation of charge carriers to produce hidden phenomena which were useful for the characterization of localized states. At the same time, the effects of external factors, such as prolonged application of the bias and continuous exposure to high-energy irradiation, were studied.

Important results were obtained during the characterization of a pentacene thin film under light conditions and, in this occasion, a mathematical model describing the dynamics of metastable defects induced by ultraviolet irradiation was developed. As explained in Chapter 3, the photocurrent evolution was first related to the trapping sites concentration through the definition of apparent mobility; then, the

evolutions of two types of induced defects, referred to as slow and fast defects, were reconstructed thanks to the proposed equations and were demonstrated to control the degradation and recovery kinetics of conductivity.

The theory related to the multiple trapping and release mechanism was revealed to be effective also in explaining the gate bias dependence of field effect mobility, when the fabricated OTFTs were measured in dark, and, in this work, it was exploited in the development of the equations modelling the OTFT behavior under light conditions. This model was reported in Chapter 4 and allowed a simultaneous study of the light effects on material structure, the trapping process of electrons at the insulator-semiconductor interface and the photoconductive efficiency in the organic semiconductor.

The physical phenomena occurring in an OTFT at the interface where the conducting channel is formed were revealed to dominate all important aspects of device performance, including operating voltage and degradation. Thus, since interfaces represent a fundamental factor for both device engineering and physical theory, an important part of the research activities dealt with the characterization of organic based metal-insulator-semiconductor (MIS) devices through admittance techniques, which allowed to separate the effects of charge trapping at the interface from that occurring in the organic film.

A first approach was the use of photocapacitance measurements. In this case, the photoinduced shift of threshold voltage and the introduction of pronounced hysteresis phenomena suggested the presence of electron trapping states at the interface and allowed their characterization. The second approach was that revealed as the main contribution to the OTFT modeling. By the means of admittance spectroscopy, an electrical model was developed to describe the different dynamics of the organic device. Starting from a theoretical approach, first, a simple equivalent circuit was built. Then, over the experimental observations, it was increasingly improved by the introduction of new elements. Thus, every element was connected to each other through different relationships, each describing a single process in the device.

This model provides an efficient parameter extraction method. It allows the characterization of the diffusion of mobile ions, the dispersive transport in pentacene bulk, the hole trapping mechanism at the insulator-semiconductor interface, the contact resistance at the metal-organic interface. As a consequence, the model is useful to

compare the properties and the performance of devices with respect to the geometries, the materials and the deposition conditions. Moreover, the model simulations revealed that the proposed analytical equations could be effective in predicting the behavior of organic electronic devices.

The obtained results could be the basis for further studies devoted to the improvement of the knowledge about charge transport in organic semiconductors and interface properties, as well as, the models proposed could be exploited in circuit simulation techniques. In the meanwhile, the behaviors observed during experiments could suggest the use of pentacene based transistors as light activated memory devices or as memory elements capable to store information about illumination power and duration for an extended amount of time. The new outcomes illustrated in this work could also be used for the design of inverters and logic gates, whose electrical properties could be selectively controlled by ultraviolet illumination.